RFID Reader Design for Neural Implants

Christopher Sutardja

Electrical Engineering and Computer Sciences
University of California at Berkeley

Technical Report No. UCB/EECS-2018-153
http://www2.eecs.berkeley.edu/Pubs/TechRpts/2018/EECS-2018-153.html

December 1, 2018

RFID Reader Design for Neural Implants

By

Christopher Sutardja

A dissertation submitted in partial satisfaction

of the requirements for the degree of

Doctor of Philosophy

in

Engineering - Electrical Engineering and Computer Sciences

in the

Graduate Division

of the

University of California, Berkeley

Committee in charge:

Professor Jan M. Rabaey, Chair
Professor Elad Alon
Professor Ali Niknejad
Professor Martin White

Fall 2017

ABSTRACT

RFID Reader Design for Neural Implants

By
Christopher Sutardja

Doctor of Philosophy in Engineering- Electrical Engineering and Computer Sciences
University of California, Berkeley
Professor Jan M. Rabaey, Chair

Brain machine interfaces (BMI) have the ability to revolutionize both healthcare and neuroscience. Recent advances in neural interfaces have demonstrated the ability to control prosthetic limbs and to monitor and treat neurological diseases. Implants with the ability to acquire neural signals are the primary sources of information used to control these systems. To ensure low risk of infection, these implants should be powered wirelessly and communicate wirelessly to the outside world. An efficient, wearable RFID interrogator, sitting outside the skull delivering power to and receiving uplink data from these implants, is a critical component of a wireless BMI system that is convenient and safe for patients to use.

However, RFID readers have a classical problem of self-interference from the transmitted carrier leaking into the reader's receive path, potentially saturating and desensitizing the RX amplifiers. Conventional methods of carrier rejection result in an RFID reader form factor that is too bulky and impractical to be worn on a human head. To solve these problems, we have developed a novel architecture for a fully integrated RFID transceiver that uses only 1 antenna and no bulky isolation components. We exploit the non-linearity of a class E/Fodd switching PA and use it as a demodulator to mix our received backscattered signal back to baseband. The reader is fabricated on a 1.2 mm x 1.5 mm CMOS Integrated Circuit and was tested with a proprietary implant through a channel of pig skin and bovine t-bone to mimic the channel characteristics of a human skull. The system achieves a data rate of 2 Mb/s, while delivering 790 uW of power to the implant at a TX power consumption of 35 mW for an overall link efficiency of 2.3%. This efficient reader is well-suited for BMI systems meant for long-term chronic neural recording for the purposes of monitoring neurological diseases such as epilepsy and Alzheimer's disease.

Table of Contents

List of Figures

List of Tables

List of Acronyms

AC	Alternating Current
ADC	Analog to Digital Conversion
AM	Amplitude Modulation
AP	Action Potential
ASIC	Application Specific Integrated Circuit
BER	Bit Error Rate
BMI	Brain Machine Interface
BW	Bandwidth
CMOS	Complimentary Metal-Oxide-Semiconductor
DC	Direct Current
ECoG	Electrocorticography
EEG	Electroencephalography
FCC	Federal Communications Commission
IC	Integrated Circuit
IEEE	Institute of Electrical and Electronics Engineers
LNA	Low-noise Amplifier
MN	Matching Network
MOM	Metal-Oxide-Metal
NMOS	N-type Metal-Oxide-Semiconductor
PA	Power Amplifier
PCB	Printed Circuit Board
PMOS	P-type Metal-Oxide-Semiconductor
PN	Phase Noise
PPM	Pulse Position Modulation
Q	Quality Factor
RF	Radio Frequency
RFID	Radio Frequency Identification
RIR	Reflective Impulse Radio
RX	Wireless Receiver
SAR	Specific Absorption Rate
SMT	Surface Mount Technology
SNR	Signal to Noise Ratio
SRF	Self-Resonant Frequency
TX	Wireless Transmitter
UHF	Ultra High Frequency
UWB	Ultra-Wideband

Acknowledgements

It has been a long road. I have been at UC Berkeley for over 11 years as a graduate student and undergraduate student. This university, the faculty, and the students have pushed my intellectual boundaries to places I didn't know was possible. And the best part is that I know there is so much more explore. There have been many challenges, struggles, and triumphs along way. I have met so many amazing people during this journey, and I have made many great friends that will last a lifetime. I have come to think of Berkeley as my home, and there no other place I would have rather spent the past decade.

First of all, I would like to thank my advisor Jan Rabaey for all his support and guidance. Over the years, he has been extremely patient with me throughout my all my struggles during Grad School. His vision and excitement has shown me that although Moore's law might be slowing down, what we have seen is only the beginning for the impact of circuits advancing civilization and improving people's lives.

Elad Alon has done much more for me than form my foundation for IC design. He taught me that when building or designing anything, the most important thing is to figure out what problem you're really trying to solve.

Ali Niknejad's classes were what inspired me to go into RF design. I'd like to thank him for his help over the years.

Bora Nikolic has been very kind and supportive of me over the years. It was fun being a GSI for EE 140 when he was teaching it.

David Chen, Michael Mark, Toni Bjorninen, and Rikky Muller introduced me to brain-machine interfaces.

I'd like to thank Andrew Townley for many interesting discussions about RF, and having the patience to help me learn CAD Tools like HFSS.

Nai-Chung and Bo Zhao have renewed my interest in RFID due to their clever tag designs that I would have never thought of.

All of the BWRC **Staff** including. Brian Richards, Fred Burghardt, and James Dunn have been instrumental to helping me succeed in designing my chips and boards. Candy Corpus, Yessica Bravo, Olivia Nolan, and Leslie Nishiyama have made working at BWRC truly a joy.

Angie Wang for interesting conversations about life and giving me the an adobe illustrator file with the template for all the circuits I would ever want to draw. All my figures would probably look terrible without her.

Daniel Gerber, Andrew Townley, and Filip Maksimovic hosted the best Bro-B-Q's and Game-of-Bros parties at their house. Bouldering with them at the gym made me realize that I had a long way to go to improve my athleticism and grip strength.

Constantine Sideris showed me that just because you are an electrical engineer doesn't mean that you cannot push your body to its physical limits. He has been a great friend, and although we may have many philosophical disagreements about the optimal way to lift weights, he is a huge reason why I will always pursue both brains and brawn.

My brother Nicholas Sutardja has been a huge support though out this entire journey. Having a buddy to consistently hang out with during the day-to-day grind of a PhD has been invaluable.

Reinaldo Halim has been a great friend over the years. He has been living in Indonesia throughout most of my PhD. During many evenings of working late at the center, we were able to chat over Google Chat due to the time difference. Our deep conversations and joking antics made it feel like I always had a good friend by my side.

I am grateful to have Vena Chu by my side. For the past 2 years, she has been the best companion, and I cannot imagine my life without her.

I'd like to thank both my loving parents. My mother Weili Dai has always given care and support. And my father Sehat Sutardja has shown me that with clever thinking and hard work, any problem can be solved.

Chapter 1:

Introduction

Interfacing electronics with the human body is an exciting new frontier in biomedical engineering, healthcare, and science. Moore's law has miniaturized digital electronics to the point that energy-efficient, powerful computation is ubiquitous and affordable. Analog, mixed-signal, and RF design techniques have matured to the point of being able to reliably detect and condition relatively weak signals from the environment in the presence of large amounts of noise and interference. The timing is right for implants and wearable electronic systems to experience a quantum leap in practicality, functionality, and safety. Drawing on the advances in engineering of the past couple decades and applying them to the unique constraints and challenges of integrating electronics with human tissue can make this dream a reality.

This grand vision culminates in the Human Intranet [RAB1]. The Human Intranet is an electronics platform containing consisting of an ever-increasing amount of devices containing sensors, actuators, computation, storage, and energy nodes [RAB1]. A vast variety of sensors including electrodes and LED's for measuring various vital signals are connected through a robust, efficient network to improve healthcare and wellness. Brain-machine interfaces enabled by neural recording and stimulation is one of the most exciting aspects of the human intranet, yet one of the most challenging to implement in a reliable and practical way.

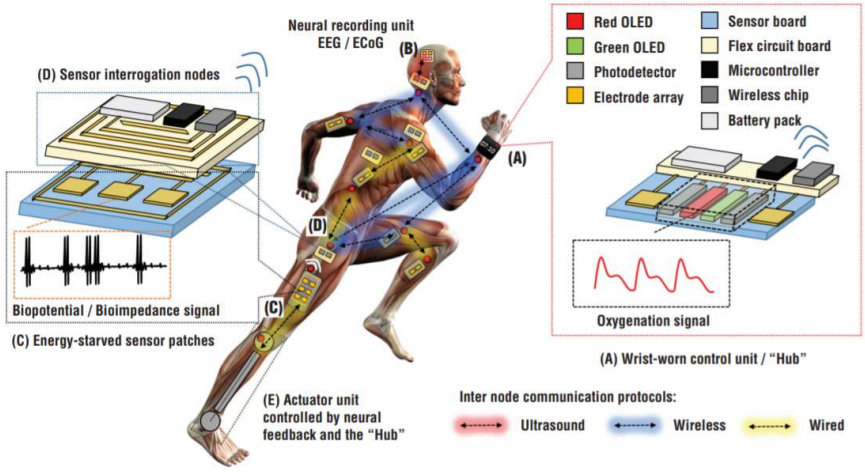

Figure 1-1: Human Intranet [RAB1]

1.1 Brain Machine Interfaces

Brain machine interfaces (BMI) have the potential to revolutionize healthcare and neuroscience. Out of all the human body's organs and vital structures, the human brain is one of the least understood by science, yet the nervous system is essential for the operation of every aspect of the human body. Fig 2. shows an example diagram of BMI system. Signal acquisition front-ends acquire neural signals from brain, which are digitized further decoded into certain actions using signal processing. The results of this signal processing can be used to provide control signals for prosthetics, computers, or they could be monitored by physicians to help treat certain neurological diseases. The feedback in such a system can come from visual perception or from tactile and proprioceptive feedback, but for people who has lost such functions, electrical stimulation of regions of the brain associated with these functions can be used instead [JOH].

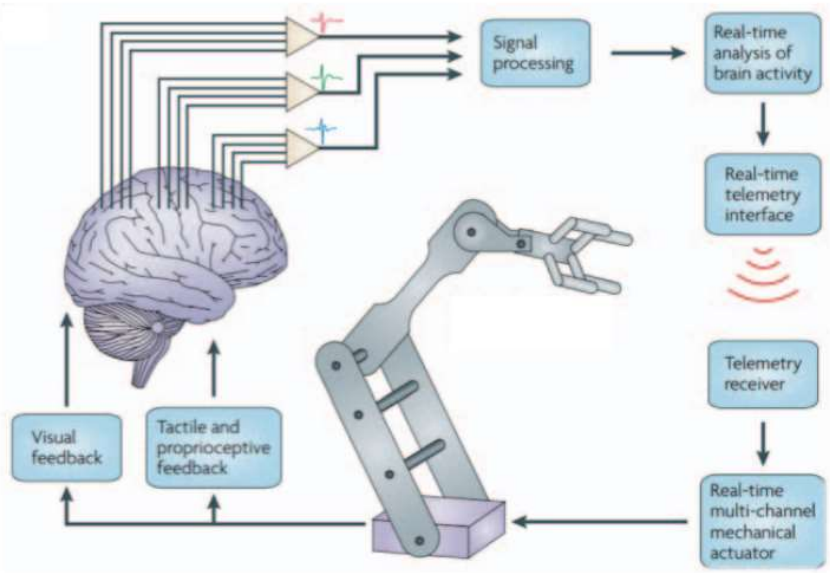

Figure 1-2: Brain machine interface [NIC1]

1.1.1 Recording and Stimulation

Two key components of Brain Machine Interface (BMI) systems are sensing and actuation. Implanted electrodes measuring the electrical activity of the brain can provide control signals for control of BMI systems, and can also provide stimulation to the brain used to close the feedback loop shown in Fig. 1-2. Sensing methods such as state-of-the-art near-infrared spectroscopy require seconds to generate command signals, while electrical signals such as Electrocorticography (ECoG) and Action Potential (AP) are able to record high resolution neural data on a millisecond timescale. Using electrodes for both recording and stimulation is the primary method for real-time control of BMI systems [BRAN].

One current standard for neural recording for BMI experiments is the Utah array. The array, shown in Fig. 1-3 is 4.2 x 4.2 mm wafer with 100 shanks, each of which is 1 – 1.5 mm long, separated by a 400 um pitch. The tip of each shank contains a conducting electrode. Neural recordings are transmitted from each electrode to external amplifiers by cables traveling through the skull. These electrodes can record action potential events from small groupings of individual neurons at a millisecond time-scale [MAY]. Fig. 1-3 also shows other devices containing electrodes such as the Michigan probe [HAR] and the Plexon Microwires [NIC2].

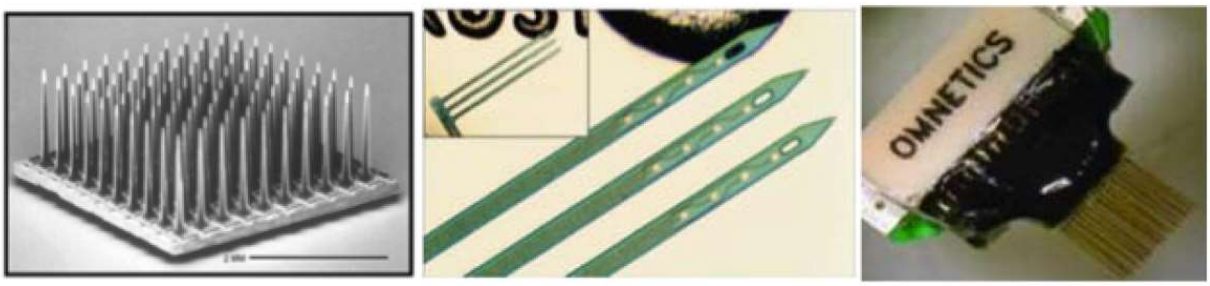

Figure 1-3: Various wired neural probes. a) Utah Array [MAY], b) Michigan Probes [HAR] c) Plexon Microwires [NIC2]

1.1.2 Neural Prosthetics

There are millions of people worldwide who suffer from a spinal cord injury (SCI) [NAT], and there are nearly 2 million people living with limb loss in the United States alone [ZIE]. For those with spinal cord injuries or amputated limbs, regaining motor function can hugely improve the quality of life for these patients. Neural prosthetics powered by BMI have greatly improved over the past few years. Fig. 1-4 shows various applications of neural prosthetics. These prosthetics often require high resolution neural data that only implanted electrodes can deliver [BRAN].

Neural prosthetics take all kinds for forms and sizes. The Braingate group is a collaborative effort involving neuroscientists, engineers, neurosurgeons and other researchers from a consortium of multiple academic and VA institutions. Its goal is to restore motor function, communication, and independence of people with neurological disease, injury to their nervous system, or limb loss. In [AJI], researchers involved with Braingate developed a system that combines neural recording and muscle stimulation to restore reaching and grasping movements in a man paralyzed from the shoulders down from a previous biking accident. Dexterous control of motor prosthetics was demonstrated [HOC], where a woman with tetraplegia used an intracortical brain computer interface to control a robotic arm to pick up and drink a bottle of coffee. This was the first time in over 14 years that she was able to voluntary reach out and take a drink without assistance from others. Successful control of motor prosthetics has been replicated in other research as well. In [COL], a woman with spinocerebellar degeneration was able to control a robotic arm with seven degrees of freedom. And [AFL] demonstrated that a man with SCI was able to use recordings from the posterial parietal cortex to control a robotic arm.

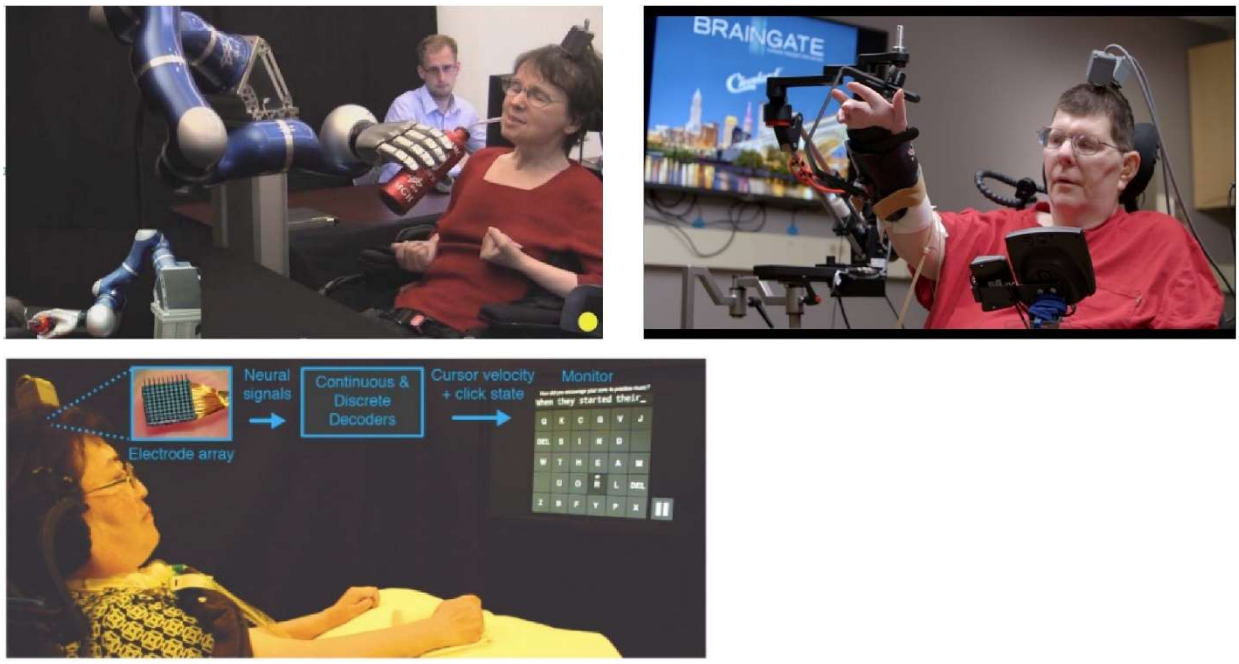

Figure 1-4: Neuroprosthetics controlled by BMI a) A tetrapeligic woman drinks water by controlling a robotic arm [HOC] b) A man with spinal cord injury uses BMI to stimulate and control hand [AJI] c) BMI allows woman to communicate by using computer keyboard [PAN]

Other forms of non-motor prosthetics have been developed. In addition to loss of movement, patients with paralysis also often have trouble using technology such as computers and communicating with others. In [PAN], researchers developed a brain computer interface that uses neural recordings from local field potentials and action potentials to provide point-and-click control of a computer cursor. A woman diagnosed with ALS was able to use this interface to type over 24 characters per minute to answer questions posed to her by researchers.

Although these results in restoring function in paralyzed patients are remarkable, all these systems have one common shortcoming. The electrodes used for neural recording are connected from the brain to the outside world using wired connections. Using a bulky wired BMI system in a lab setting is fine for proof-of-concept experiments that explore the nuances of translating neural signals into control of a prosthetic. But a wireless BMI system would make these treatments available for daily, practical use by the masses.

1.1.3 Treatment of Neurological Disorders

Long-term recording of neural signals is a practical method to monitor the condition of patients suffering from various neurological disorders such as seizures, Parkinson's, and Alzheimer's. In some cases, closed loop brain stimulation can even help to treat the severity of these diseases. Recent advances in neural implants have demonstrated treatments for neurological diseases that involve both neural recording and stimulation [JOH].

Epilepsy is one of the most commonly-occuring neurological disorders, affecting nearly 1% of the world population. Surgery is an effective treatment for intractable epilepsy, but the success of the surgery is highly dependent on identifying the seizure onset zone. Localization of the region of the brain responsible for seizures is usually done by implanting large wired electrode arrays to record Electrocorticography signals (ECoG) of the patient for a period of weeks [ENG]. The wireless uECoG implant developed in [MUL2] makes this type of chronic neural recording far more convenient for daily wear, reducing the risk of infection for those who are considering surgery for epilepsy.

Neuropace has recently developed an implantable device called the RNS Stimulator, shown in Fig. 1-5, that combines neural recording with direct brain stimulation to effectively treat epilepsy. The cranially implanted neurostimulator continually senses ECoG signals, and is programmed by a physician to detect abnormalities in the ECoG. In response to these abnormalities the RNS system provides electrical pulses aimed at mitigating the effects of seizures or even preventing them entirely. In clinical trials, the neurostimulator has been shown to reduce seizures by over 44% after one year and 53% after 2 years [HEC]. Recently, Neuropace has announced the RNS Tablet, an internet-connected platform with an easy-to-use UI for easy access to patient ECoG data.

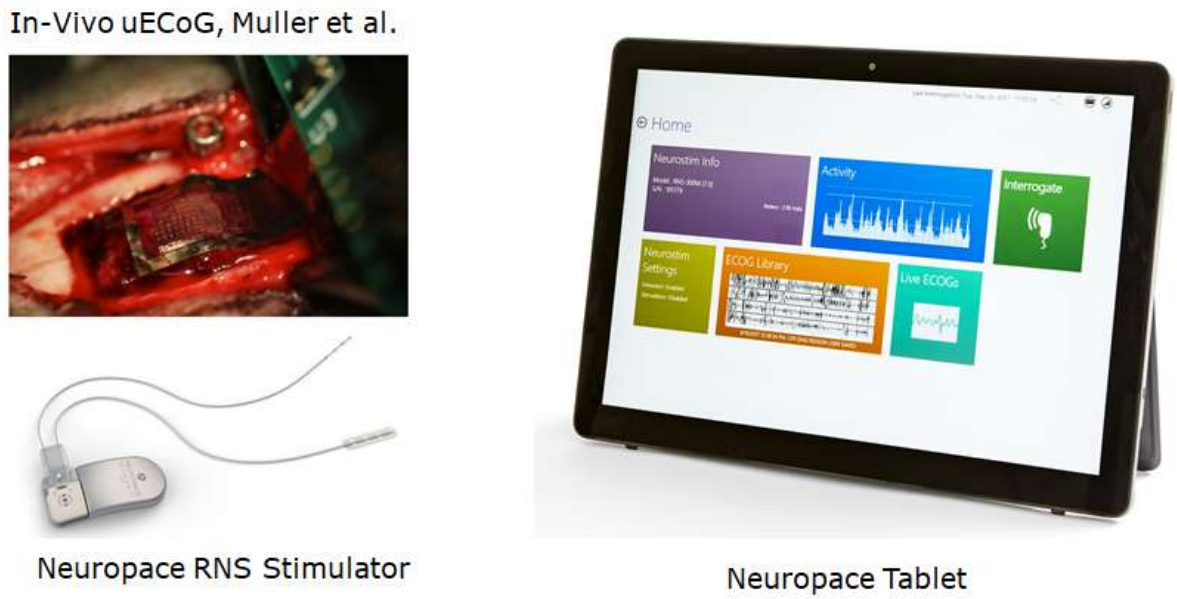

Figure 1-5: Recent advances in ECoG recording for seizure detection. [MUL2, HEC]

The growing understanding of the brain from neural recording technologies recently enabled treatment of various neurological disorders using a technique called deep brain stimulation (DBS). DBS involves interfacing and intervening with the nervous system through electrical means in order to treat Parkinson's disease, tinnitus, sensory disabilities, chronic pain, and a whole host of other conditions. Fig. 1-6 shows a schematic of the brain detailing the locations of electrode arrays implanted for the purposes restoring hearing and treating tinnitus [JOH].

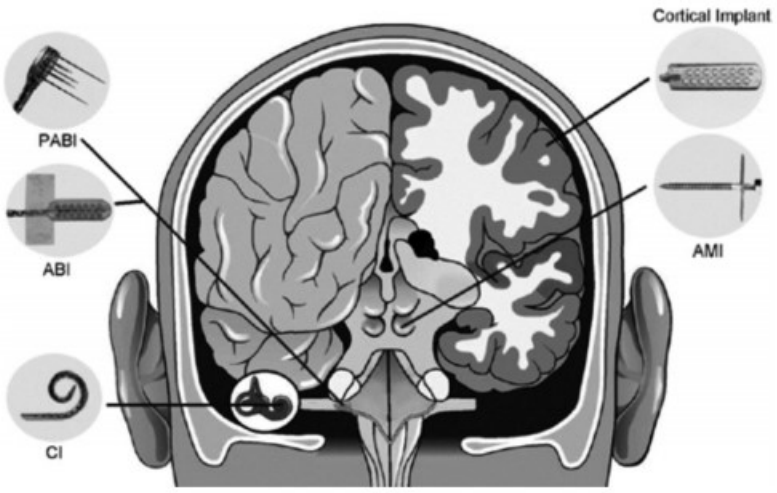

Figure 1-6: Implants using DBS to treat tinnitus and restore hearing [JOH]

1.2 The Need for Wireless BMI

Wireless powering and communications is an important feature for widespread adoption of BMI systems. Wireless communications through the skull removes the needs for transcranial wires that could increase the risk of infection. Having an external reader deliver wireless power to the implant would also eliminate the need for frequent surgeries to replace the implant's battery.

In recent years, much attention has been to the implants of wireless BMI system, but less focus has been put on designing the external reader meant to power and communicate with them. An external reader should be able to safely deliver power to a BMI implant, while reliably receiving uplink data from it. To create a BMI system that patients want to use, the reader must be compact and efficient. It has to be a device that people actually want to wear on top of their head.

1.2.1 Power Delivery

In [RAB], it was shown that electromagnetic power sources were determined to be able to deliver 2-3 orders of magnitude higher power to implants inside the skull. Implants can derive their own power supply by rectifying an external RF carrier.

The FCC sets the maximum amount of power allowed to be transmitted inside the human body for each wireless frequency based on health concerns such as heating of tissue by electric and magnetic fields [FCC]. In [MARK2], it was determined that the maximum amount of power available for a sub-cranial implant depends on the available area inside the skull for a coil to receive the power. The quality factor (Q) of the implanted coil determines the efficiency of power transfer through skull. Smaller coils have lower Q at lower frequencies, while larger coils have high Q at lower frequencies. In addition, loss through human tissue and the skull generally increases as frequency

increase. Based on these observations, it is observed that using lower frequency carriers make more sense when powering larger coils, and using higher frequency carriers are more efficient at delivering power to smaller coils.

1.2.2 Uplink Data Rate

The required data rate of wireless BMI systems is dependent on both the type of neural recording modality and the number of sensor sites. While surface recordings such as ECoG require a bandwidth of only 500 Hz, recordings from individual neurons such as AP have a bandwidth from 250 Hz-10 kHz. For example, a 64-channel ECoG array digitized at 10 bits of resolution would require a data rate 3.2 Mb/s, while a 100-channel AP array digitized at 10 bits would require a data rate of 100 Mb/s [MUL1].

1.2.3 Wireless Implants

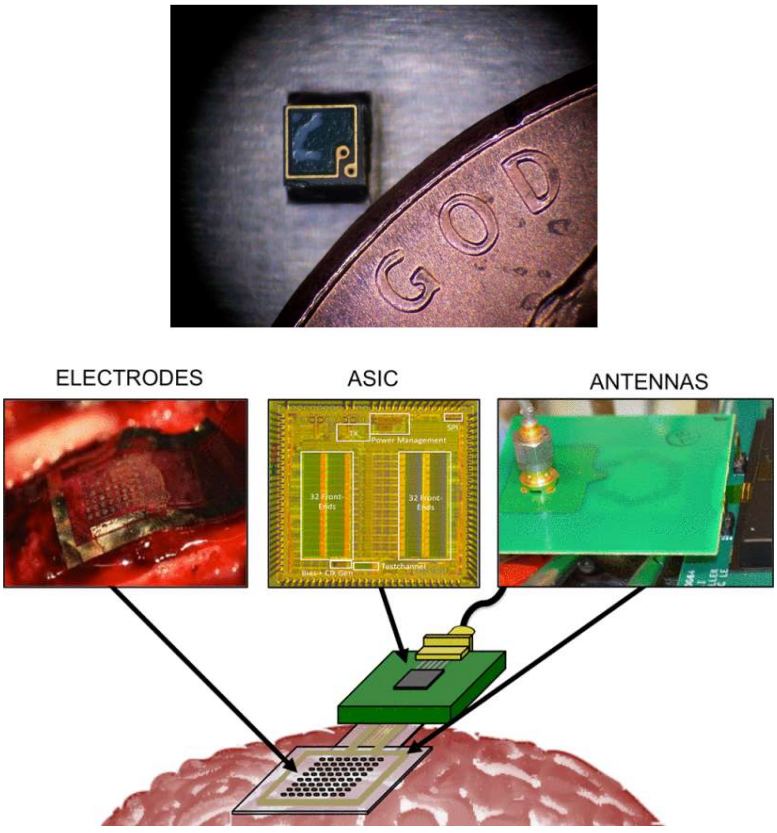

Figure 1-7: 1 mm^3 neural transponder (top) [MARK1] and wireless uECoG implant (bottom) [MUL2]

In [MARK1], researchers developed a 1 mm^3 neural transponder with a wireless radio consuming only 330 pJ/bit energy per bit [CHEN1]. Although there is no circuitry for neural monitoring or

stimulation on this implant, the prototype demonstrated the limits of efficiency for low-power radios implanted inside the skull.

The system in [MUL2] demonstrated an implantable wireless uECoG implant for the purposes of long-term neurological recording for monitoring of various neurogical disorders such as seizures and Alzheimer's disease. The implant consists of a flexible antenna and a electrode array printed on a flexible substrate and an IC capable of recording 64 channels of ECoG data. The chip derives its power from an external wireless source and can send neural data through a wireless uplink at a rate of 1 Mb/s.

1.2.4 Neural Dust

Feasibility of less-than-mm-sized ultrasonic sensor motes that derive power from an ultrasonic interrogator are shown in [SEO]. This "Neural Dust" can detect neural signals and backscatter them back to the interrogator. Because ultrasound has far less loss in water than RF, this allows implants with neural acquisition to be placed far deeper into tissue than before. Also, ultrasound has a smaller wavelength in water than air, and efficiency of energy harvesting depends on how close the transducer is to the wavelength of the energy source. This form factors of "Neural Dust" can be much smaller. Fig. 1-8 shows a demonstration of neural dust motes measuring EMG and ENG to from a mouse's leg and backscattering the measurements to the reader.

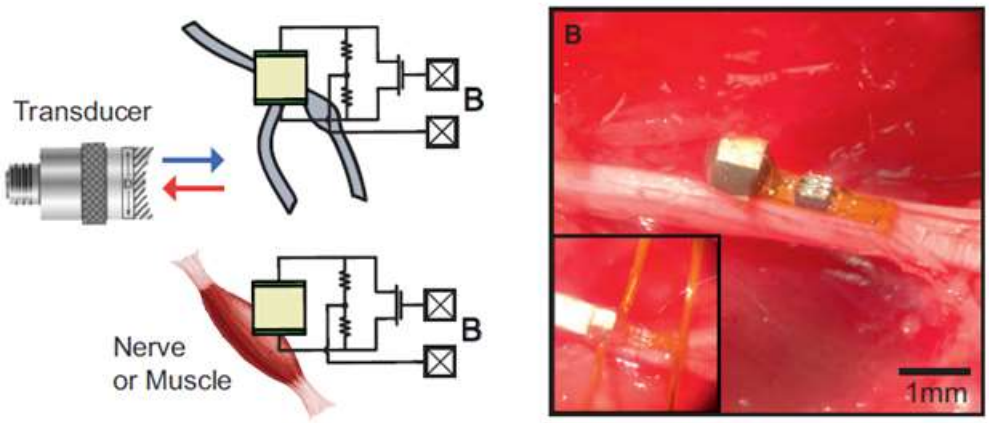

Figure 1-8: In-vivo neural recording in mouse leg using ultrasonic motes [SEO]

These advances in ultrasound implants make it even more important to be find a way to deliver RF power wirelessly through the skull to neural implants. Even though ultrasound has low loss in water, it has difficult propagating through the skull. Ideally, wireless powering and communications through the skull can be used to deliver power to and interrogate large implants on the surface on the brain. These implants can then generate ultrasound waves to interrogate and power neural dust.

1.3 Radio Frequency Identification

Radio-frequency Identification (RFID) is a communications technology used when one side of the link has access to far more energy resources than the other. An RFID reader sends a wireless carrier to a tag, which the tag can reflect back to the reader by modulating its own antenna impedance to send back uplink data. The tag can also use this wireless carrier to derive its own power supply if necessary [FIN].

This technology is commonly used for inventory or identification purposes where the "tag" can be a disposable sticker on an object or a smart card held by a person. For reasons of cost and practicality, these tags have small or zero energy reserves on the devices. On the other hand, these tags are commonly read by an interrogator or reader that has its own power source and complex circuitry. Shown in Fig. 1-9 are some common applications of RFID.

Figure 1-9: Common applications for RFID [FIN]

These system constraints are conveniently similar to that of a wireless brain-machine interface with implanted device for neural recording. Communication using RFID backscattering is well-suited for a data link through the skull. The external reader on top of the head provides a carrier to the tag underneath the skull, and the tag passively modulates its own impedance to communicate with the reader. The tag can then use this carrier to derive its own power supply.

1.3.1 State of the Art

Existing systems use frequencies from 13.56 MHz – 50 MHz for power and data communications in order to maximize the amount of power transfer through the skull. At these frequencies, coupling through the skull is near field (wavelength of light at 30 MHz is 10 meters in a vacuum, while a skull is ~ 1 cm thick). As a result, the power transmit coil at the top of the head and the power receive coil inside the skull are near-field coupled. In this regime, coupling efficiency is highly dependent on the Q of the inductive coils used in the link.

However, backscattering systems suffer from TX-to-RX carrier leakage that may saturate receiver front-ends, and excess phase noise from the TX that can lower receiver sensitivity. Implanted tags with separate coils for powering and data telemetry like [KIA,RUSH] take up too much space inside the skull. Some systems [KIA,RUSH] have the tag generate a new carrier frequency for data before communicating, but that results in increased implant complexity, and a link that is difficult to optimize for both powering and data communications.

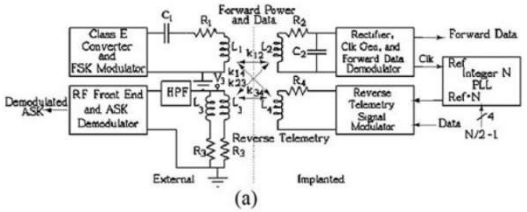

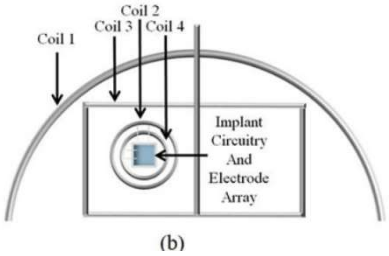

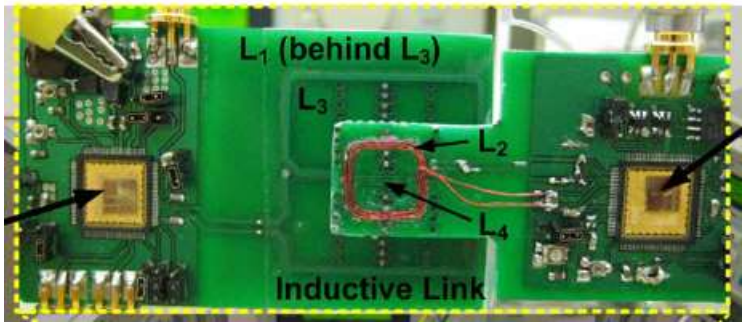

Figure 1-10: Near-field inductive link using separate transmit and receive coils [RUSH]

Although these systems have high link efficiency, the size of the external coil is 3 cm, and the size of the implanted coil is over 1 cm. These systems are suited for BMI systems that require lots of

power such as neural stimulation or perhaps powering an implanted ultrasonic interrogator to power ultrasonic motes like the ones shown in [SEO].

1.4 Thesis Outline

The primary goal of this work is to describe the methodology for a compact and efficient design of a transcranial RFID reader that wirelessly powers brain implants while receiving backscattered neural recording data from that same implant.

Chapter 2 gives an overview of self-jammer cancellation, one of the primary hurdles of RFID design. It defines the link budget and system constraints required to design a functional backscatter link. Classical and state-of-the-art methods of removing the self-interference are analyzed for feasibility in a practical trans-cranial link. A design example of an RFID Reader, built from off-the-shelf components, meant to power and communicate with a 1 mm^3 330 fJ/bit transponder for implanted neural sensors [MARK1] is presented as a proof of concept for these design principles. While able to demonstrate the functionality and prove the feasibility of the miniature transponder, the external reader is bulky and impractical for daily wear for patients using BMI.

The need for a wearable and efficient RFID Reader for Brain Machine Interfaces motivates the design of a blocker rejection method that does not require bulky external components. Chapter 3 explains a novel RFID Reader architecture that uses a Class E/Fodd PA to simultaneously transmit a power carrier to the tag while demodulating the its backscattered signal. Using these principles, a proof-of-concept fully-integrated RFID Reader, meant to wirelessly power and receive data from mm-sized neural implants is described.

Chapter 4 details the measurement results of in-vitro system tests using a prototype radio built using the IC in chapter 3. Practical concerns of PCB level antenna optimization and matching network design are detailed. The components of the RFID reader and tag system are tested with an in-vitro mock-up of human skull tissue using cuts of meat and bone from the grocery store. And the measurements from these tests and over-the-air tests are included.

And finally, future directions, possible improvements, and conclusions are discussed in chapter 5.

Chapter 2:

RFID Readers for Brain Machine Interfaces

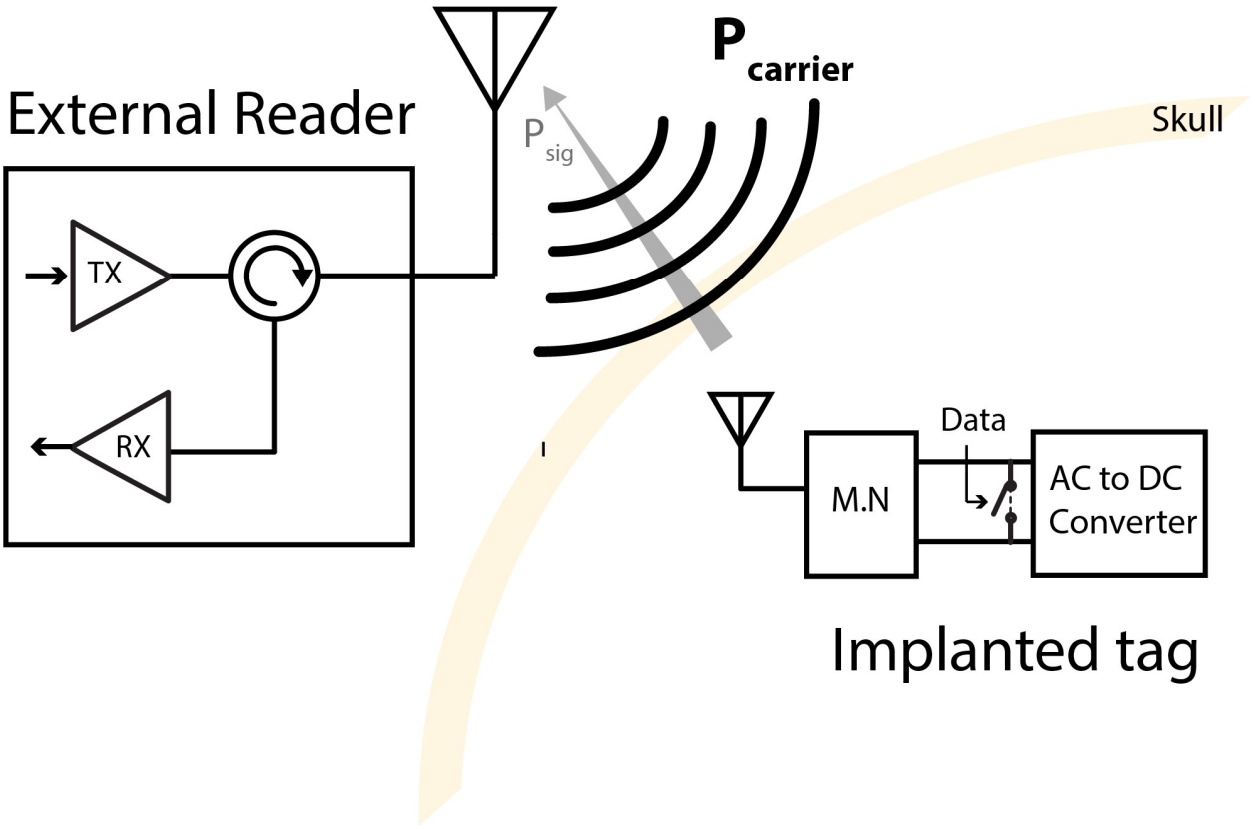

Figure 2-1: RFID reader for power delivery/data communications with neural implant

Systems using RFID backscattering have been shown to enable communications between a reader with access to lots of power resources and inexpensive tags with no battery of their own [FIN]. This chapter focuses on addressing the many challenges involved in implementing an RFID communications scheme in a wireless BMI system. Fig. 2-1 demonstrates the principles of operation for an RFID system for Brain Machine Interfaces. The reader transmits a sinusoidal carrier to the tag, and the tag communicates to the reader by modulating the impedance of its antenna, also called backscattering. To prevent the need for regular surgery to replace batteries, the implanted tag can use AC-to-DC conversion to derive its own power supply from the reader. The power available to an RFID tag can be expressed as

$$P_{Tag} = P_{TX} \times L_{Channel} \times Eff_{RF-DC} \quad (1)$$

where P_{TX} is the transmitted power, L_{Chann} is the loss of the channel, and Eff_{RF-D} is the efficiency of the RF-DC Converter of the tag. This power can be stored on a capacitor for use in communications, signal acquisition, and neural stimulation.

2.1 Blocker Rejection

The primary issue with backscatter recovery for RFID Readers is leakage of the transmitted carrier into the reader's own receiver. This large signal can saturate the receiver's LNA, and noise from the carrier can desensitize the entire receiver. The transmitted carrier is often orders of magnitude larger than the received backscattered signal because reader receives a heavily attenuated signal that experiences the path loss of the link in both directions.

2.1.1 Spectral Content of Backscattered Data

Backscattering is a passive form of communication that does not require the tag to have a PA or generate its own carrier frequency. A reader interrogates the tag by sending it a continuous sine wave. The tag modulates the impedance seen by its own antenna using an encoded form of the data it intends to transmit, resulting in a change in the radio wave reflected back to the reader. Amplitude shift keying (ASK) is one of the simplest and most efficient modulation schemes to implement on a tag. All the tag needs to do to communicate is short its own impedance using a switch that is controlled by the backscatter data.

The spectrum of various backscattered signal is shown in Fig. 2-2. The power spectral density of standard NRZ encoding is concentrated near the frequency of the carrier. Other forms of binary data encoding effectively shift most of the power of the backscatter data P_{sig} to be centered at a frequency f_{mod} away from the carrier, spectrally separating the data from the carrier P_{TX} [FIN]. The encoded data has a higher switching rate than the original NRZ encoding, resulting in more power being used in the tag to modulate its impedance. This frequency shift can be also be performed by mixing the encoded data with an IF frequency, but this requires the tag to generate its own IF carrier.

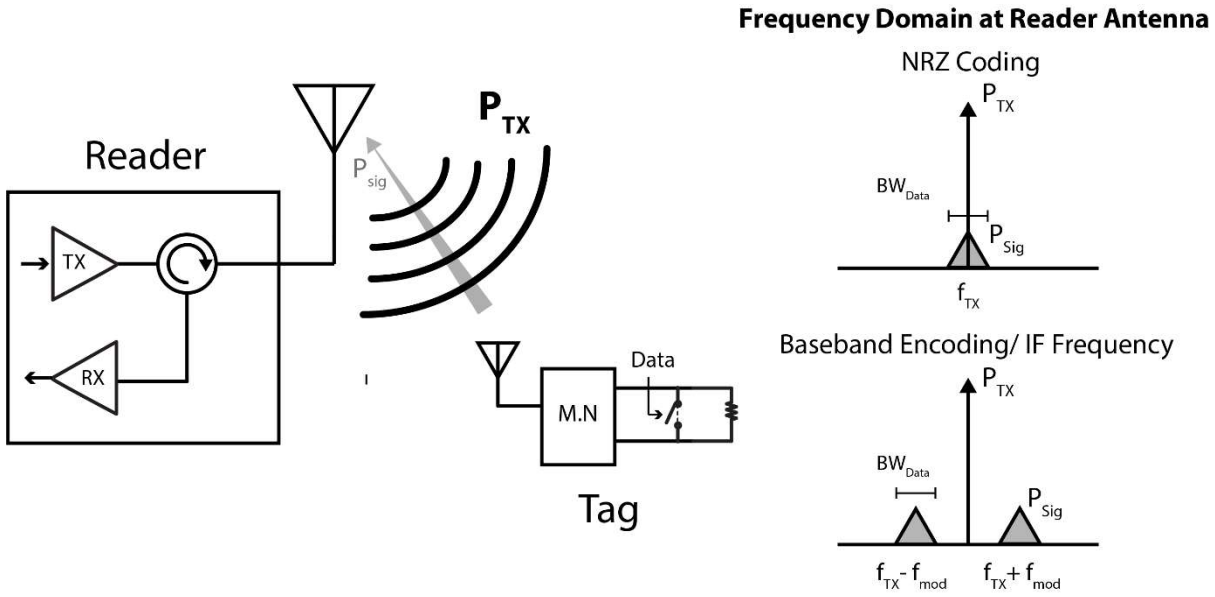

Figure 2-2: Illustration of backscattered signal spectrum

To recover the backscatter signal P_{sig} without saturating the receiver, the RFID reader has to lower the strength of the interferer P_{TX} while maintaining the SNR of P_{sig}. Simply attenuating the signal before it reaches the RX would lower the SNR of the received backscattered data.

Conceptually, a high-Q band-reject filter can be placed before the input of the RX to reject the interferer. However, implementation of this filter is often impractical. Either off-chip components such as high-order LC networks or high-Q external SAW filters would be needed. High-order LC filters are susceptible to variance in their L and C values, and cannot be adjusted once implemented. Similarly, SAW filters are electromechanical structures that have physical dimensions designed for specific frequency bands, so they are also inflexible.

2.1.2 Circulator

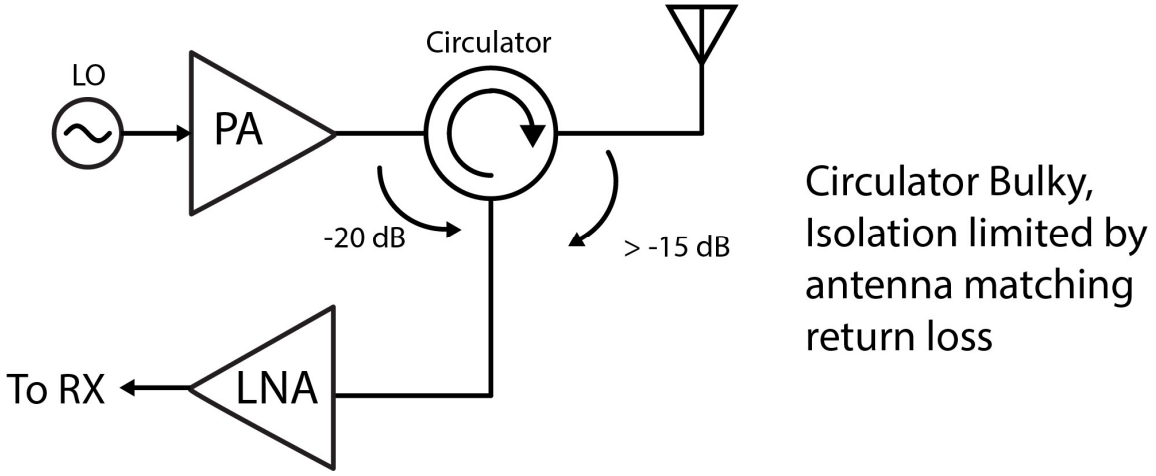

Figure 2-3: Blocker cancellation in an RFID reader using circulator

One common method of blocker rejection is to use a circulator. A circulator is a three-port device that ensures power flow in one direction, and isolates the first port from the third port. Shown in Fig. 2-3, when the transmit power amplifier is connected to port one, the antenna is connected to port two, and the receive chain is connected to port 3, the receiver is isolated from the transmitter. However, the isolation between ports 1 and 3 is finite, typically being < 20 dB for most commercial circulators, so there is still considerable leakage that could desensitize the amplifier. In addition, circulators are large off-chip components that are made out of ferromagnetic material, so they increase the form factor of the reader and are difficult to integrate on chip. For an external interrogator that is meant to be worn on top of the head, this architecture would be far too bulky.

Even if the circulator has perfect isolation, practical matching networks for antennas have finite return loss. It is difficult to achieve better than 15 dB return loss for a matching network at most commonly used carrier frequencies for wireless data communications. As a result, the leakage power at the input of the LNA in an RFID system using a circulator can be expressed as

$$P_{interferer} = P_{PA} \times (G_{Circ} + RL_{MN}) \quad (2)$$

Where G_{Circ} is the isolation of the circulator and RL_{MN} is the return loss of the matching network due to imperfect matching beween the antenna and the circulator. It is important to note that there could be a phase offset between G_{Circ} and RL_{MN} depending on the implementation of the matching network.

2.1.3 Active Cancellation

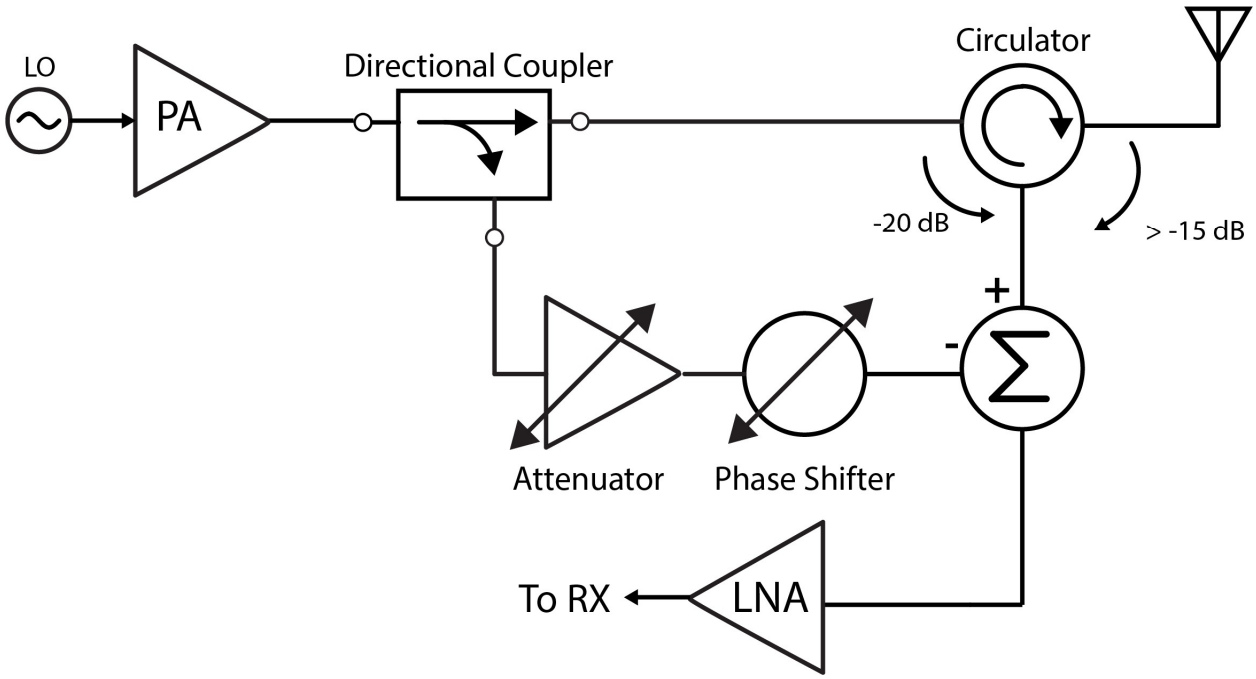

Figure 2-4: Active Cancellation Block Diagram

One of the convenient aspects of backscatter communications is that the reader already has a copy of the transmitted carrier at its exact frequency. If a scaled and phase-shifted copy of the transmitted carrier signal is combined with the received backscatter signal before the input of the receiver LNA, any transmit leakage will be cancelled out before it can rail out the receiver. If the transmit leakage comes from multiple sources (i.e. limited circulator isolation or finite return loss of antenna matching network), active cancellation can still cancel out the received signal because the sum of multiple sinusoid of the same frequency, regardless of phase or magnitude, is another sine of the same frequency.

For a wireless brain machine interface system, active cancellation is best used combined with a circulator to further increase the external reader's robustness against self-interference. Employing active cancellation without a circulator would require the reader to generate a copy of the carrier of the same power but opposite phase as the transmitted carrier. This would effectively cut the efficiency of the reader's carrier transmit chain in half because every transmitted carrier would need an equally large copy of itself to cancel it out.

Fig. 2-4 shows a block diagram of an RFID reader system employing active cancellation. A directional coupler sends the majority of the TX power to the circulator on its way to the antenna, while the remainder of the power (<-10 dB of the PA output) is sent to a cancellation path. The cancellation path has a programmable attenuator and phase shifter that can be adjusted so that its output is opposite in phase and equal in amplitude to the carrier leakage, caused by the circulator and non-ideal matching to the antenna, into the RX path. These two paths are then summed together using a power combiner.

The effectiveness of active cancellation of the self-jammer of the reader depends on the resolution of the programmable phase shifter and attenuator. The effect of this non-ideality is plotted in Fig. 2-5, which is taken from a system using active cancellation for the purposes of image rejection [CHEN1]. As seen in the plot, if resolutions of less than 0.2 dB amplitude imbalance and 1 degree of phase imbalance can be achieved, cancellation of the self-jammer can exceed 35 dB.

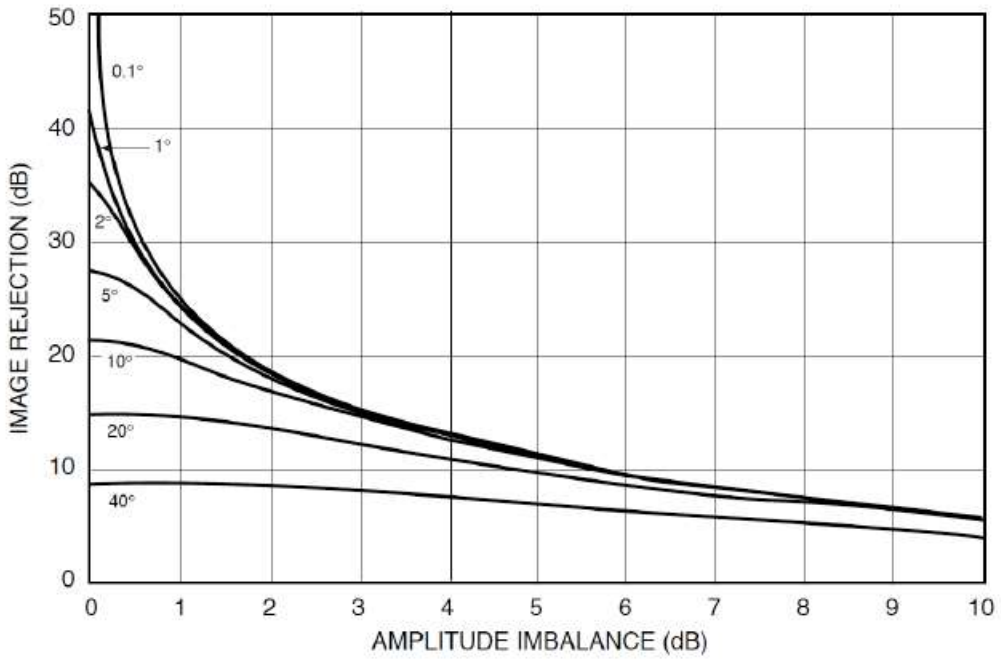

Figure 2-5: Interference Suppression vs Phase and Amplitude Imbalance [CHEN1]

Recently, [CAL] has demonstrated a full duplex transceiver employing active-cancellation using a current-based DAC to cancel out any transmitted data to enable full duplex communications. Using a DAC-based cancellation is overkill for an RFID system meant to only be full duplex in the sense that it is only transmitting a single power tone while receiving a backscatter. But the transformer-based current summation methods in [CAL] could allow for more effective blocker cancellation in RFID readers.

2.1.4 Separate Antennas

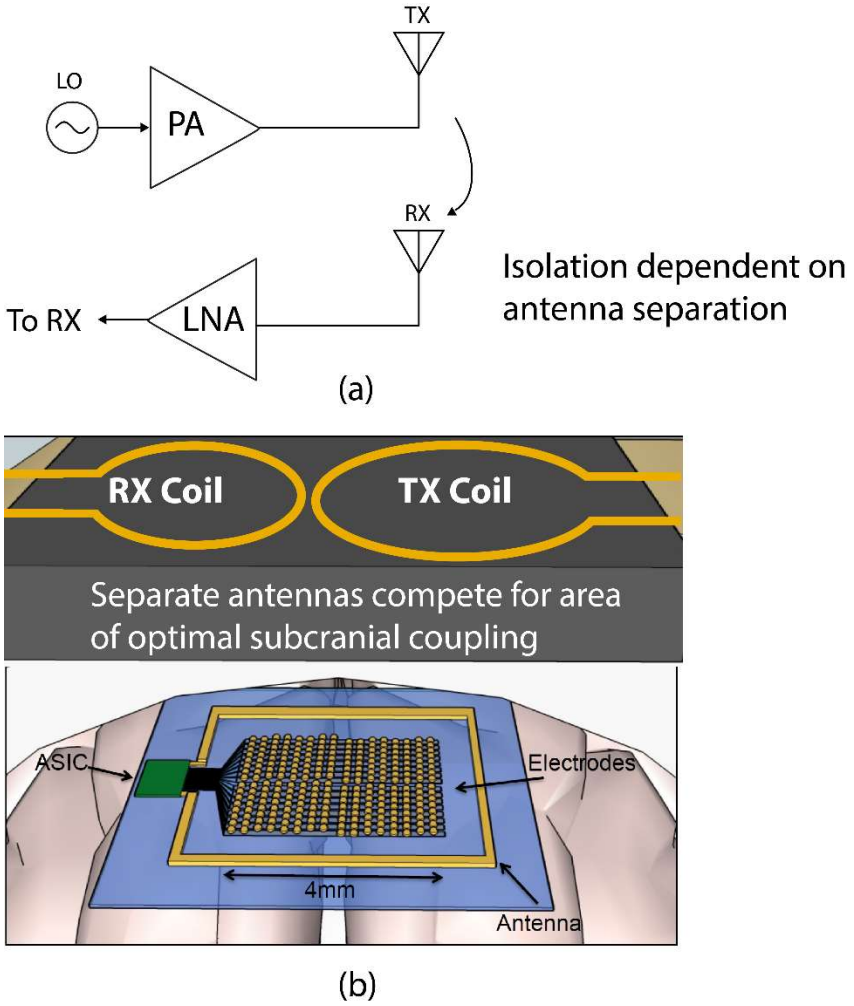

Figure 2-6: (a) Antenna Isolation dependent on separation between RX and TX coil. (b) Both RX and TX coils compete for space on top of skull for face-to-face coupling with implant.

One technique to protect against self-interference is to use separate antennas for transmit and receive chains of the reader. This method makes it so that there is no direct electrical connection between the large sinusoidal carrier in the TX and the amplifiers and filters of the RX chain. Aside from a wireless system using two antennas being costly and bulky, this configuration isn't well-suited for trans-cranial powering and communication.

Isolation between two antennas scales with the distance between them. However, in a trans-cranial link for a BMI system, the transmit loop antenna must be placed on top of the head, directly above the implant, to optimize power delivery to the implant. Shown in Fig. 2-6, an arrangement of two antennas leaves no room for a separate receive antenna with a direct line-of-sight coupling to the tag. Either the transmit antenna has to shrink or shift, lowering the

efficiency of the power delivery, or the receiver has very weak coupling to the implant, greatly lowering the strength of the received backscattered signal.

2.1.5 Mixer-first implementations:

For the past decade, CMOS mixer-first RF receiver topologies have been shown to be good at rejecting out-of-band interference without requiring bulky external SAW Filters [AND], especially in receivers that don't need to have extremely low noise-figure. Shown in Fig. 2-7, n-path filters have been shown to be able to create flexible band-pass transfer functions using primarily CMOS switches and capacitors, while consuming only a small amount of area [KLU]. In a mixer-first architecture, the first block in the receive chain is a CMOS passive mixer instead of an LNA. This down-converts the received signal down to DC or to a lower IF frequency before amplification. Because the devices in the front-end are used as passive switches and the frequency translational properties of the switches allow for high-Q bandpass filters to be constructed in a small amount of are, out-of-band blocker rejection as high as +26 to+36 dBm IIP3 have been reported [KLU].

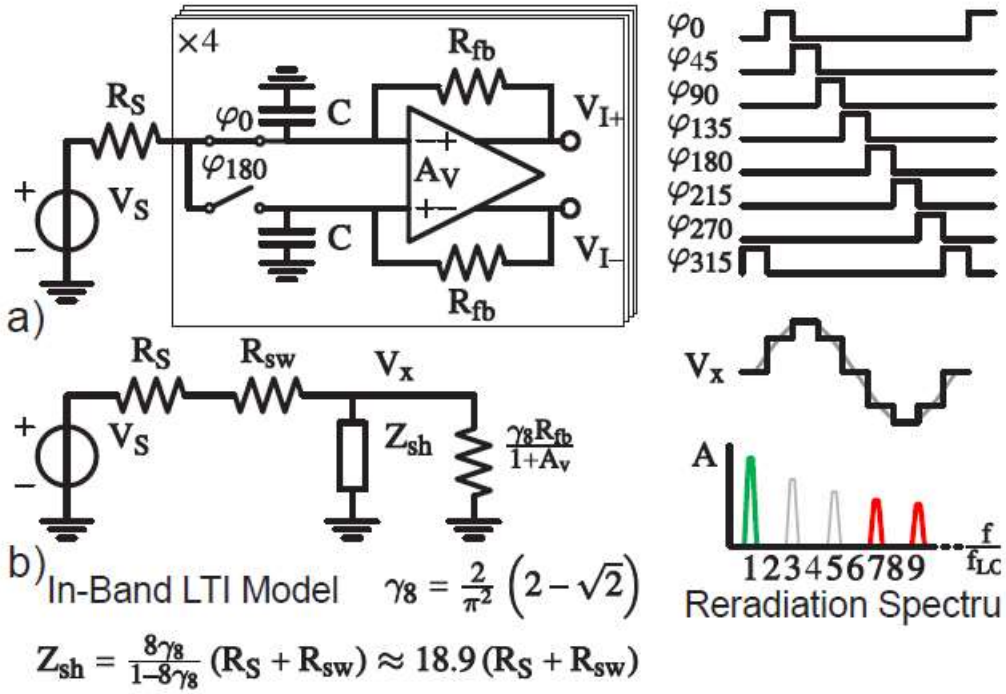

Figure 2-7: Use of n-path filters with many phases of the same clock to construct complex baseband filters.

In Fig. 2-8, a passive mixer-first LNA front-end is proposed for a UHF RFID reader [LIN]. Using the frequency translation properties of passive mixing, [LIN] is able to create a receiver without an external matching network. However, the P_{1dB} of the structure is only at -8.3 dBm, so a circulator or directional coupler is still needed to isolate transmit from receive. For wireless

BMI implants like those shown in [MUL1] and [MARK1], transmit powers of greater than 10 dBm are required to power the implants through the skull.

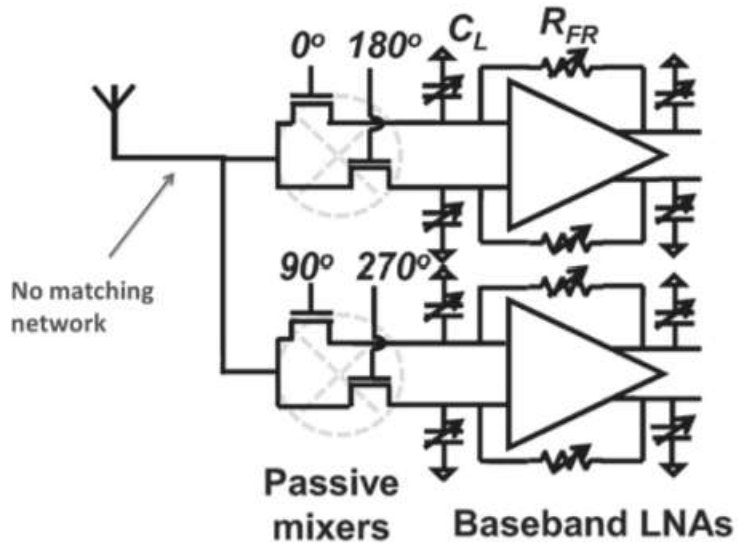

Figure 2-8: Passive mixer receive front-end for UHF RFID Reader [LIN]

What causes the P1dB to be so low? Even though passive mixers are great for out-of-band filtering, in-band blockers are still subject to the non-linearity of the RX amplifiers [AND]. RFID carrier self-jammer is considered an in-band blocker. Recent advances such as [KUO] attempt to use non-linearity of translate the frequency of the backscatter so that it is out-of-band compared to the blocker.

2.1.6 Separate Data and Power Carriers

Separate carrier frequencies can be used by the reader for power delivery and data communications. This is not technically an RFID backscattering scheme because the implant would need to generate a separate frequency for communications. This method would make separating interference from the desired signal to be as simple as using a band-pass filter. However, the remotely-powered implant need additional circuitry to generate is own carrier for communicating on a different band. This can increase both the power consumption of the implant, and it might also increase the form factor because the implant would need some sort of reference and/or PLL to generate a spectrally pure carrier. For a standard RFID Reader, the recovered backscattered signal can be approximated as (assuming low loss in the receiver)

$$P_{RX} = P_{Tx} \times L_{cha}{}^{2} \times G_{tag}{}^{2} \times d_M \quad (3)$$

Where P_{TX} is the transmitted power, G_{Tag} represents signal gain/loss from the tag's RF front-end and finite modulation depth. Because it's a backscattering system, the channel loss $L_{Channel}$ is experienced twice by the signal.

If the tag has to generate its own carrier at a different frequency, another source of loss comes into play: the efficiency of the tag's RF-DC rectifier Eff_{RF-DC}. The expression in (3) then becomes

$$P_{RX} = P_{TX} \times L_{ch,f1} \times G_{tag,f1} \times Eff_{RF-DC} \times Eff_{tag} \times G_{tag,f2} \times L_{ch,f2}. \quad (4)$$

Two frequencies are used so the channel loss $L_{ch,f1}$ and tag antenna gain $G_{tag,f1}$ for the power frequency are different than the $G_{tag,f2}$ and $L_{ch,f2}$ of the data frequency. The term $Eff_{tag,TX}$ encapsulates all losses associated with carrier generation, signal processing, and data transmission associated with the tag transmitting on a different data frequency.

Because all the power comes from the reader, the terms above effectively lower the strength of the received signal for the same amount of transmitted power. Near-field power delivery systems that have a large amount of power to the implants such as [RUSH] and [KIA] (> 10 mW) can afford this loss in order to increase data rate of the backscatter by using a carrier frequency for the data backscatter that is much higher than the carrier frequency used for power. Fig. 2-9 shows the powering and communications architecture used in [RUSH]. As stated in Chapter 1, these systems trade-off power available to the implant for a larger coil size for both reader and receiver.

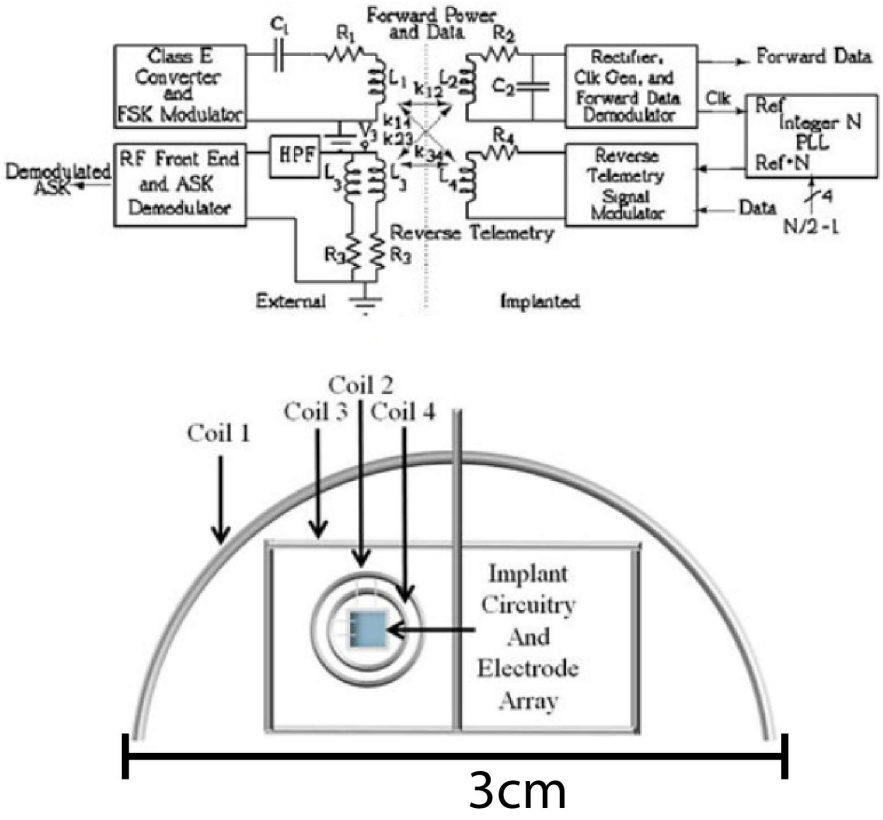

Figure 2-9: Block diagram of Near-field powering and communications using separate data and power frequencies, including separate coils for each frequency [RUSH]

2.2 Effect of Phase Noise on Receiver Sensitivity

Even if the amplifiers in the receive chain could remain in a linear mode of operation in the presence large self-jammers from the TX, the phase noise of the TX carrier leakage could still desensitize the receiver. Phase noise is the result of non-idealities in the oscillator that generates the carrier. The amplitude noise in the components of a VCO manifests itself as random perturbations in the phase of the generated carrier. An example white phase noise power spectral density of a carrier signal vs frequency offset is shown in Fig 9. This noise is particularly dangerous in an RFID reader because the self-jammer leakage is large compared to the received signal. Fig. 2-10 also shows how the phase noise from transmit PA can leak into the receive path. Assuming white phase noise, we calculate the effect of the phase noise at the carrier P_{noise} using

$$P_{noise} = P_{TX} \times G_{circ} \times P_{PN} \times BW_{sig} \quad (5)$$

here P_{TX} is the transmitted power of the PA, G_{circ} is the isolation of the circulator, P_{PN} is the phase noise in dBc/Hz of the carrier, and BW_{sig} is the bandwidth of the received signal.

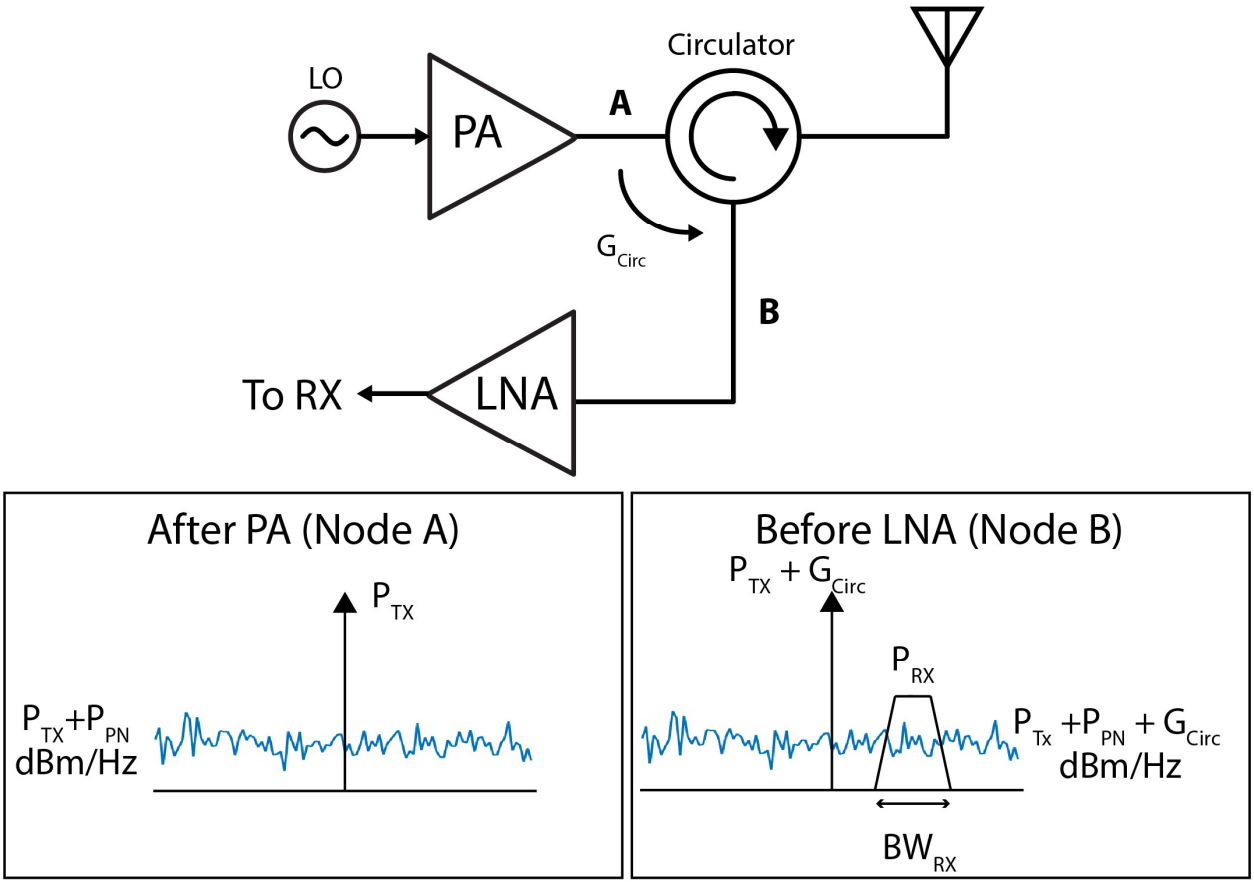

Figure 2-10: Effect of phase noise on RFID Reader using circulator.

Several observations can be made by the expressions above. Higher isolation of the circulator G_{circ} results in a lower amount of phase noise at the PA output. In addition, a higher RX signal

bandwidth results in a greater integrated noise in the band of interest. This suggests that for RFID systems where there is a high loss between tag and load, bandwidth-efficient modulation schemes can result in improved receiver sensitivity.

What if there are multiple sources of interference caused by transmit leakage? It is clear that the combined signal strength of the combined interferer would depend on the relative phase and magnitude difference between the two sources. However, the way the noise from the two sources add up depends on the correlation between their respective noise. Noise power in a signal can be modeled as the variance of a random process. If two noise sources are completely uncorrelated, the variance of the noise adds in the power domain. The resulting noise source has a variance expressed by

$$\sigma_{sum}{}^2 = \sigma_1{}^2 + \sigma_2{}^2 \tag{6}$$

However, if the noise is correlated, the situation becomes more complex. If two sources of noise have the same spectral density, but are correlated the standard deviation of the noise can be expressed as

$$\sigma_{sum}{}^2 = \sigma_1{}^2 + \sigma_2{}^2 + \rho\sigma_1\sigma_2 \tag{7}$$

Where ρ is the correlation factor. This result has some interesting implications. It means that if $\rho > 0$, the noise is actually higher than the sum of two independent noise sources. It also means that if $\rho = -1$ and the standard deviation of each noise source is the same magnitude with the same spectral characteristic, the noise can perfectly cancel. This is the case shown in a cancellation loop with a single source of noise in the next section.

2.2.1 Phase Noise Experiment

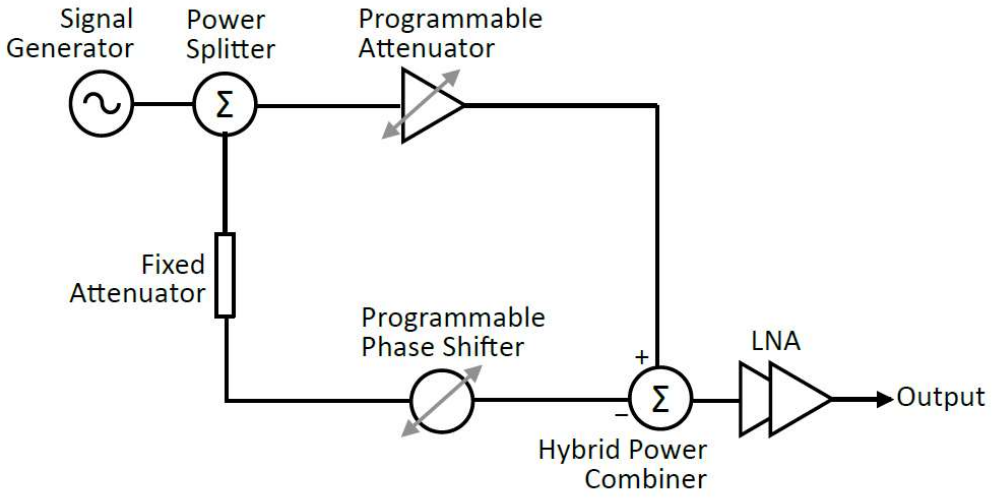

Figure 2-11: Phase noise cancellation experiment. [CHEN1]

To explore the behavior of different interference cancellation methods on the overall noise of the external reader a system, an experiment was devised. Fig. 2-11 shows a block diagram of the phase noise cancellation experiment. The signal generator is directly fed into a power splitter which splits the signal into two paths, each with their own different attenuators. One attenuator is programmable in order to compensate for any gain imbalance between the top and ottom path. In order to match the paths together a progammable phase shifter can be tuned anywhere from 0 to 1080 degrees was used to match the paths to each other. If one path is any integer multiple $n *$ 360 degrees phase shifted away from the other path, then the inteference should cancel, assuming equal magnitudes of the signal of both paths.

However, as shown in the simulation results of Fig. 2-12, the phase noise of the interference only cancels if there is a 0 degree phase alignment between the main signal and the cancellation path. Why is this? The phase noise from any integer multiple $n \times 360^{\circ}$ phase-shifted version of the signal generator is not corellated with the phase noise from the 0 degrees phase-shifted version of the signal generator. Only when phase noise is correlated can the sum of the paths' noise cancel out when subtracted form each other.

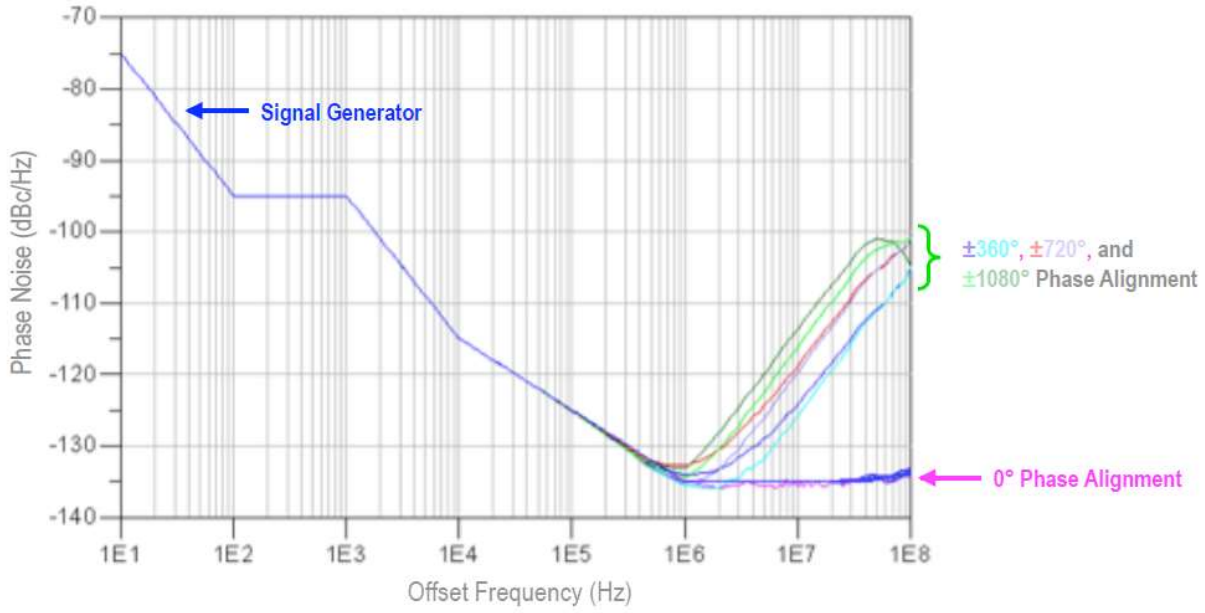

Figure 2-12: Phase noise from single path cancellation experiment [CHEN1]

2.3 Received Signal Strength

In an RFID reader system, the signal strength of the recovered backscatter signal P_{sig} can be expressed as

$$P_{sig} = P_{PA} \times {L_{channel}}^2 \times {G_{tag}}^2 \times L_{RX} \times d_M \quad (8)$$

where L_{RX} takes into account all the losses induced from the passives in the receiver. L_{Chann} is the propagation loss through the channel. G_{tag} is the antenna gain of the implant's antenna. And d_M is the modulation depth of the backscattered signal. It's important to note that the losses of the channel $L_{Channel}$ are suffered twice in this system.

From (8), it appears that there are several ways to increase the signal strength of the backscatter by the reader. Increasing the power output of the transmitter P_{PA} increases the receive signal, but it also increases the strength of the interference. The phase noise contributed by the self-jammer also increases by the same amount, so the SNR of the receiver is left unchanged.

Decreasing the loss of the channel and/or improving the gain of the tag results in a larger backscattered signal. Antenna optimization and correct choice of carrier frequency given the system size constraints can greatly improve link efficiency [MARK1].

Modulation depth d_M is a measure of the degree of reflection in a backscatter system. When the reader sends a power carrier to the tag, the tag can communication by switching its impedance so that it either absorbs the carrier or reflects the carrier. The contrast in signal amplitude between the two states is the modulation depth.

2.4 Design Example: External Reader for 1 mm^3 Neural Transponder

Sub-cranial implants should have as small of a form factor as possible to minimize damage to brain tissue. To push the limits of size and power for a wireless implant, a 1mm^3 330 fJ/bit transponder was designed in [MARK2]. This implant was designed to be wirelessly powered, and it communicates with the outside world using a transmitter with a unique form of backscattering called a reflective impulse radio. Because of the small size of the coil relative to the frequency of operation, there is a large loss through the channel in powering the radio. On the communications side, this loss is even more significant. Because the transponder communicates by reflecting the carrier from an external reader, the carrier that is modulated by the backscattered data suffers the channel loss twice. The primary challenge in designing the external reader for this implant is delivering power safely to the implant, while being sensitive enough to receive the implant's backscatter communications.

This section focuses primarily on the design of the external reader meant to power and communicate with the 1mm^3 neural implant described above. The first part of the chapter discusses the challenges with powering the implant. Next, the communications protocol of the implant is discussed. Based on the requirements of the implant, the design for reader using off-the-shelf RF components is discussed. Measurement results and system analysis results are then discussed to inform the design of future RFID readers meant for neural implants.

2.4.1 Transponder Specifications

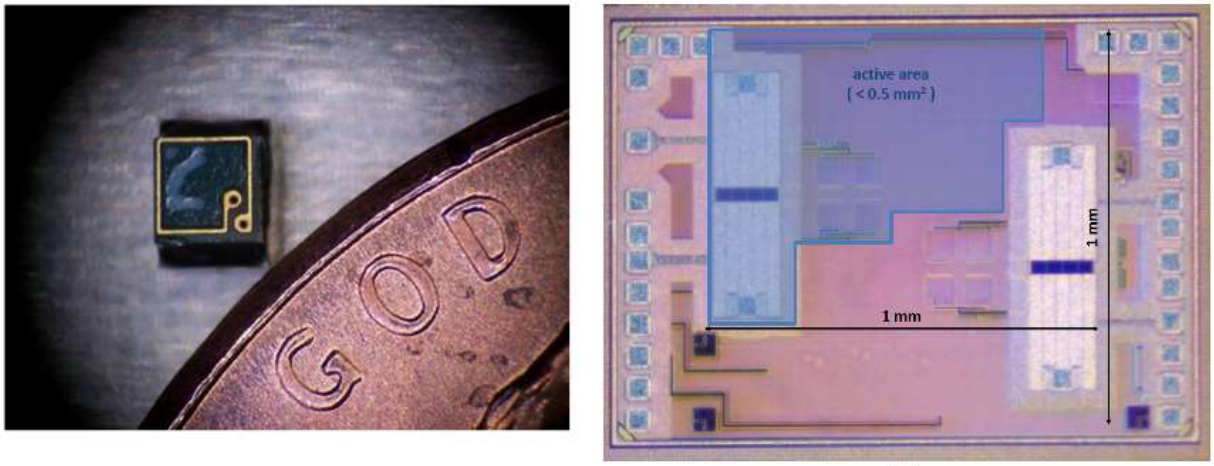

Figure 2-13: a.) Size comparison of implanted transponder micro PCB antenna and coin b.) Die photo of neural transponder testchip [MARK1]

Fig. 2-13 shows the chip and microPCB used for the implant. The loop antenna consists of two loops to increase the inductance, which in turn increases the Q of the antenna. The dimensions of the loop antenna are 1 mm x 1 mm and the trace thickness is somewhere between 1.3 -1.6 mils due to process variation. On one side of the implant, there is one turn of the antenna and two gold pads that are meant to be connected to a transponder chip using flip-chip bonding. The other side contains the other turn of the antenna.

The transponder chip is fully integrated on a 1.1 mm x 1.4 mm chip in a 65 nm CMOS process. However, the bond-wire pads are mainly for testing purposes, and the active area is less than 0.5 mm^2. As a result, a version of the chip meant for implantation should have no problem fitting on the 1 mm^3 micro PCB implant board. Figure 13 shows the block diagram of the system. An AC-to DC converter down-converts the signal from the antenna and stores it on a capacitor for use as a power source. The data uplink consists of using pulse position modulation (PPM) to efficiently implement backscatter by shorting the two ends of the antenna together. A summary of the transponder's performance is given in Table 2-1.

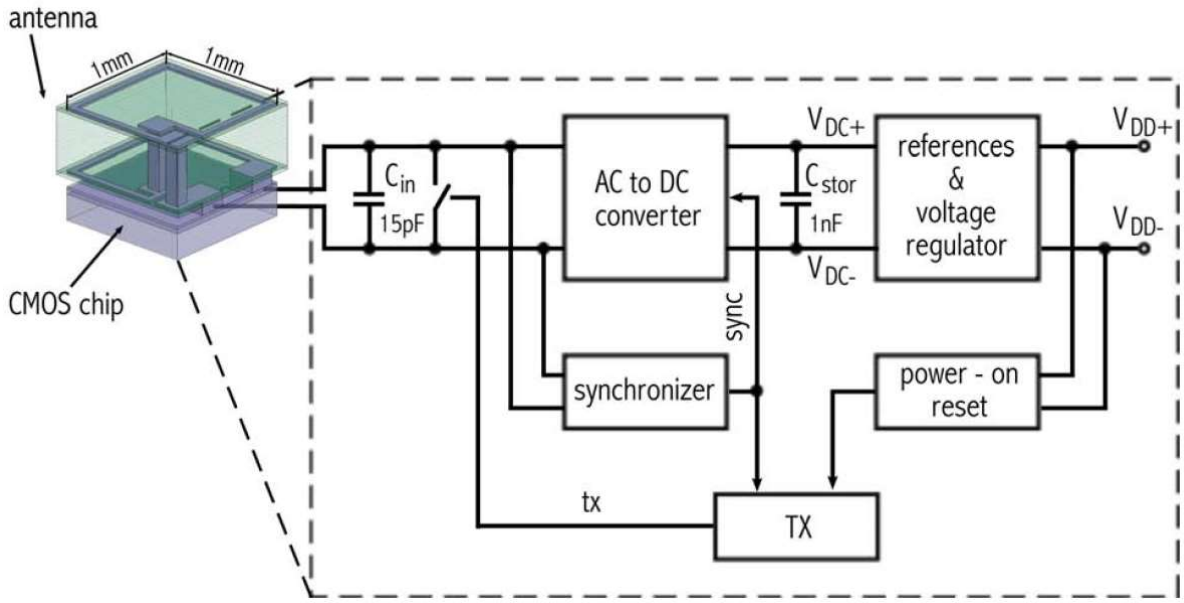

Figure 2-14: System Diagram of 1 mm^3 transponder [MARK1]

Table 2-1: Performance Specifications of 1 mm^3 transponder

Technology	65nm CMOS
Size	1.1 x 1.1mm
Power TX	660 nW
Data Rate	2 Mb/s
Energy/bit	330 fJ/bit
Extra Power Available	5 uW

2.4.2 Communications

The transponder communicates using a wireless communication architecture known as Reflective Impulse Radio (RIR). Conventional RFID Readers use narrowband modulation schemes such as Amplitude Shift Keying (ASK), Frequency Shift Keying (FSK), or Phase Shift Keying (PSK). Fig. 2-15 illustrates the principle of pulse position modulation (PPM) for a Reflective Impulse Radio. Each symbol period T_{PR}, the tag reflects the transmitted carrier from the reader for a time t_{PW} which is only $\frac{1}{M}$ of T_{PR}. In this transponder, sending a pulse requires shorting the antenna, which means that the implant cannot absorb power during the duration of the pulse. The RIR scheme allows the tag to fully absorb power from the reader's carrier for $\frac{M-1}{M}$ of each symbol period. In addition, each symbol period can transmit up to $\log_2 M$ bits of information.

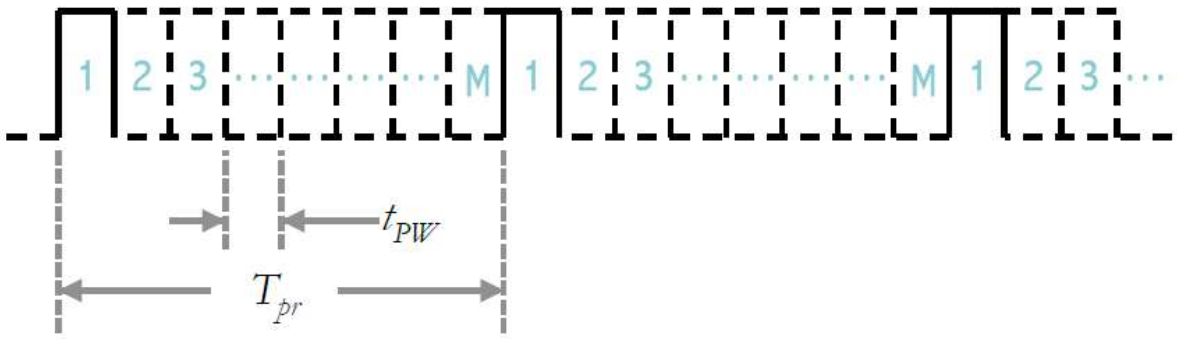

Figure 2-15: Pulse Position for Reflective Impulse Radio [CHEN1]

A block diagram for the transponder's reflective impulse transmitter is shown in Fig. 2-15. Pulses are fed into a PPM encoder consisting of an adujustable delay line that is set by the baseband data that the radio intends to send. This pulse is fed into buffers and then finally to a switch that shorts the antenna when the pulse is high. In this RIR radio, modulation depth d_M is limited to 50%.

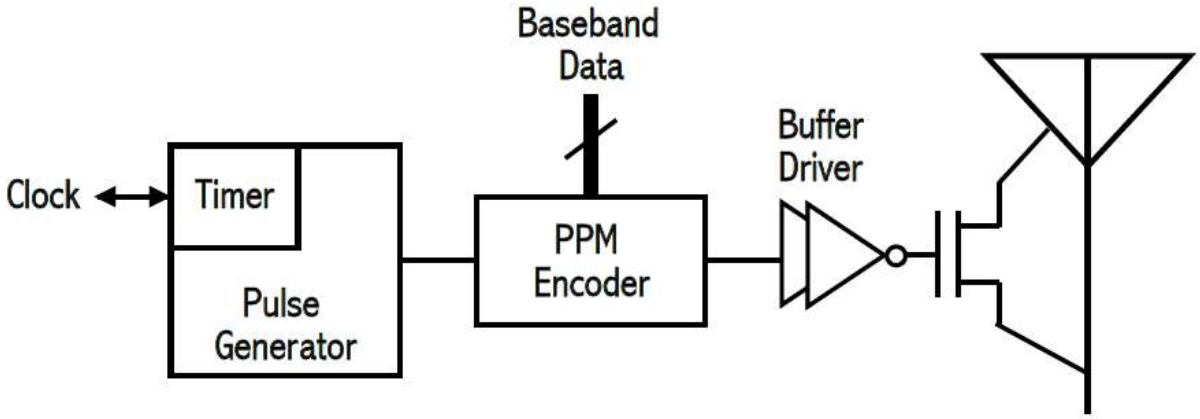

Figure 2-16: Diagram of Reflective Impulse Transmitter [CHEN1]

Why use a pulse position radio? There appears to be significant overhead in transforming the baseband data into a PPM encoder in order to create the pulses needed for backscattering. However, 3 bits of information can be transmitted for each symbol period T_{pr} as shown in Fig. 2-16. And to transmit these 3 bits of data requires only switching the antenna once per symbol period. This means that as the data rate of RIR goes up, its efficiency relative to simple on-off keying schemes will also go up. Fig. 2-17 illustrates this trade-off.

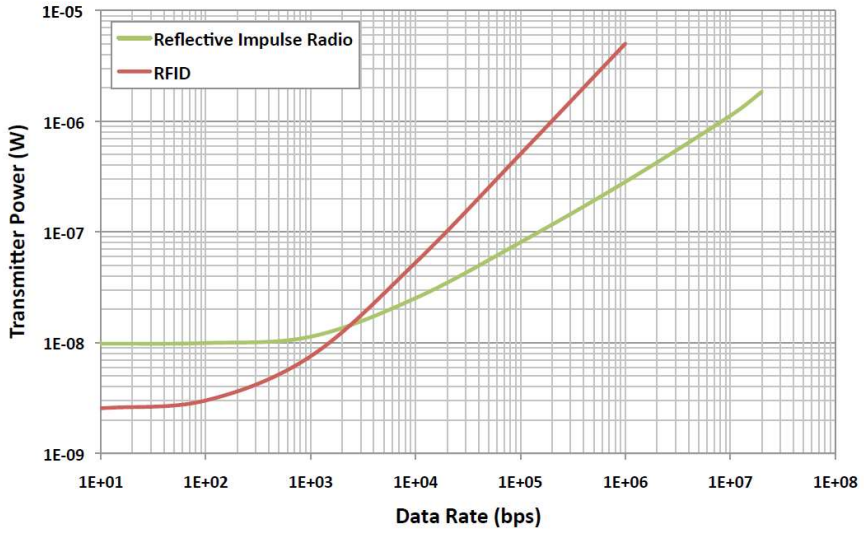

Figure 2-17: Power consumption of RFID and Reflective Impulse Radio vs. Data Rate [CHEN1]

The cost of this decreased power consumption by the implant is that the external reader needs to have a higher sensitivity in order recover the transponder's backscattered signal.

2.4.3 Reader Design

The reader design, built from off-the-shelf components, is shown in Fig. 2-18. A circulator is used to isolate the transmitted carrier from the received signal. However, because commercial circulators typically have isolations of < 25 dB, active cancellation also needs to be employed. The transmit PA is connected to a directional coupler that that sends a small portion of the PA output to an active cancellation path. The cancellation path contains an attenuator and phase shifter that is adjusted so that the path's output is equal in magnitude and phase to the carrier leakage in the receive path.

The primary limitation to this system is the leaked phase noise from the transmitter to the receiver. Shown in Fig. 2-19, even though the blocker can be fully cancelled by tuning the phase and magnitude of the shifter and attenuator, the noise is not cancelled. The phase noise is blocked in dBc/Hz. If the carrier leakage through the circulator were the only source of interference, the overall phase noise would be attenuated as the signal is attenuated, but the dBc/Hz level should remain unchanged.

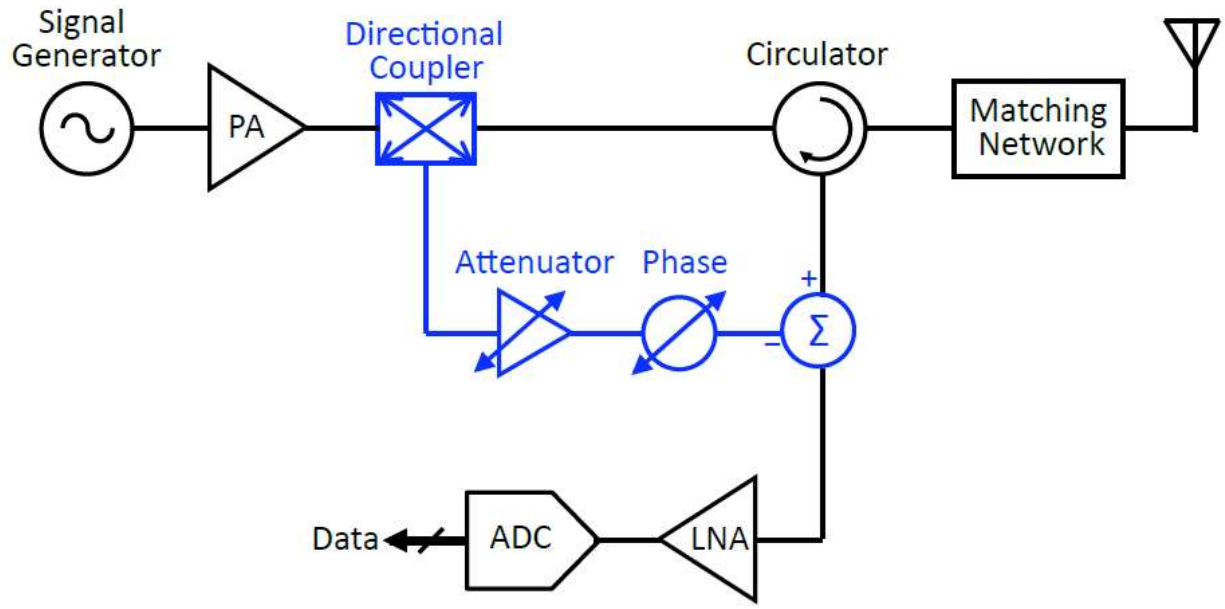

Figure 2-18: Diagram of Reflective Impulse Reader [CHEN1]

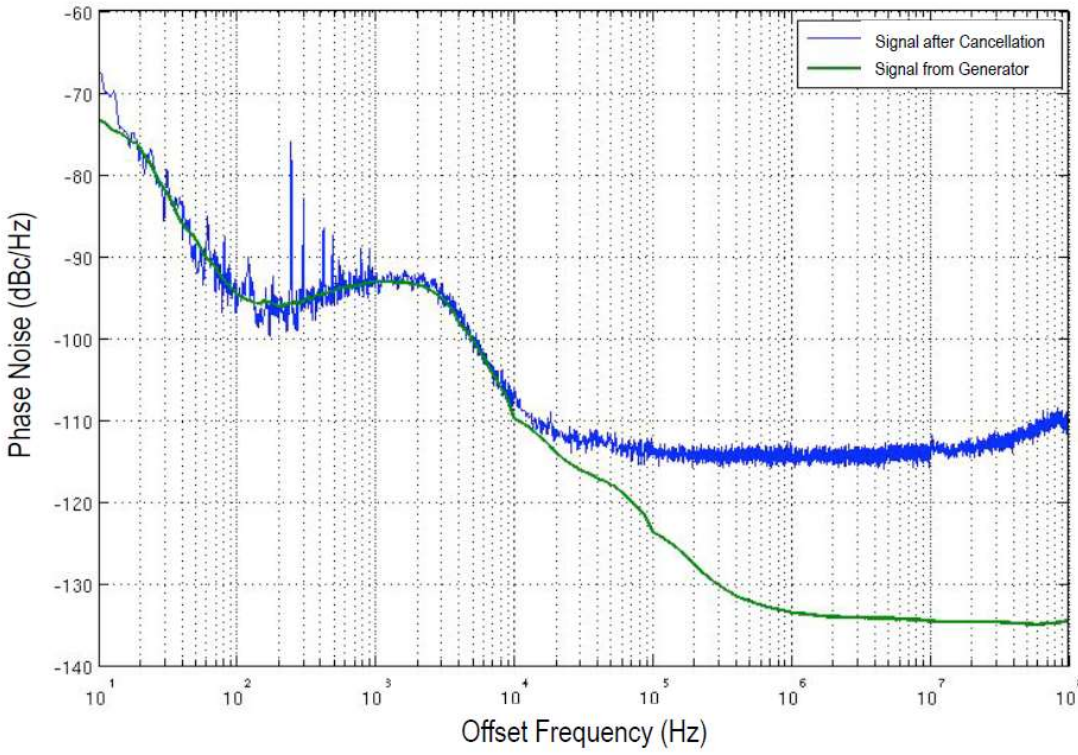

Figure 2-19: Phase noise from the generator and at the receive node. [CHEN1]

So why isn't the noise fully cancelled in this system? It turns out that there are two sources of interference in the reader design shown in Fig 17, the finite leakage of the circulator G_{Circ} and the return loss of the matching network RL_{MN}. It is impossible to guarantee that the phase shifts in the paths of the two sources of interference are identical, so the noise from each source cannot be fully correlated. In addition, the matching network is narrowband compared to the rest of the signal path and cancellation path. Therefore, its return loss would have a spectral characteristic that is different than the attenuated carrier used in the cancellation path.

2.4.4 Reader SNR

As shown earlier, the backscattered signal strength at the receiver can be given by

$$P_{sig} = P_{PA} \times {L_{channel}}^2 \times {G_{Imp}}^2 \times d_M \times L_{RX} \quad (9)$$

Calculating the SNR of the reader gives insight into the range of the reader. The first requirement of the reader is to calculate the noise. The noise incident at the input LNA can be expressed by

$$P_{noise} = P_{LNA} + P_{PN_{inteferer}} \quad (10)$$

where P_{LNA} is the integrated input-referred noise of the amplifiers of the receive chain, and $P_{PN\_inteferer}$ is the integrated phase noise of the interferer. Assuming that P_{LNA} is negligible because the LNA in this system is a highly sensitive off-the-shelf RF component, we are left

with $P_{PN\_inteferer}$. Calculating the RMS value of $P_{PN\_inteferer}$ requires integrating the phase noise spectral density over the bandwidth of the backscattered signal. Any out-of-band noise can be filtered out after the LNA. The backscatter reflective impulse radio has a spectrum that be shown in Fig. 2-20.

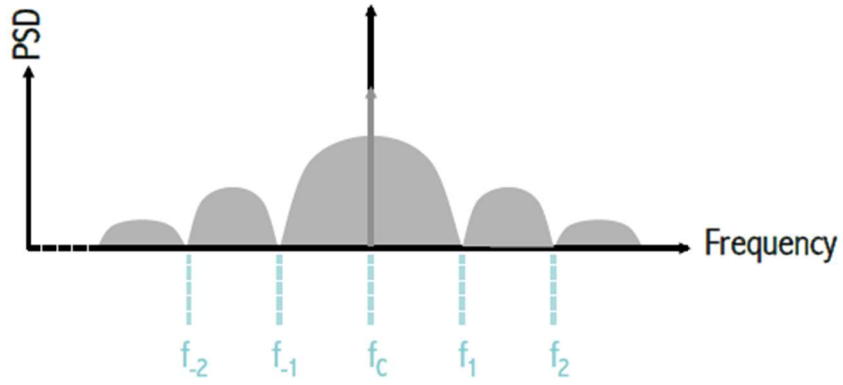

Figure 2-20: Power spectral density of reflective impulse radio [CHEN1]

For an impulse radio, the spectral content of the signal resembles that of a sinc ($sinc(x) = \sin(x)/x$) that is upconverted to RF and centered around the carrier frequency. As can be shown in Fig. 2-20, the majority of the energy in a pulse is between $f_{carrier} \pm \frac{1}{T_{pulse}}$, but there is still appreciable energy further away from the carrier. The phase noise can be given by

$$P_{PN,interferer} = P_{PA} \times G_{PNdBc} \times G_{isolation} \times BW_{sig} \quad (11)$$

Where P_{PA} is the transmitted power of the TX, G_{PNdBc} is the phase noise in dBc of the interferer, $G_{isolation}$ is the amount of interference cancellation of the reader, and BW_{sig} is the signal bandwidth. For simplicity, G_{PNdBc} is approximated to be white across the entire bandwidth of the signal. This will give slightly lower noise results than expected.

$$SNR = \frac{P_{sig}}{P_{PN,interferer}} = \frac{P_{PA} \times (L_{channel} \times G_{Imp})^2 \times d_M \times L_{RX}}{P_{PA} \times G_{isolation} \times G_{PNdBc} \times BW} = \frac{(L_{chann} \times G_{Imp})^2 \times d_M \times L_{RX}}{G_{isolation} G_{PNdBc} \times BW} \quad (12)$$

In the reflective impulse radio used in the transponder, for a symbol period of 1 us, the pulse width would be 0.125 us, contributing to a data rate of 3 Mb/s and a single-side band bandwidth of 8 MHz. An equation approximating the SNR given the simulated loss of the link ($L_{chann} \times G_{Imp}$) being -35 dB from [MARK1], and setting both the modulation depth d_M and receiver losses L_{RX} to 0.5 is given by

$$SNR = \frac{(L_{chann} \times G_{Imp})^2 \times d_M \times L_{RX}}{G_{isolation} G_{PNdBc} \times BW} = \frac{(10^{-3.5})^2 \times 0.5 \times .05}{10^{-4} * 10^{-11} \times 8 \times 10^6} = 3$$

Where the P_{PNdBc} is given by the measured results in Fig. 2-19, and $G_{isolation}$ is assumed to be -40 dB. Under the assumptions above, the radio is predicted to work, but not much margin is given to any source of non-idealities in the link.

2.5 Discussion

This chapter presented the classical problem of RFID Reader self-interference from its own transmitter potentially saturating its RX. Different methods of cancellation were explored, and each have their own pros and cons for use in a trans-cranial link for BMI. To test the feasibility of using backscatter communications to receive data from an implant, an external reader was designed for a 1 mm^3 neural transponder implant [MARK1]. The neural transponder pushes the limits for low power communications in an implantable system by using a novel form of backscattering based on PPM known as a Reflective Impulse Radio. Though consuming less than 1 uW on communication, the high communications bandwidth and high link loss of this tag make it challenging to design an external reader sensitive enough to demodulate its data in the presence of a large self-jammer. The external reader requires a bulky external circulator and an active cancellation loop to cancel the phase noise of the TX leakage over the entire bandwidth of the wideband RIR backscatter. It becomes clear that the reader and tag should be co-designed to consider the practical constraints of a wireless BMI system. In the next section, a wearable integrated RFID reader for a wireless uECoG neural implant is presented.

Chapter 3:

Integrated RFID Reader for Powering/Data Communications of Neural Implants

For BMI systems, a compact, efficient RFID reader architecture is desirable to deliver power to and communicate with mm-sized implants inside the skull. The reader should have an efficient power transmitter so that it can deliver sufficient power to the tag without needing too large of a battery to be worn on top of the head. As shown in chapter 2, to ensure proper operation, the RFID Reader must be able to isolate its receiver from its own transmitted self-interference in order to be able to recover the backscatter of the implanted tag. A lightweight form-factor is essential for comfortable wearing throughout the day.

This chapter will outline the design behind a single antenna RFID architecture using an ammeter-based data-recovery method to reject the interferer from an efficient TX using a Class E/Fodd switching PA. The first part of the chapter will introduce the Class E/Fodd Power Amplifier and introduce some unique properties about it that can be used to isolate a large transmitted carrier from a received backscatter signal in a near-field coupled link. Next, the received signal strength and link sensitivity of such a reader are derived based on link parameters and quality factor of PA passives. As a proof of concept, a design example of an integrated RFID Reader using these techniques is described. This reader is designed to deliver power to and receive data from an existing wireless ECoG Implant [MUL2] for applications of chronic neural recording for neurological diseases.

3.1 Target BMI System: 64-channel uECoG Neural Implant

An RFID reader meant for sub-cranial powering and communications should be designed to power and communicate with an actual neural implant. A minimally invasive 64-channel wireless Electro-corticography (ECoG) implant was designed by a colleague in [MUL2]. The device consists of a highly flexible polymer-based 64-channel electrode array and a flexible antenna, bonded to a CMOS integrated circuit that performs 64-channel signal acquisition from the surface of the cerebral cortex and wireless data transmission. The implant also derives its supply from external wireless power transfer. It requires 225 uW of power and transmits data at 1 Mb/s. The system requirements are specified in Table 3-1. The external RFID reader was designed to surpass

the maximum power delivery and received data rate requirements of the ECoG implant, shown in Fig. 3-1.

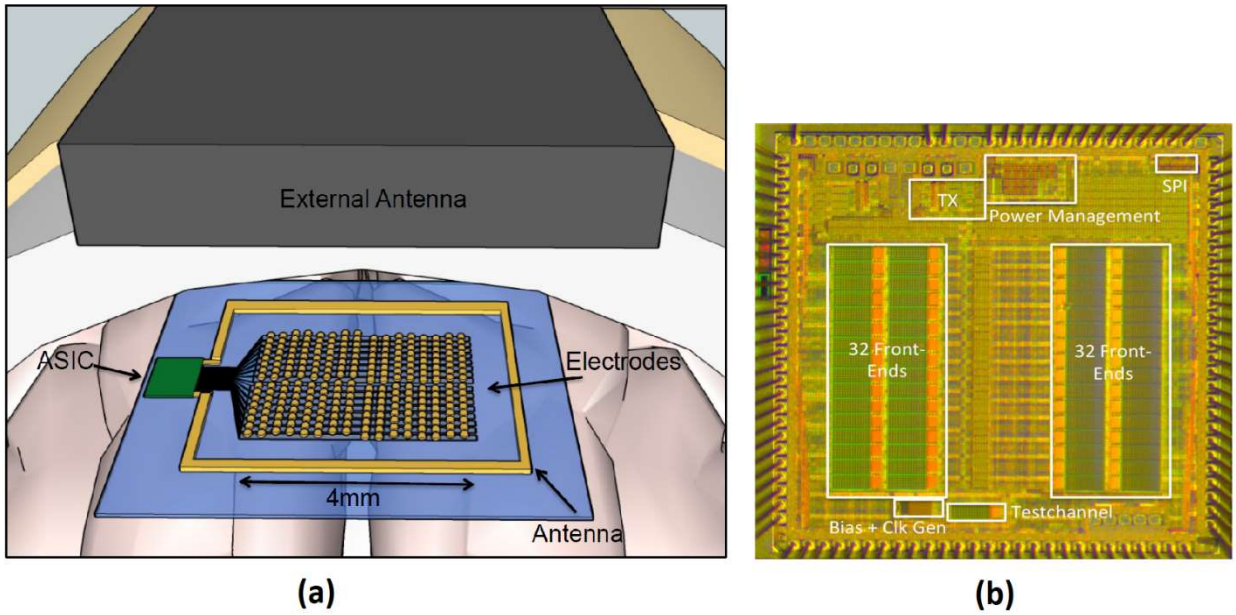

Figure 3-1: a) uECoG neural recording micro-system including electrodes fabricated on flexible substrate b) IC containing neural recording amplifiers, wireless power recovery, and wireless data communications. [MUL2]

Table 3-1
uECoG Implant Parameters

Recording Modality	Electrocorticography
Channel Bandwidth	1-500 Hz
Number of Channels	64 Simultaneous
Uplink Data Rate	1 Mb/s
Required Power at	225 uW
Carrier Frequency	~300 MHz
Implanted Antenna	6.5 mm

3.2 Ammeter-based Blocker Rejection using Nonlinear Switching Power Amplifiers

This section introduces an RFID reader architecture that doesn't need external isolators to cancel its own self-jammer by using the non-linear properties of switching power amplifiers to demodulate the backscattered signal to baseband, where it can be measured by an ammeter in series with the PA and the power supply. Interference is translated to DC, where it can be removed using

a DC blocking capacitor. Analysis based on the PA parasitics and link characteristics between the reader and the tag are used to determine the signal strength recovered at the ammeter.

3.2.1 Class E/Fodd Power Amplifier

The Class E/Fodd power amplifier, shown in Fig. 3-2 is a non-linear switching PA topology that was first introduced in [KEE]. It uses differential switches to drive a tuned differential load. Because the load is differentially driven, current at even harmonics does not flow through it. In addition, there is a parallel LC tank tuned to the fundamental frequency connected in parallel to the load to ensure that all higher-order harmonics are differentially shorted. The purpose of a tuned switching PA is to deliver power to a load at high efficiency. One of the primary mechanisms of loss in a switching PA is through the drain capacitance of the switches. As seen in Fig. 3-1, when a switch is turned on, the capacitance of each switch C_s is shorted to ground. As a result, each cycle, there is a loss equivalent to $C_s V_s^2$ through each switch in the PA. Tuned switching power amplifiers shape the waveform on the drain of the PA to resemble a half sinusoid so that when the switches turn on, the voltage across the switch is close to zero.

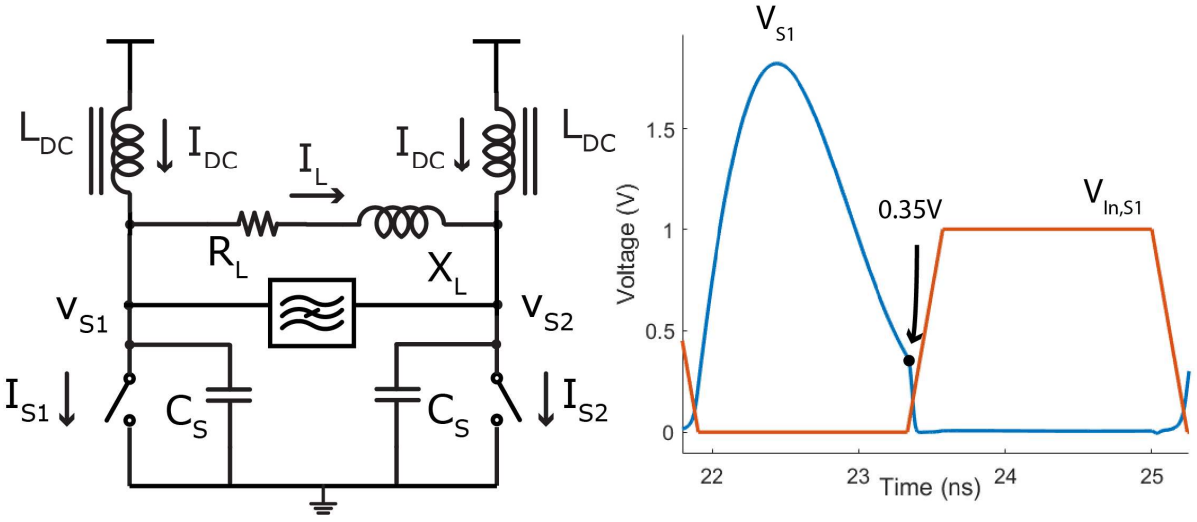

Figure 3-2: Class E/Fodd PA. High level schematic shown with drain waveforms.

3.2.2 Blocker Rejection Mechanism

As, seen in Fig. 1, one interesting property of the Class E/Fodd PA is that the current through each DC-choke inductor L_{DC} can be given by

$$I_{DC} = \frac{\pi^2 V_{DC}}{4R_L}. \quad (1)$$

This result reveals that the DC current the amplifier draws from the supply is dependent on only two parameters, the load resistance and the voltage of the power supply [KEE]. Fig 2 shows that the load impedance connected to the implant coil is near-field coupled to the external reader's

segmented antenna. As a result, any change to the load impedance of the implant changes the load impedance seen by the PA. If a series resistor is inserted in series between the power supply and the Class E/Fodd PA, then it can act as an ammeter that measures the change in current as the load impedance of the implant changes. The recovered baseband signal V_{Signal} across the ammeter resistor R_{amm} is given by

$$V_{Signal} = R_{amm} * \Delta I_{amm} \quad (2)$$

where ΔI_{amm} ($I_{amm} = 2I_{DC}$) depends on both the modulation depth of the implant tag and the coupling between the coils of the reader and implant.

Because the DC-feed inductor is not ideal, some leakage current at the TX carrier frequency will flow through the ammeter resistance, but the desired backscatter signal from the implant is already spectrally separated from the interference, so low order baseband filters can filter out any interference.

3.2.3 Effect of Link on Antenna Impedance

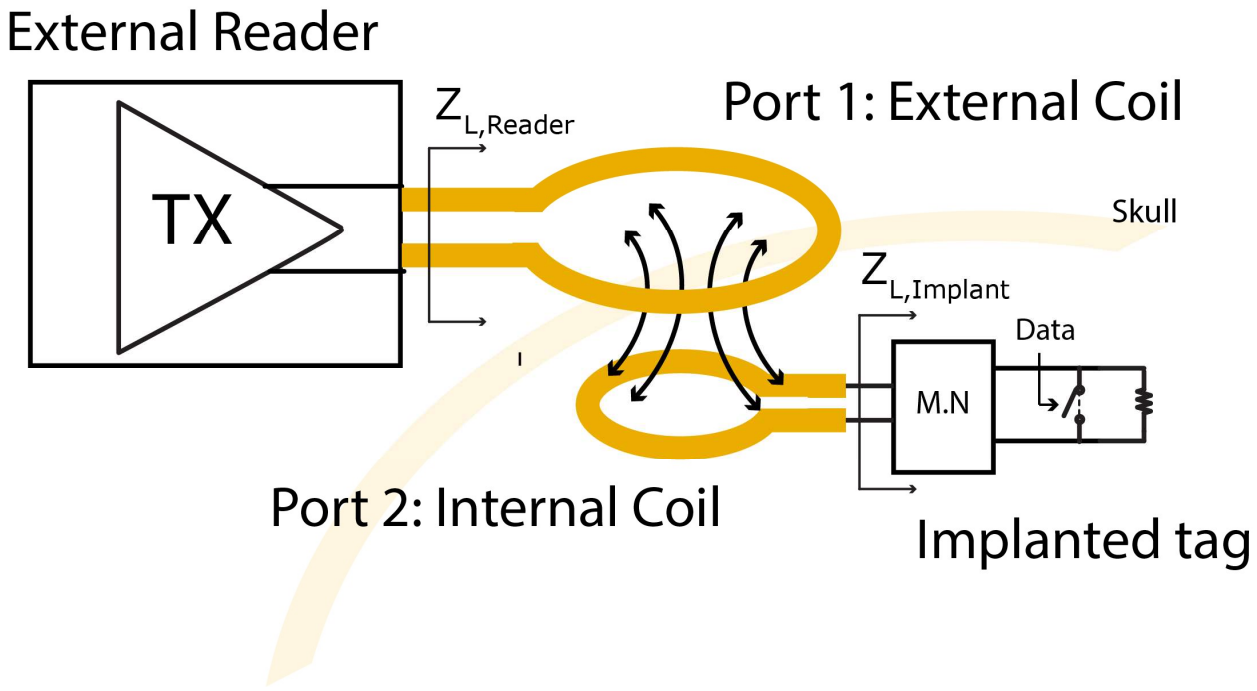

Figure 3-3: Diagram of power transfer in BMI Sytstem

In a wireless Brain Machine Interface system, power is coupled through an external loop RFID reader to an internal loop connected to the load of the implant. Because both loops are passive structures, the overall link parameters can be modeled through 2-port z-parameters, where port 1 represents the loop driven by reader, and port 2 represents the internal loop of the tag [ORF]. The impedance looking into the external loop is given by

$$Z_{L,Reader} = Z_{11} - \frac{Z_{12}Z_{21}}{Z_{22} + Z_{L,Implant}} \tag{3}$$

The desired recovered signal is based on the impedance $\Delta Z_{L,Reader}$ when the implant's load impedance $Z_{L,Imp}$ changes as follows

$$\Delta Z_{L,Reader} = \frac{Z_{12}Z_{21}}{Z_{22} + Z_{L,Imp}} - \frac{Z_{12}Z_{21}}{Z_{22} + (Z_{L,Imp} - \Delta Z_{L,Imp})}. \tag{4}$$

where port 1 refers to the terminals of the reader antenna and port 2 refers to the terminals of the implant antenna. $\Delta Z_{L,Implant}$ is the change in the load impedance of the implant impedance during backscatter communications. The change in the real impedance of the reader antenna is then given by

$$\Delta R_{L,Reader} = real(\Delta Z_{L,Reader}) \tag{5}$$

which results in

$$\Delta I_{amm} = \frac{\pi^2 V_{DC}}{2(R_{L,reader} - \Delta R_{L,Reader})} - \frac{\pi^2 V_{DC}}{2R_{L,Reader}}. \tag{6}$$

3.2.4 Effect of PA Efficiency on Backscatter Recovery.

The calculations above assume a 100% switching power amplifier efficiency. In reality, switching power amplifiers have significant loss that can affect the load impedance seen by the reader. ,

$$\Delta I_{amm} = \frac{\pi^2 V_{DC}}{2(R_{Total} - \Delta R_{Total})} - \frac{\pi^2 V_{DC}}{2R_{Total}}. \tag{7}$$

Fig. 3-3 highlights the factors which determine the strength of the recovered signal ΔI_{amm}. To maximize the detected signal ΔI_{amm} by the ammeter, the change in the total impedance seen by the outputs of the PA ΔR_{Total} must be maximized. R_{Total}

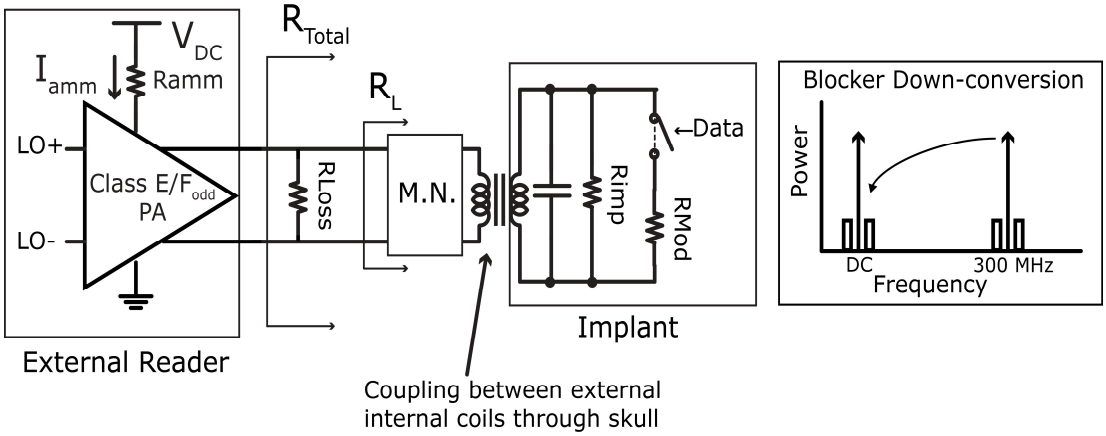

Figure 3-4: Backscatter demodulation mechanism

can be approximated by the parallel combination of the load resistance of the antenna R_L and the equivalent parallel loss resistance R_{Loss}. As shown in (4), the antenna resistance R_L changes by ΔR_L based on the modulation depth of the implant, the coupling factor between reader and implant coils, and the impedance of the implant. In a zero-voltage switching PA with relatively low switch on-resistance, R_{Loss} is dominated by the equivalent parallel resistance of the inductor L_{Tank} of the parallel LC tank of the Class E/Fodd PA. Calculation of ΔR_{Total} is as follows:

$$\Delta R_{Total} = \frac{(R_L + \Delta R_L)R_{Loss}}{(R_L + \Delta R_L) + R_{Loss}} - \frac{R_L R_{Loss}}{R_L + R_{Loss}} \tag{8}$$

$$\Delta R_{Total} \approx \frac{\Delta R_L R_{Loss}}{R_L + R_{Loss}}. \tag{9}$$

This result shows that making the equivalent parallel resistance R_{Loss} as large as possible maximizes the detected signal on the ammeter. The method of achieving this high R_{Loss} would be to maximize the Q of LC tank inductor L_{Par} .

3.2.5 Why Class E/Fodd?

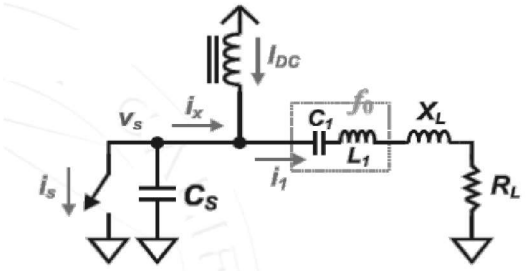

Class-E PA schematic

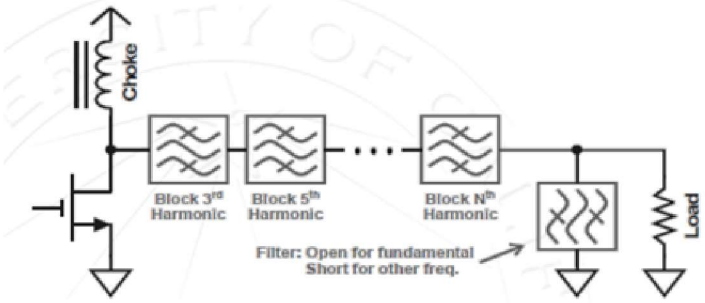

Class-F PA conceptual implementation

Figure 3-5: Schematic Diagrams for both Class E and Class F PA

Class E PA and Class F PA have single-ended topologies. In a CMOS process, the MOS switches can tolerate only a finite amount of voltage before device breakdown. Switches constructed from multiple cascode devices placed in series can limit this effect, but can increase the series resistance

of the PA switches. Assuming a sinusoidal output, he maximum amount of RMS power able to be delivered to the load of a single-ended PA can be expressed by

$$P_{Lmax,SE} = \frac{{V_{max}}^2}{8R_L} \tag{10}$$

Where V_{max} represents the maximum swing on the switch of a single-ended PA. In a differential Class E/Fodd PA, R_L is a differential load placed in between the positive and negative outputs of the PA. Because only one side of the PA is on at a time, V_{max} is now the amplitude of the sine wave across the load resistance of the PA. The power delivered to the differential load can be given by

$$P_{Lmax,DE} = \frac{{V_{max}}^2}{2R_L} \tag{11}$$

As seen by combining (10) and (11), it is apparent that $P_{Lmax,DE} = 4P_{Lmax,SE}$. In modern CMOS processes, this breakdown voltage is on the order of 1V, so being able to transmit power with lower voltages enables easier integration with digital CMOS processes.

In addition, the Class F PA consists of multiple parallel LC band-reject filters in series with its output switch and output load. In modern CMOS processes, passives such as inductors are lossy, so each of these LC filters would induce a significant amount of loss in the transmitter [KEE].

3.2.6 Choice of Ramm

According to (2), having a higher R_{amm} results in a higher received signal at the ammeter for the same I_{amm} . However, increasing R_{amm}results in a larger voltage drop so that the effective V_{DC} seen by the PA is lowered by $I_{amm}R_{amm}$ (assuming $I_{amm} \gg \Delta I_{amm}$) so that

$$\Delta I_{amm} = \frac{2\pi(V_{DD} - I_{amm}R_{amm})^2}{R_{Total} - \Delta R_{Total}} \tag{12}$$

Because excess power is burned in the ammeter that does not make it to the load of the PA, As R_{amm} approaches the load impedance of the PA, it actually takes a larger amount of power in the transmitter to receive the same increase in signal strength. Fig. 3-6 shows the simulated ΔI_{amm} vs. different values of R_{amm} for different values of load resistance to the PA. Also shown in Fig. 3-6 is the effect on PA efficiency vs R_{amm} for differing values of R_L. An R_{amm} is small relative to R_L, there is minimal impact on PA efficiency. An R_{amm} value of 1 ohm was chosen so that it would only be 2% of the value of a PA load resistance R_L of 50 ohms.

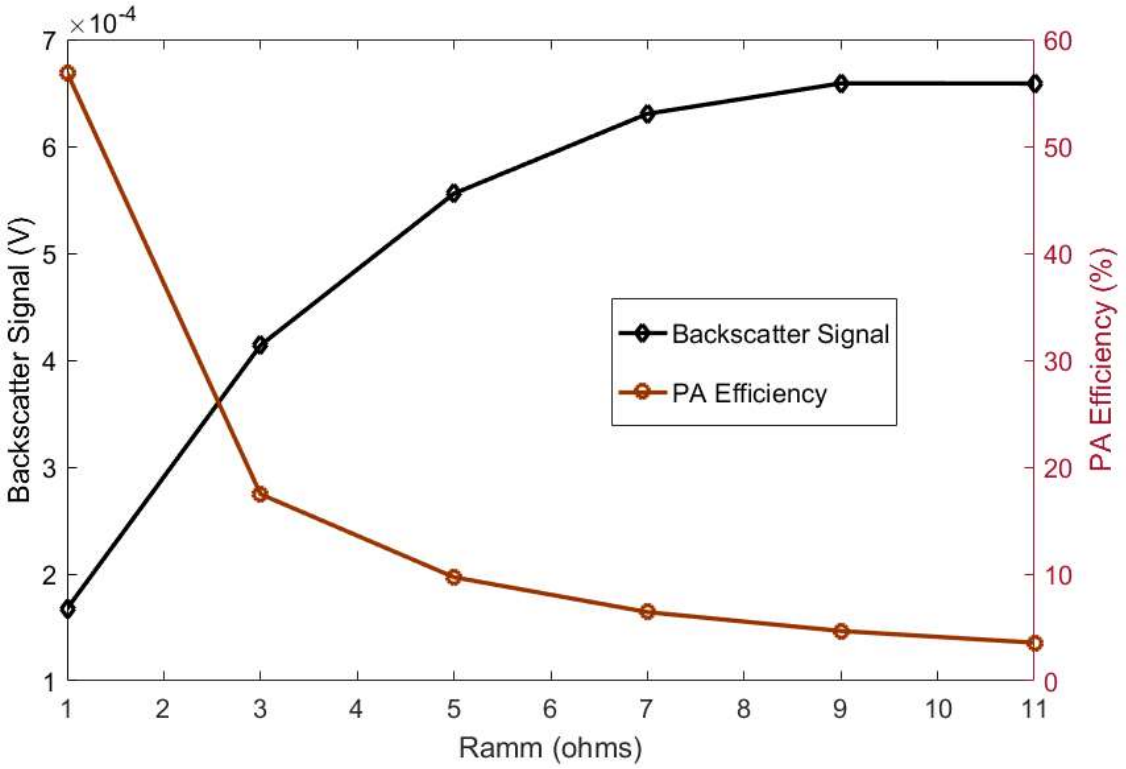

Figure 3-6: Backscatter Signal and PA Efficiency vs Ammeter Resistance.

3.3 System Architecture

Fig. 3-7 shows the system diagram of the proposed RFID reader. The transceiver is intended to deliver power to and receive data from the implant in [9]. The transmitter consists of a Class E/Fodd Power amplifier [8] driving a segmented loop antenna at 309 MHz. An ammeter resistor measures the current drawn from the power supply of the PA. Because the reader and the tag are near-field coupled, the tag's impedance modulation will affect the load impedance seen by the PA of the reader, and hence the DC current drawn from the supply by the PA, which depends directly on its load. The non-linearity of the switching PA effectively mixes the backscatter of the tag down to DC, and spectrally separates the desired backscatter signal from the PA's output without the need for any external circulator or isolator. Any leakage current at RF can be filtered with simple low-pass filters built into the baseband amplifier chain (see Fig. 3-7), while any DC offset is filtered with a DC blocking capacitor. The data is encoded using Miller modulation, moving information away from DC, so the DC blocking capacitor does not introduce any loss to the desired signal.

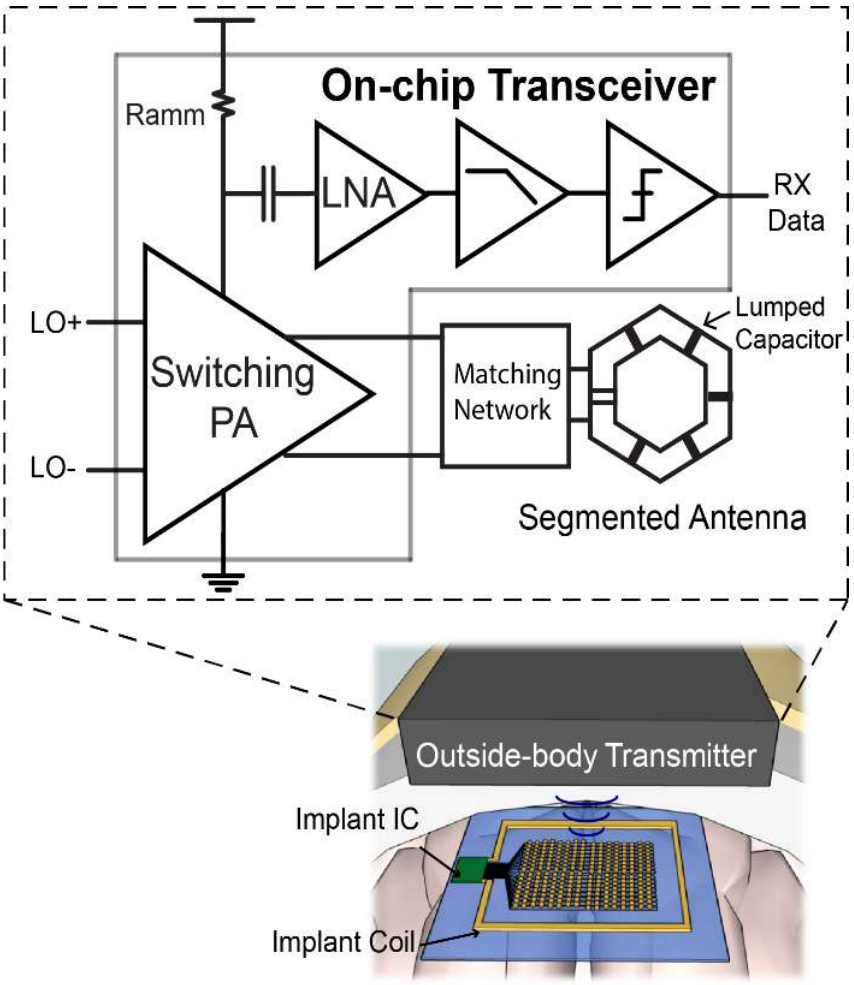

Figure 3-7: Trans-cranial Link Diagram and Transceiver Architecture.

3.4 Integrated Circuit

The integrated circuit consists of both transmit and receive circuitry. The transmitter consists of a Class E/Fodd power amplifier that is driven by a buffer chain. The receiver consists of a single-ended baseband LNA and subsequent baseband amplification and filtering stages. Having a high-efficiency PA also improves the signal strength of the recovered backscatter signal. As shown in (8), if most of the PA power consumption is delivered to the load antenna instead being burned in the PA, then the change in the PA's load impedance by backscattering will result in a larger change in the current drawn from the supply.

3.4.1 Transmitter Design

The TX power amplifier is designed using a modified Class-E/Fodd topology. The two separate large DC choke inductors and the inductor of the parallel LC tank are replaced by a single symmetric inductor that has a center tap connected to the supply. This modified design saves area on the chip while allowing a higher-Q inductor to be used for both the LC tank and the DC feed inductors.

3.4.1.1 Symmetric Inductor

In addition to having a high enough Q to minimize losses through the LC tank, the equivalent parallel resistance of this inductor must be sufficiently large compared to the load impedance of the PA so that the majority of the current from the PA flows into its load. As a result, the inductance had to be designed to be as large as possible given the area constraints of the chip. To increase the inductance, the symmetric inductor was designed to have 9 turns. Even with 9 turns, the self-resonant frequency (SRF) of the inductor is still 1.2 GHz, far higher than the 300 MHz operating frequency of the PA. The Class E/Fodd PA requires that the impedance in parallel with the load inductor is a short at frequencies higher than 300 MHz, so a 1.2 GHz SRF should not affect PA performance.

3.4.1.2 PA Impedance at Harmonics

Class E/Fodd operation requires there to be a high impedance from the output nodes of the PA to the power supply. Fig. 3-8 shows that the voltage at the drains of Class E/Fodd PA's have both differential and common-mode components. To ensure that the PA remains in Class E/Fodd operation, the impedance seen from output to supply must be large compared to the load being driven. Using separate DC choke inductors for each side of the PA accomplishes the goal of high impedance at both common mode and differential mode components of the PA output to the DC supply. However, this TX design combines the parallel LC-tank inductor and the two DC feed inductors of a classic Class E/Fodd PA into one large center-tapped symmetric inductor to save area and reduce the number of external components.

Figure 3-8: Differential and Common-mode components of Class E/Fodd Waveforms.

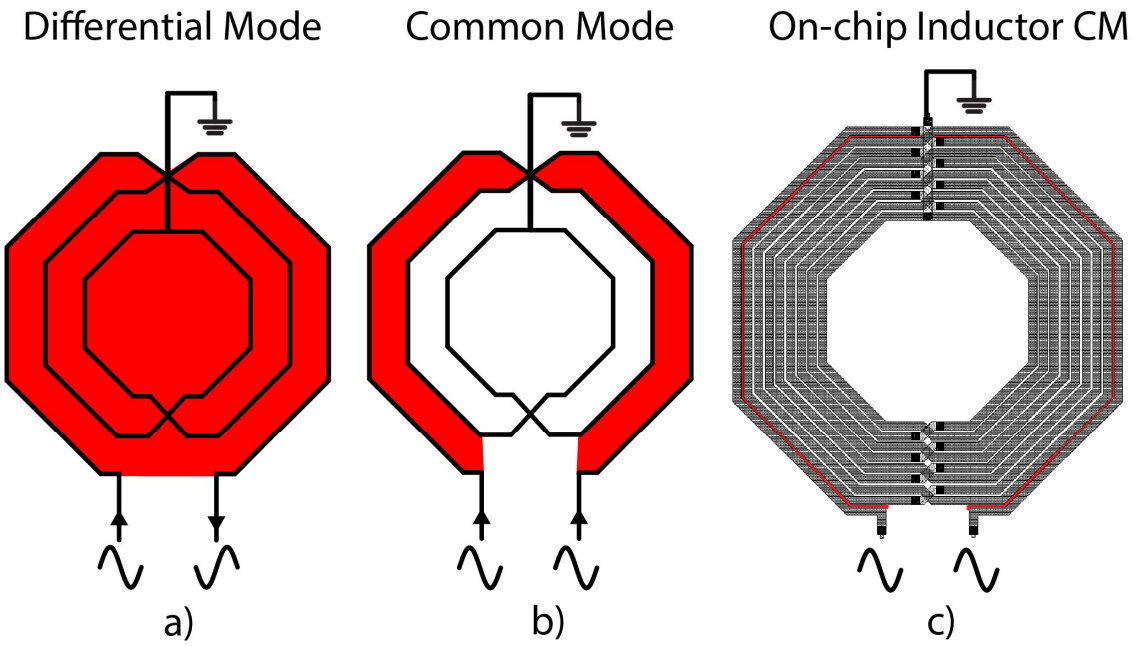

Figure 3-9: Magnetic field, shown in red, generated by a) 3-turn symmetric inductor operating in differential mode, b) 3-turn symmetric inductor operating in common mode, and c) the on-chip 9-turn symmetric inductor operating in common mode.

Even though the symmetric inductor has a high differential inductance, the common mode inductance is low because there are 9 turns that are closely wound together [CHEN2]. The path from the positive terminal of the inductor to the center tap is wound in the opposite direction as

the path from the negative terminal of the inductor to the center tap. Fig. 3-9 illustrates the difference in magnetic field induced in between common mode and differential operation of a center-tapped symmetric inductor. In common-mode operation, this results in most of the flux generated by one side of the inductor to be almost equal in magnitude but opposite in direction to the flux generated by the other side of the inductor, creating a low inductance path of less than 1 nH from the common mode of the PA to the supply. This low inductance causes there to be an especially small impedance from the output to the supply at the 2nd harmonic.

To solve this issue, an extra inductor L_{DC} is put in between the center tap of the inductor to increase the common mode inductance without changing the differential inductance of the PA. Without capacitors added in parallel, the common-mode impedance of the inductor tap to the supply at even harmonics is

$$X_{DC} = \omega\left(L_{Par,CM} + L_{DC}\right). \tag{13}$$

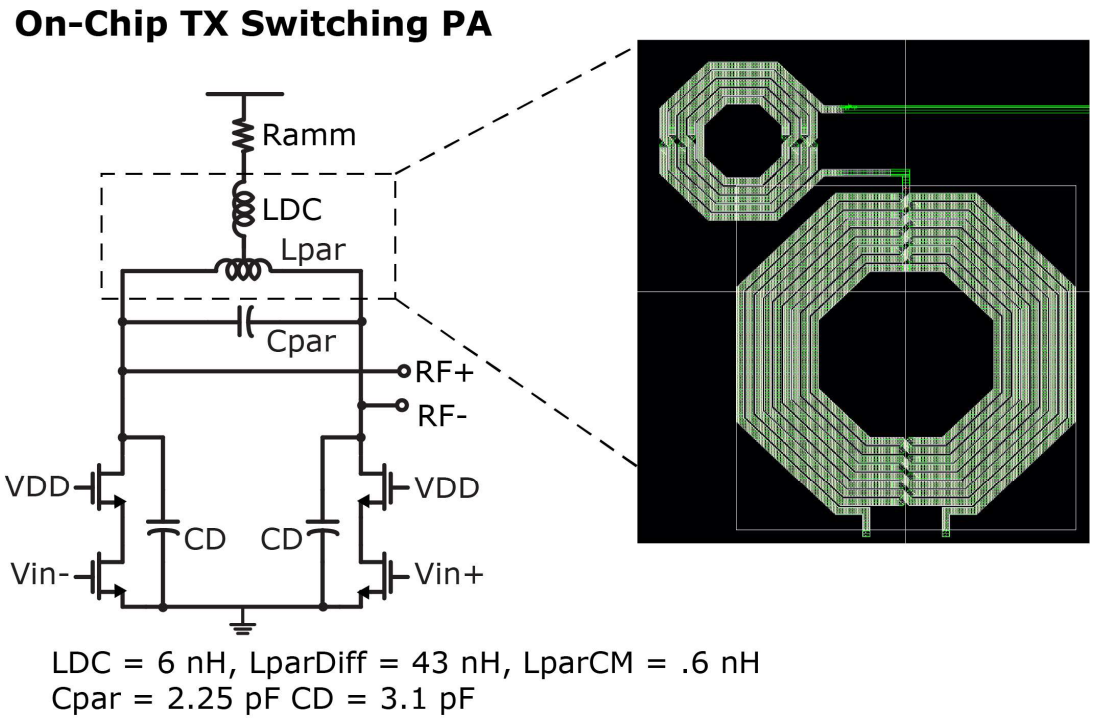

Figure 3-10: Final design of on-chip TX PA

the output switches of the PA to resonate with this increased common inductance at the 2nd harmonic of the transmitted carrier. The final design for the modified Class E/Fodd is shown in Fig. 3-10. The expression for the resonant frequencies ω_{Diff} for the differential load of the PA is

$$\omega_{Diff} = \frac{1}{\sqrt{L_{par,Diff} * (C_{par} + C_{DC} + C_{D,switc})}}. \tag{14}$$

And the expression for the second harmonic resonance frequency ω_{CM} for the common mode impedance of the PA is

$$\omega_{CM} = \frac{1}{\sqrt{(L_{par,CM} + L_{DC}) * (C_{DC} + C_{D,switc})}}. \quad (15)$$

3.4.1.3 Switch Design

The differential switches of the PA were designed with a cascode topology to increase the maximum voltage allowed at each output node of the PA before device breakdown. The primary causes of loss for PA switches are the $CV_{DD}{}^2$ loss of the stages driving the PA output stage and the loss from the finite series resistance of the switches themselves. The transistors were sized to balance both sources of loss.

3.4.2 Receiver Design

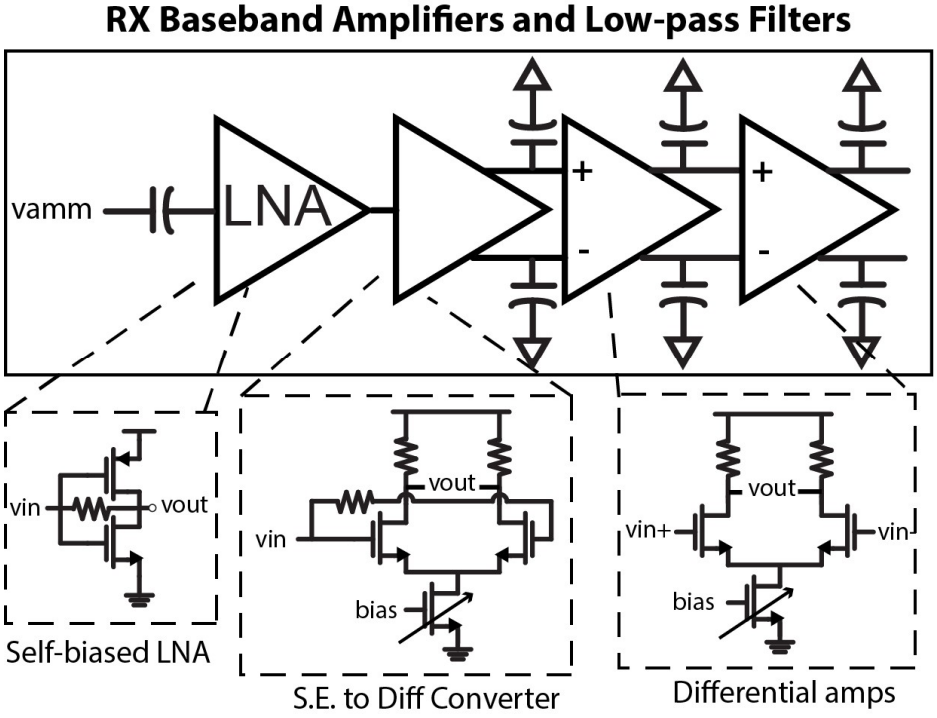

Figure 3-11: RX Baseband Implementaton

To recover the backscattered signal from the implant, the receive chain is connected to a 1 ohm ammeter resistor that is connected in series with the power supply of the transmitter. The received signal from the implant is miller encoded to ensure there is no frequency content at DC. This encoding allows the receiver of the reader to filter out any DC offset from the backscattered signal using a 30 pF series blocking capacitor. The baseband amplification stages are shown in Fig. 3-11. The LNA is followed by a differential pair acting as a single-ended to differential converter and amplifier. This stage drive two subsequent stages of differential pairs to create a total gain of 60 dB for the receive chain of the reader.

3.4.2.1 Miller Encoding

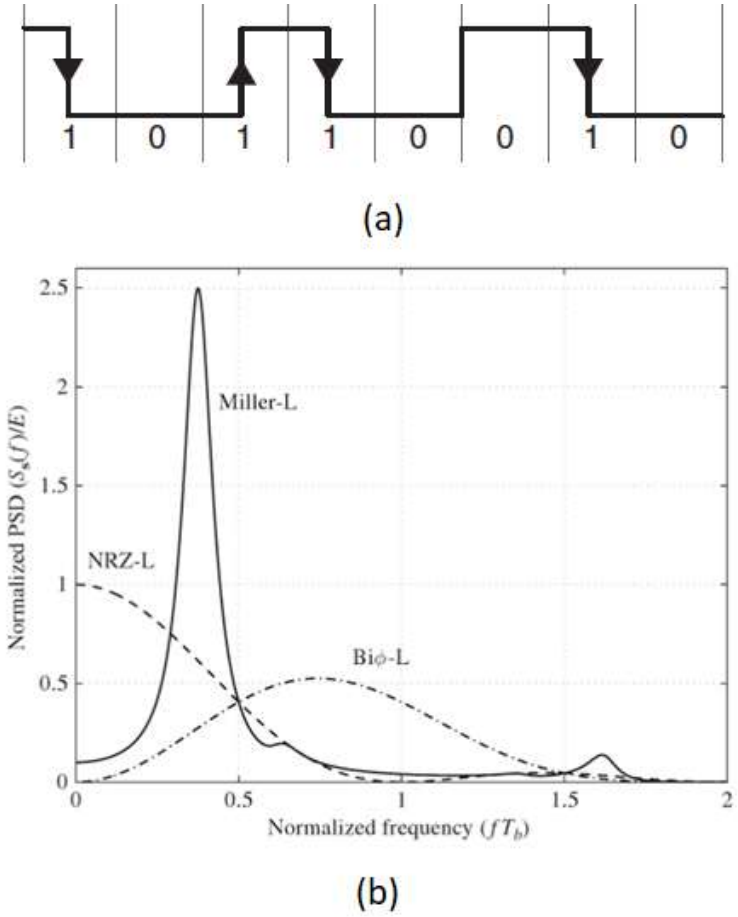

Figure 3-12: a.) Example of miller encoded data [FIN] and b.) normalized power spectral density of miller-modulated data. [NGY]

The ECoG implant uses Miller encoding to communicate with the reader in order to make it easier to filter the interfering carrier away from the received backscatter. Miller encoding is a way to code data so that a transition always happens every 2-4 cycles depending on the data pattern being generated. Each symbol period contains two clock cycles. If a "1" is being transmitted, there will be a transition in the middle of the symbol period. If a "0" is being transmitted, there will be a transition at the end if the next symbol being transmitted is also a "0." Otherwise there is no transation.These frequent transitions ensure that there is very little information at DC. Fig. 3-12 shows a sample data pattern and the power spectral density of a Miller encoded system. Because the ammeter-based RFID reader directly down-converts the received signal to be centered at DC, any interference present from the carrier will also be down-converted to DC. Encoding the data using Miller modulation ensures that a simple first-order high pass filter can be used to cancel out any DC offset.

3.4.2.2 DC Offset Cancellation

In conventional RFID systems, the down-converted signal has a DC-offset component that varies based on the phase shift of the self-jammer component relative to the LO signal. Deterministic changes in the self-jammer (i.e. channel variations) usually happen at a slow rate (ms time scale). Considering that the backscatter data received is using miller modulation at 2 Mb/s, there is little information at DC, so a simple high-pass filter using a single capacitor as an AC coupler between the ammeter and LNA is effective in cancelling any DC offset.

One problem with using a simple high-pass filter for conventional RFID systems is that there can be long transients to charge the DC blocking capacitor if it is charged to an incorrect initial condition. However, this is mainly a problem in applications when tags are sporadically interrogated by a reader for only short period of time, such as RFID readers for inventory identification purposes [BOA]. In a BMI system, the tag would be an implant that would constantly be wirelessly sending neural uplink data, so a short period of charging the DC blocking capacitor at system start-up would have minimal effect on the overall functionality of the system, since the reader for the neural uplink would need to be on for minutes to hours at a time for most BMI applications such as neural prosthetics or chronic neural recording for seizure localization [MUL1]. Using a simple 1st order high pass filter for DC offset cancellation makes the reader design simpler without affecting the functionality.

3.4.2.3 Baseband Amplification and Filtering:

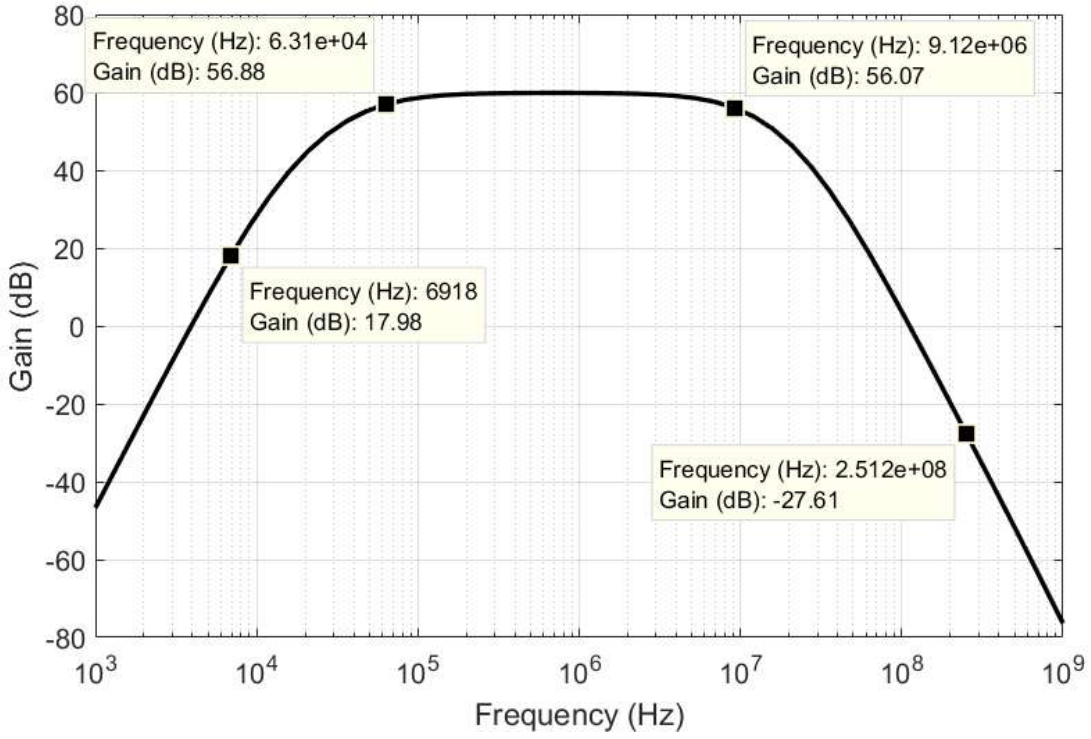

Figure 3-13: RX Baseband Transfer Function

Although the desired signal has already been demodulated down to baseband, there is still some leakage at RF due to the finite Q of the PA inductors. Each amplifier stage, including the LNA, has extra capacitance added to the output to act as a first-order low-pass filter. In total, there are 4 such amplifier stages, creating a 4^{th} order low-pass filter that can heavily attenuate any interference from the carrier. Using capacitors of less than 10 pF, a blocker rejection ratio of -75 dB is achieved at the output of the amplifier chain. Fig. 3-13 shows the transfer function of the RX amplifier chain. At the frequencies of the backscattered signal, the amplifier chain has 60 dB of gain, while at the frequency of the TX leakage at RF, there is a loss of -27 dB. This is equivalent to 77 dB of blocker rejection. As shown in Fig. 3-14, this blocker rejection is enough to ensure that there is only 1.5 dB of gain compression at a carrier leakage magnitude of 100 mV. Keep in mind that the typical measured blocker amplitude at the ammeter is less than 10 mV.

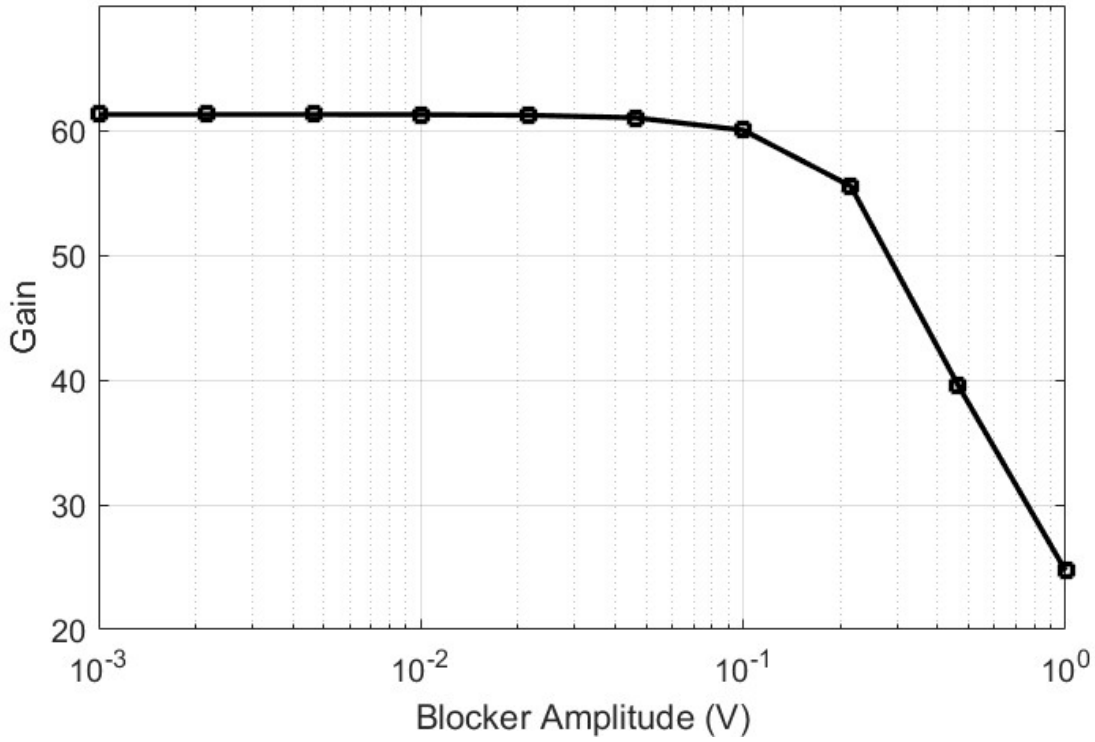

Figure 3-14: Gain in dB of the baseband receive chain vs. blocker amplitude at ammeter.

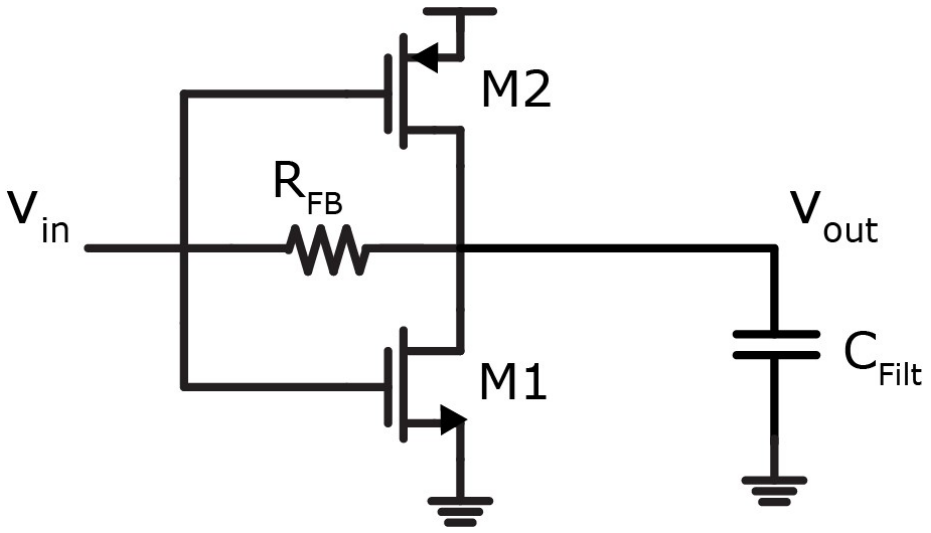

Figure 3-15: Schematic of self-biased Class-AB LNA.

3.4.2.4 LNA Design

There are several requirements of the first stage amplifier of the receive chain. The LNA should consume a small fraction of the power of the transmitter while maintaining high enough sensitivity to recover the backscattered signal. The amplifier should be linear enough make sure that any LO leakage from the transmitted carrier does not saturate the amplifier. And the input impedance should high enough so that the corner frequency of the high-pass filter created by the DC blocking capacitor and the input impedance of the amplifier is lower than the lowest frequency content of the miller-modulated data required. The self-biased inverter-based amplifier shown in Fig. 3-15 satisfies all three requirements.

The gate and drain are connected by a large bias resistor, ensuring that the DC bias of the input and output of the amplifier keeps both PMOS and NMOS devices biased in saturation. The design is efficient because the complimentary input devices give two sources of g_m for only one bias current. The total gm at is gm1 + gm2, so the input-referred noise power spectral density would be

$$v_{n,input}{}^2 = \frac{4kT}{g_{m1} + g_{m2}} \frac{\gamma}{\alpha} \Delta f \tag{16}$$

The main contribution to amplitude noise would be the first-stage LNA. And the total input-referred noise voltage at the frequency band of the LNA would be approximately:

$$v_{n,integrated}{}^2 = \int \frac{4kT}{g_{m1} + g_{m2}} \frac{\gamma}{\alpha} |H_{LNA}(f)|^2 \, df \tag{17}$$

where

$$H_{LNA} = \frac{2\pi f * R_{in} C_{Block}}{1 + 2\pi f R_{in} C_{Block}} \frac{1}{1 + 2\pi f * R_{out} C_{filt}} \tag{18}$$

Also, these complimentary input transistors also are more tolerant of higher swings. The high-pass filter used for DC offset cancellation can be constructed with a relatively small 30 pF capacitor and the large yet predictable input impedance of the biasing resistor connected in feedback. The simualted amplitude of the backscatter signal on the ammeter is simulated to be 173 uV at link distance of 1.5 cm, so the ammeter was sized to have to an input-referred integrated noise voltage with a 1 uV standard deviation to ensure robust low BER in the receiver. The input-referred SNR vs. Link Distance is shown in Fig. 3-16.

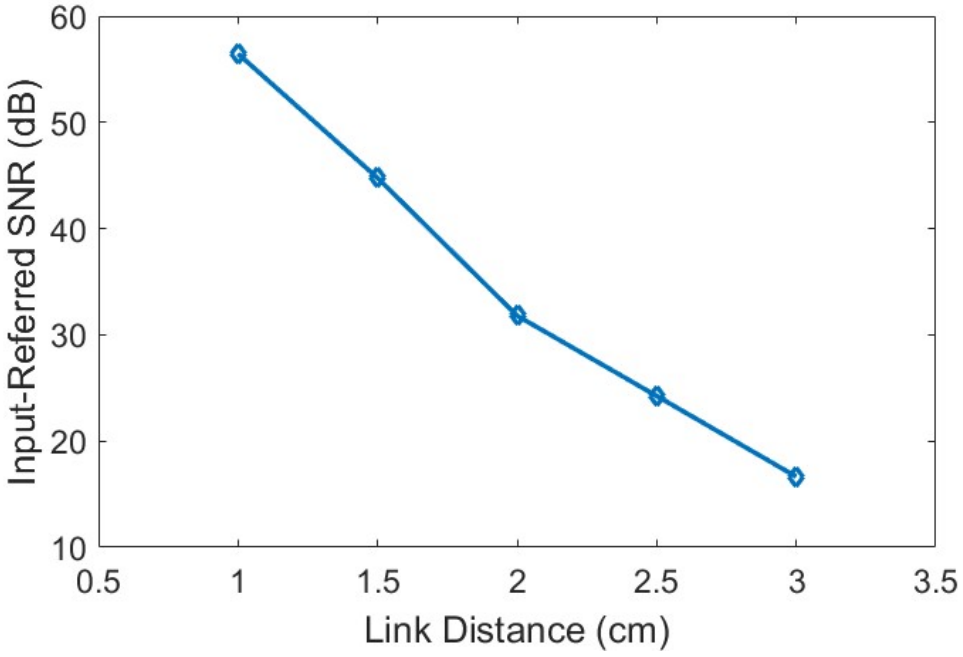

Figure 3-16: Input-referred SNR at the ammeter vs. Link Distance

3.4.2.5 Baseband Differential Amplifiers

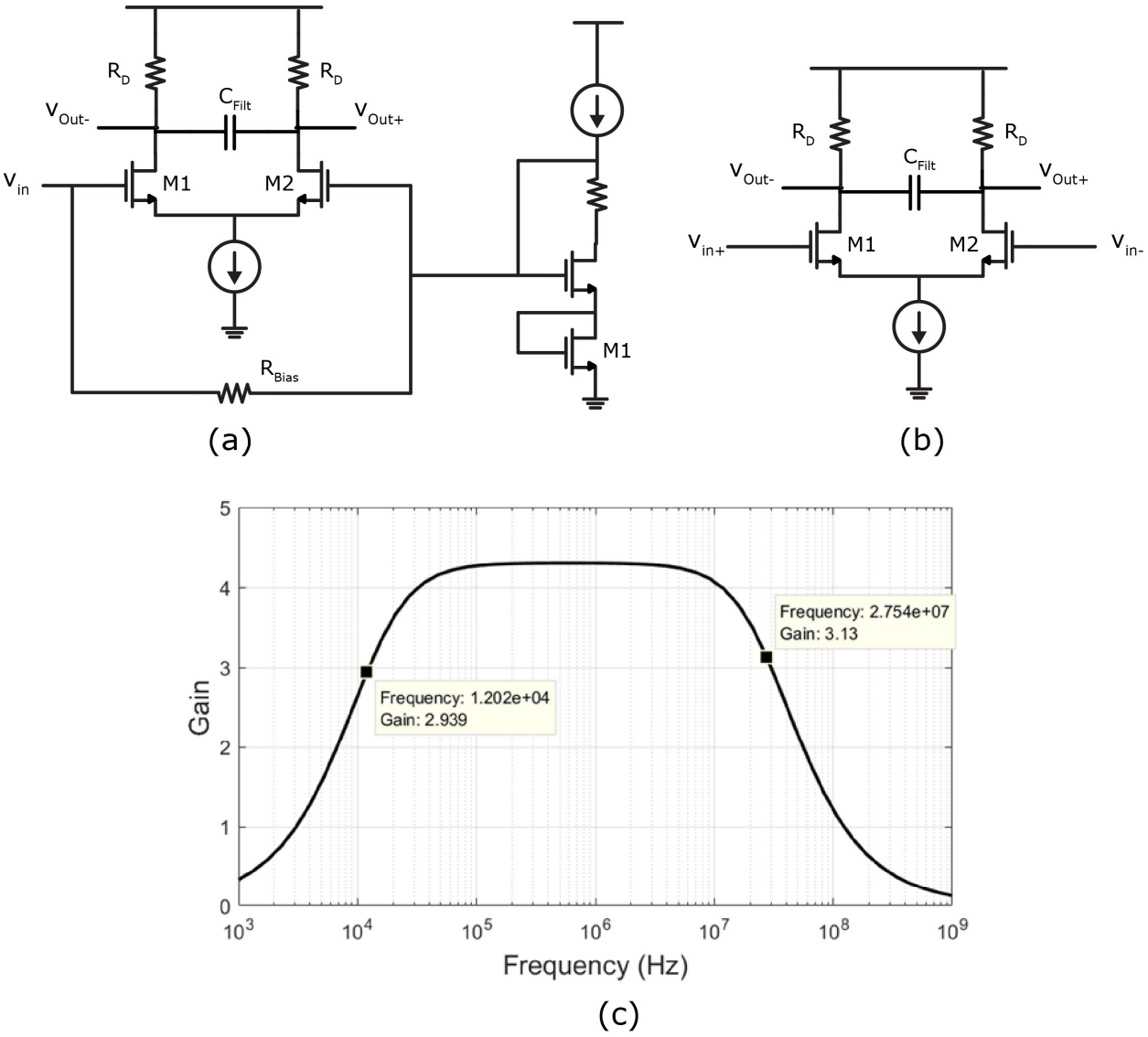

Figure 3-17: a) Schematic of Single-Ended to Differential Converter, b) Schematic of differential amplifier, and c) Transfer Function of one stage of the differential amplifier

The first-stage LNA is designed to be single-ended because the backscatter signal recovered at the ammeter is single ended. To ensure robustness against power supply noise and common-mode noise, the later stages of the receive chain are designed differentially. The following two amplifiers are designed to be simple differential pairs. Each amplification stage is designed to have a gain of 4, a high-pass corner frequency of 12 kHz, and a low-pass corner frequency of 27 MHz. Each amplifier stage was designed to have a low gain to be an easy way to ensure that the baseband amplifiers operate robustly across process and temperature variations. The relatively low-output impedance of each amplifier makes it so the input transistors stay in saturation across corners. Fig.

3-17 shows the schematic and simulated transfer function of the differential pairs used in the baseband receiver chain.

There isn't a significant penalty to using multiple low-gain differnetial stages in this system. Multiple stages of amplification are helpful to create a high-order baseband filter to filter out any transmit carrier leakage. In addition, there isn't any feedback in the receiver that would result in instability of the baseband chain. The dominant source of power consumption is the LNA, which is limited by the desired input-referred noise of the system, so having multiple low-gain baseband amplifiers adds a trivial amount of power consumption to the chip.

3.4.3 Phase Noise

For RFID readers, phase noise leakage from the LO of the TX to the RX is often the primary cause of lowered receiver sensitivity [CHIU]. As seen in Fig. 3-18, the thermal noise at the input of transistors of the Class E/Fodd PA have a low gain to the PA output because the transistors are operating in a non-linear switching mode. Mixing down the carrier of the received signal with a carrier with correlated phase noise lowers the contribution of the phase noise [CHIU]. In this ammeter-based PA transceiver, the same clock simultaneously generates the carrier for the received backscatter, while demodulating the received backscatter back to DC, so there should be correlation between the phase of the clock ammeter resistance.

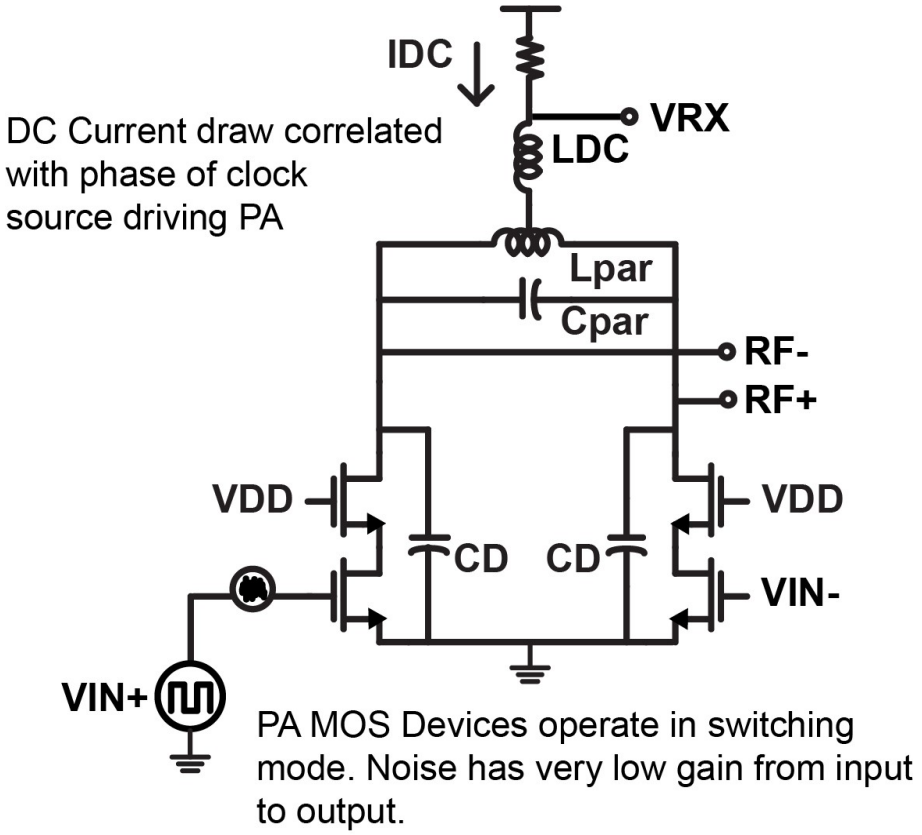

Figure 3-18: Transceiver Phase Noise Rejection

3.4.3.1 Simulated Phase Noise Transfer Function

Although the ammeter-based reader down-converts the desired backscatter signal to baseband, it also downconverts the phase noise of its own LO to baseband. Variations in the phase of the input signals driving the differential switches of the Class E/Fodd PA could potentially change the current through the R_{amm}. The voltage induced on the R_{amm} by the integrated down-converted phase noise power can lower the sensitivity of the receiver. Fig. 3-19 shows the setup of the phase noise experiment. The effect of phase noise was simulated by using a sine wave with a similar phase noise power spectral density to signal generator used to test the 1 mm^3 transponder in Chapter 2. This sine wave is passed through a single-ended to differential converter and fed into a chain of inverters to limit its amplitude to that of a square wave. Then the effect of the phase noise on V_{amm} was measured through harmonic balance simulation.

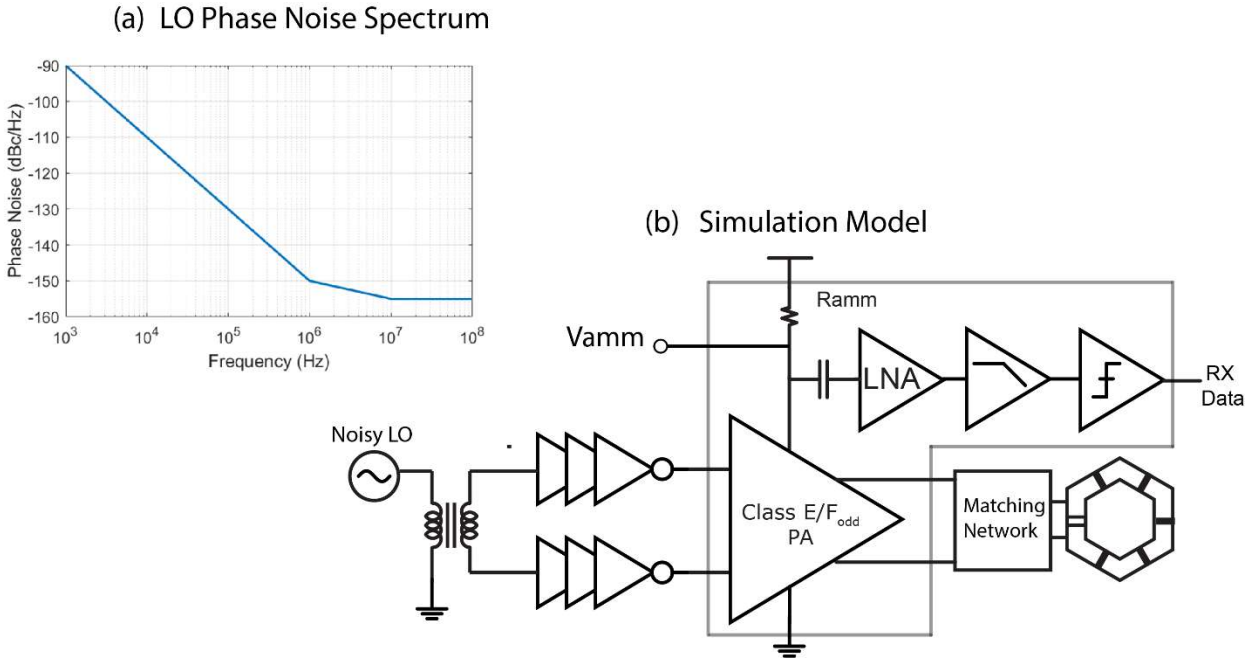

Figure 3-19: (a) Phase noise spectrum of LO (b) Simulation model used to determine effect of down-converted phase noise on receiver sensitivity.

To calculate the effective dBc/Hz of the phase noise signal, the dc current through the ammeter needs to be compared to the noise spectral density of the current of the downconverted phase noise at V_{amm}. The difference in dB between the downconverted phase noise current and the DC current through the ammeter R_{amm} is the relative phase noise spectral density in dBc/Hz. Fig. 3-20 shows the phase noise density.

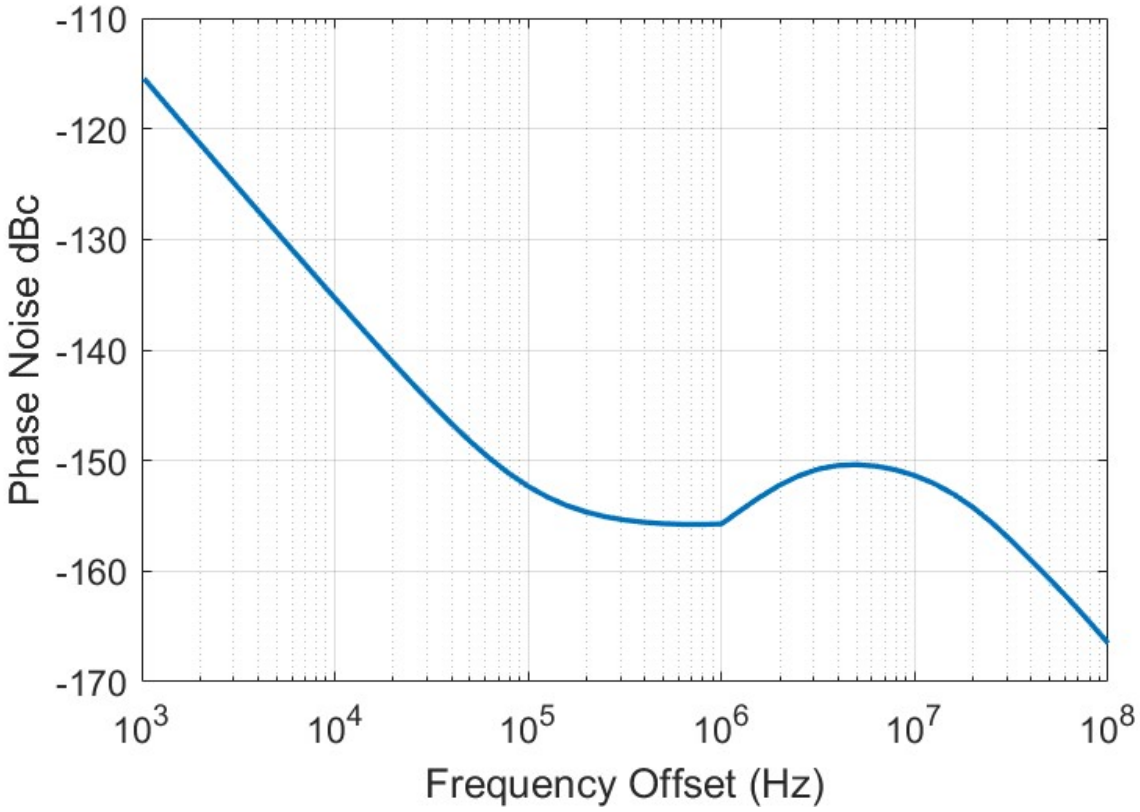

Figure 3-20: Phase noise vs frequency offset at V_{amm}.

3.4.3.2 RX Filtering of Phase Noise

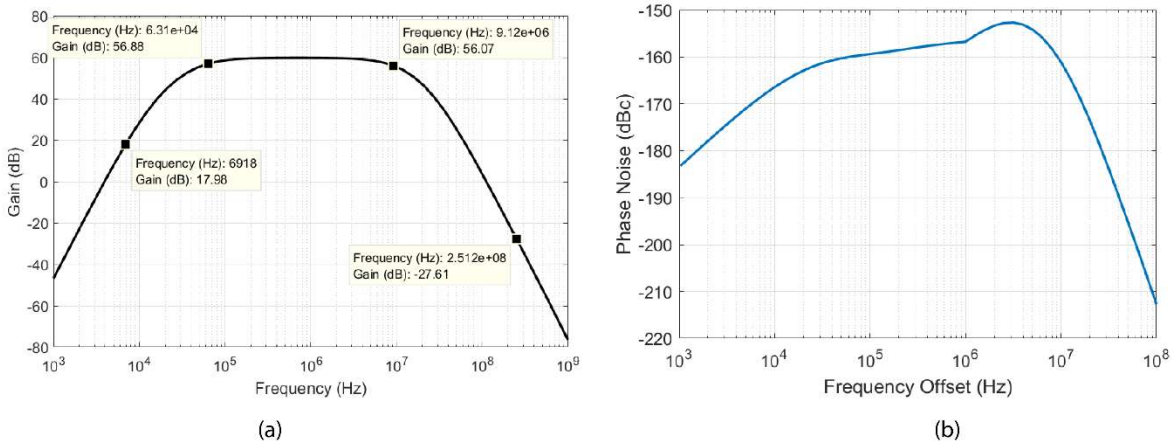

Figure 3-21: (a) Transfer function of receiver. (b) Phase Noise in dBc input-referred to receiver input.

The high-pass characteristic of the baseband receive chain is very helpful in reducing the impact of the basband down-converted phase noise. Shown in Fig. 3-21 is the input-referred phase noise vs frequency spectrum in dBc at the ammeter input. The integrated noise voltage over this

bandwidth is less than 600 nV, significantly lower than the designed LNA input-referred noise of 1 uV. This is another advantage of using Miller encoding. As shown in Fig. 3-20, a large portion of the phase noise is situated close to the carrier. Using miller encoding moves frequency content of the backscatter signal away from the carrier, so the phase noise that is close to the carrier can be filtered out with simple high-pass filters.

3.5 Discussion

The blocker rejection method described in this chapter can be used for any near-field backscatter link. As shown in (7) and (8), the performance of this architecture is limited primarily by the efficiency of the switching power amplifier, so the design scales well for any system that has a carrier frequency where non-linear switching PA's can operate efficiently. The specific IC designed in this chapter can be used for any near-field RFID link with a carrier center frequency of around 300 MHz. The next chapter will explore the antenna deisgn concerns and experimental setup required to demonstrate the chip to delivering power to a proprietary implant similar to the one in [MUL2], while at the same time recovering backscattered data at a low BER.

Chapter 4:

Prototype and Experimental Setup

4.1 Test Chip Implementation

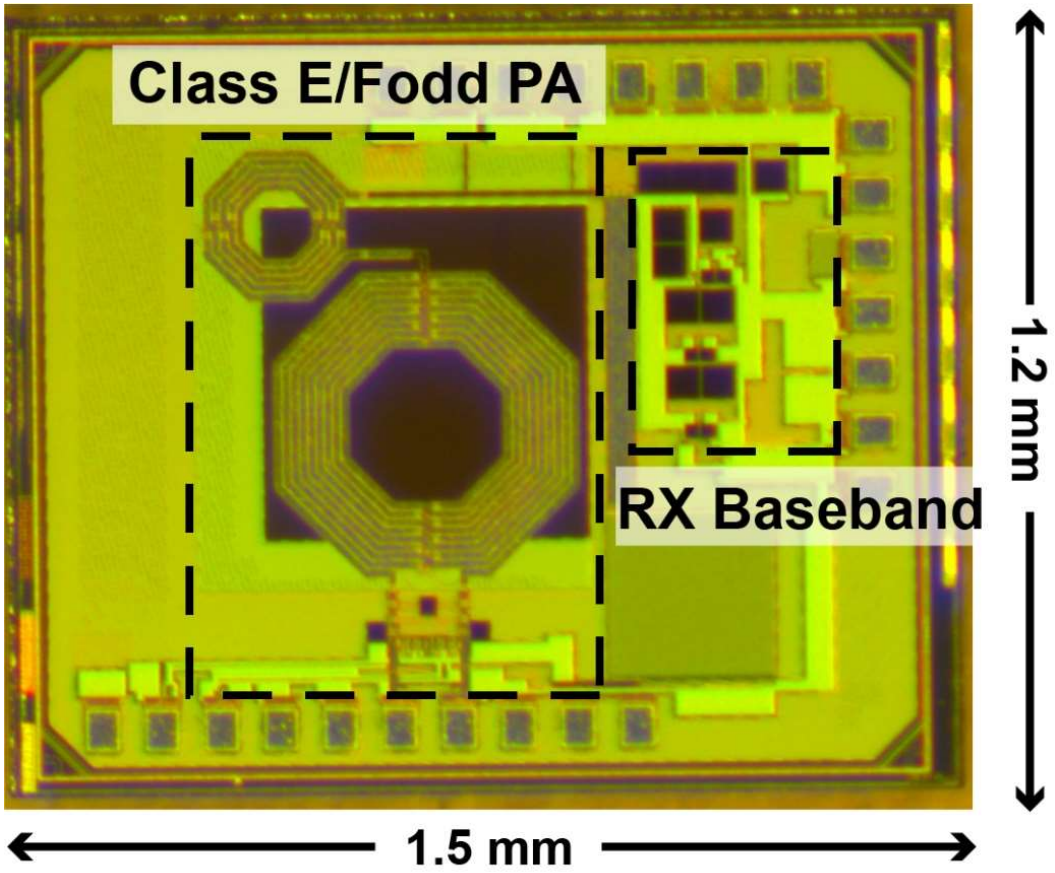

Figure 4-1: Die Photo

The design was fabricated in 65 nm in a general-purpose CMOS process with 7 metal layers, 2 thick metal layers, and 1 top-level Aluminum layer from TSMC. A chip micrograph is shown in Fig. 4-1. The chip consists of a Class E/Fodd Transmitter and a baseband receive chain. The passive components of the PA, the filtering and amplification stages of the receiver, and biasing circuitry are all integrated on the die. The total chip area including pads is 1.5 mm x 1.2 mm. The active area of all the circuitry is .89 mm^2. The area and power consumption of the IC are dominated

by the Class E/Fodd PA, which consumes 35 mW and has two large integrated inductors. Table 4-1 lists the power and area breakdowns by block.

TABLE 4-1: Power and Area Breakdown of IC

	Area	Power
TX Switching PA	.66mm^2	35 mW
RX Baseband Amplification	.23 mm^2	4.4 mW
Total	.89 mm^2	39.4 mW

4.2 Prototype Board

Figure 4-2: Test PCB for reader.

The printed circuit board used for testing was created for two purposes. One function is to characterize the segmented antenna to determine the center frequency of the matching network and the impedance of the antenna. The primary purpose of the printed circuit board is to allow

testing of the reader's functionality. Once characterized, the actual size of such a system would be closer to the size of the loop antenna.

4.3 Power Delivery

A highly efficient power amplifier on-chip means nothing if power cannot be efficiently transferred from the reader IC to the external reader's antenna. In addition, ensuring safe power transfer from outside the skull to inside the head is also important for a wearable RFID reader. This section outlines the various optimizations and design choices made in the antenna and matching network in order to ensure efficient and safe operation of the external reader.

4.3.1 Antenna Design

The primary limitation for wireless power transfer in the human body is Specific Absorption Rate (SAR). SAR is defined as

$$SAR = \frac{\sigma |E|^2}{\rho} \tag{12}$$

where E is the electric field, σ is the conductivity of human tissue, and ρ is the mass density of the human tissue. Even though a loop antenna with a 1.6 cm diameter is small compared to the wavelength of a 300 MHz carrier in human tissue, its length is still electrically significant enough to induce a non-uniform electric field in the human tissue below it. These electric field hotspots can limit the maximum power able to be delivered from the reader to the implant through the skull.

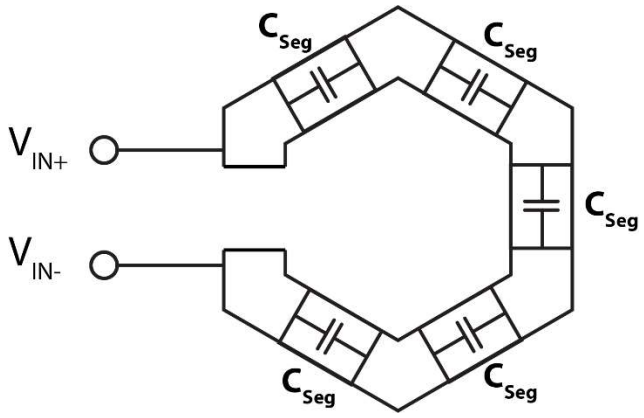

Figure 4-3: Loop Antenna with Segmenting Capacitors

To solve this problem, a hexagonal loop antenna that is segmented by series capacitors was designed [BJO]. These series capacitors resonate out the inductance of the antenna and spread the electric field evenly throughout the tissue underneath the reader. This topology allows up to 30%

more power to be delivered to the antenna while still satisfying the maximum SAR limit mandated by the FCC [MARK3].

4.3.2 Antenna Optimization

The antenna impedance is mostly inductive, and its dimensions are too small compared to the wavelength of the carrier to any significant radiation resistance. Therefore, to maximize the amount of power delivered by the antenna, the real part of the resistance of the antenna must be minimized. The segmenting capacitors do spread the electric field, but these surface mount components add a large amount of resistance in series with the coil. Because the segmented antenna has such a high Q, any series resistance will greatly lower the S21 of the system. Shown in Fig. 4-4 is the simulated S21 of a 1.5 cm link in air between a segmented coil and the implant coil vs segmenting capacitor resistance.

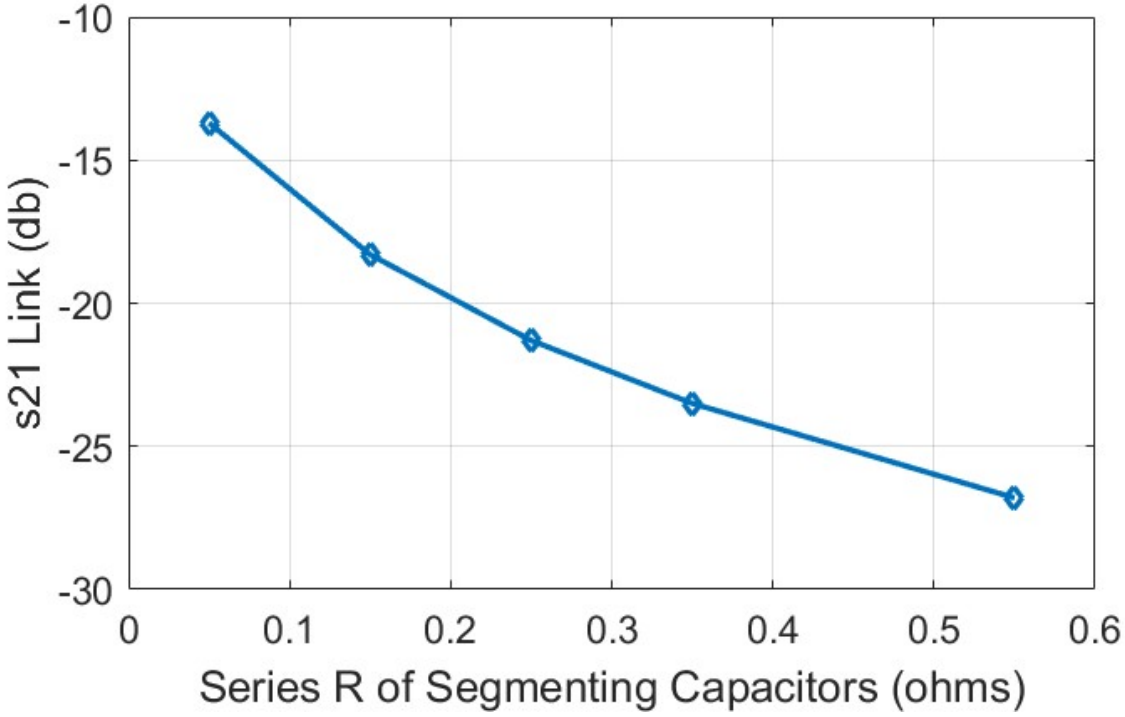

Figure 4-4: Simulated S21 of the link vs. series resistance of segmenting capacitors.

A small amount of resistance can greatly lower the Q of the mainly inductive antenna, greatly lowering the power transfer of the reader to the implant. Even surface mount capacitors marketed as high-performance RF capacitors still have an ESR on the order of 0.1 ohms each. 5 series segmenting capacitors can add 0.5 ohms to the antenna. To lower the loss from these series capacitors, instead of using 1 capacitor for each segment, the antenna was designed to have two capacitors in parallel to connect each segment of the loop with the next section. This topology also reduces lowers loss by minimizing current constriction at the leads of the segmenting capacitors, which allows the current to spread out more while flowing through the loop.

4.3.3 Matching Network

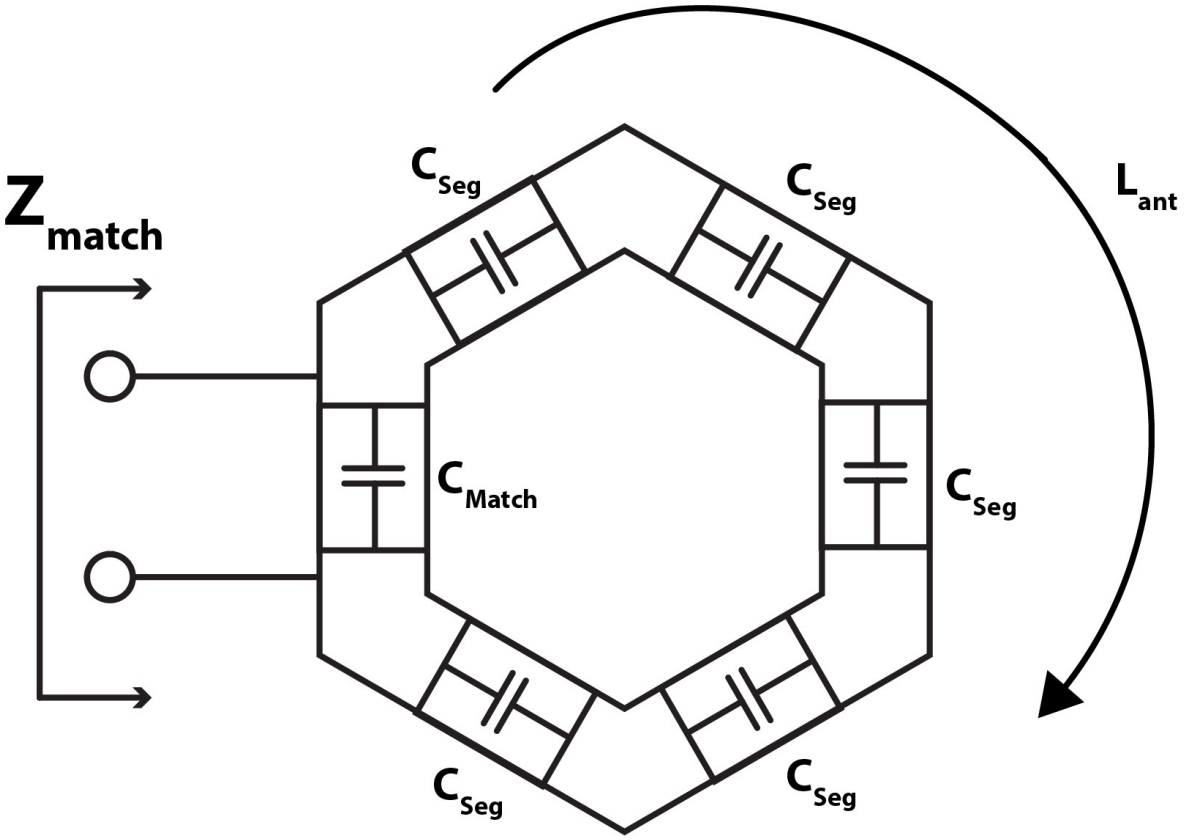

Figure 4-5: Lumped View of Segmented Antenna Impedance

The goal of the matching network is to maximize the efficiency of the transmitter while ensuring proper class E/Fodd operation of the transmit PA. The magnetic field generated by the transmit coil is dependent on the current through it. The impedance of the unmatched antenna is

$$Z_{ant} = (\omega L_{Ant} - \frac{5}{\omega C_{Seg}})i + R_{Ant} + R_{Cseg} \tag{13}$$

With a parallel match, the impedance at the resonant frequency becomes

$$Z_{match} = \left(1 + {Q_{Ant}}^2\right) = R_{Ant} \tag{14}$$

Where

$$Q_{Ant} = \frac{\omega L_{Ant} - \frac{1}{\omega C_{Seg}}}{\left(R_{Ant} + R_{Cseg}\right)} \tag{15}$$

Matching the antenna to a higher impedance lowers the effect of any series resistance from the PCB traces and bond-wires in between the antenna and the TX PA. Fig. 4-6 shows the design and

dimensions of the segmented antenna and matching network and the simulated matched impedance of the antenna as a function of frequency.

Figure 4-6: Segmented Antenna and Matching Network

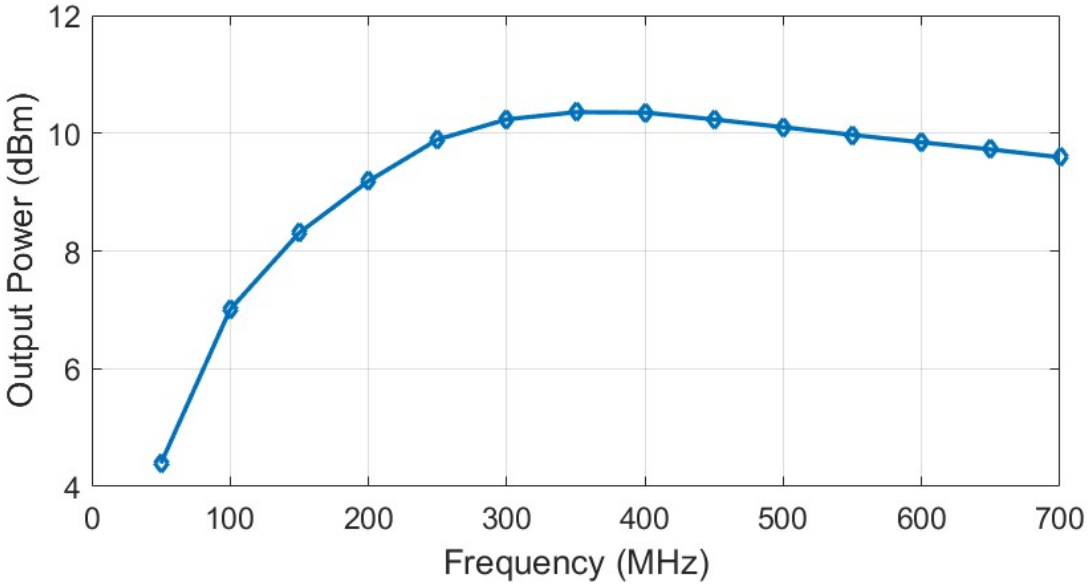

Figure 4-7: PA output power vs frequency when driving a 50 ohm real load.

While the switching PA remains relatively efficient over a wide band as shown in Fig 4-7, the matching network of the segmented antenna has an extremely narrow bandwidth due to the high Q of the Antenna. The real part of the unmatched antenna impedance is both low and unpredictable because it comes primarily from the PCB trace impedance, the series resistance from the surface mount segmenting capacitors, and solder bumps used to attach the segmenting capacitors. This effect results in a matching network where the antenna is matched over a narrowband and exact value of the impedance match is unpredictable (see Fig. 4-6). Outside the center frequency of the matching network, the segmented antenna has a low impedance. With low load impedances (< 1 ohm) presented at its output, the class E/Fodd PA does not function efficiently. To ensure acceptable PA efficiency over a wider bandwidth, series capacitors are added in between the antenna and PA to increase the impedance seen by the PA.

4.4 Proprietary Implant Tag

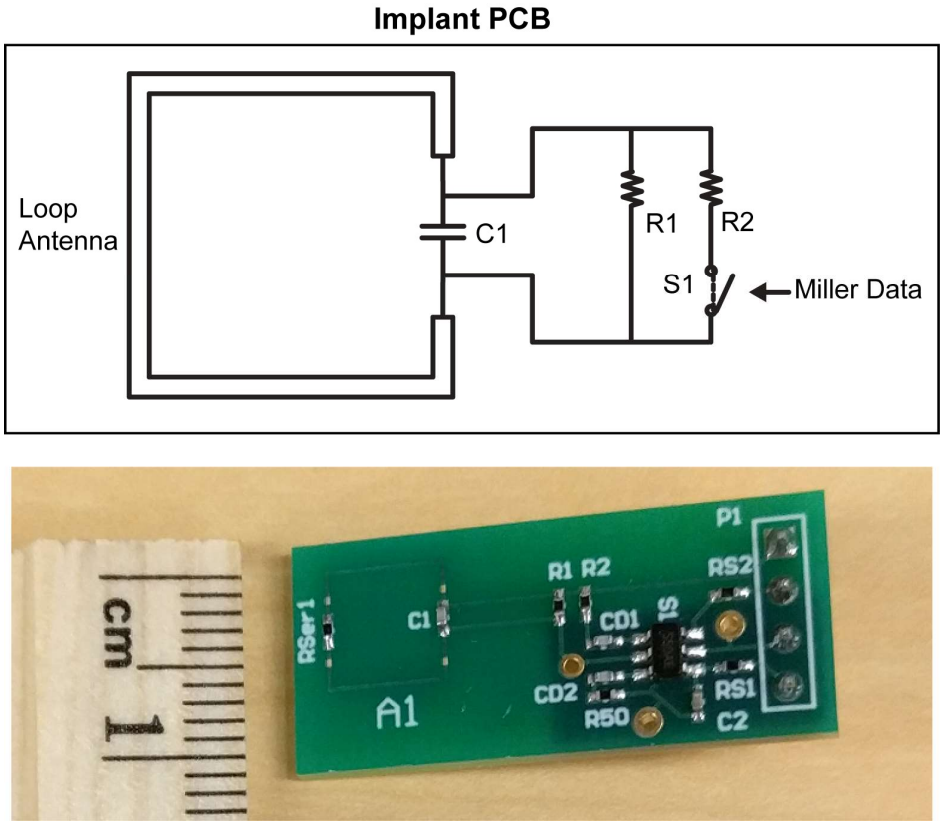

Figure 4-8: Design and photograph of proprietary implant tag.

The reader was designed to deliver power to and communicate with an existing implant described in [9]. The implant chip is complex and consists of an RF transmitter, RF-DC power conversion circuitry, and 64-channels of amplifiers meant for neural signal acquisition. To simplify testing, a proxy board was designed to have the same antenna dimensions and similar impedance characteristics to the implant shown in Fig. 4-8. This board consists of a loop and surface mount components meant to replicate the load characteristics of the ECoG chip designed in [9]. A surface mount capacitor is placed in parallel with the loop antenna to act as a matching network. Parallel surface mount resistors with similar resistance values to the rectifier in [MUL2] are driven by the antenna. One of the resistors is connected in series with a switch so that the implant board can communicate through backscatter by modulating its load impedance. The switch S_1 is driven by an Opal Kelly FPGA board outputting a PRBS-7 Miller-encoded data pattern.

Testing of the power delivered to the implant's is done by measuring the voltage across R_1 with a high frequency voltage probe. The current can be derived by calculating the impedance of the implant during each phase of operation. In [MUL2], the implant was designed to rectifiy the output of its antenna during both phases of its backscatter. Depending on whether S_1 is switched on or off, the real resistance of the implant will either be R_1 or $\frac{R_1 R_2}{R_1+R_2}$. The normalized difference between

these two impedances, also known as the modulation depth, is one factor determining the strength of the backscattered signal.

4.5 Measurements in Air

Power transfer and data-link measurements were taken with the implant coil at various distances away in air to compare with existing trans-cranial data/power transfer systems. At 1 cm coil separation, the design is able to deliver a maximum of 1.25 mW to the implant at a TX power consumption of 35 mW, for an overall link efficiency of 3.3%. Fig. 4-9 shows the BER vs link distance in air. The minimum BER is primarily limited by test equipment, specifically the amount of data the oscilloscope used can capture. Fig. 4-10 shows the overall link efficiency vs. frequency at a link distance of 1.5 cm. Overall link efficiency is found by taking the total amount of power delivered to the load of the implant and dividing that by the power consumption of the TX PA. This metric takes into account both PA efficiency and link loss. The PA's load is a highly-tuned inductive load matched to a real impedance, so optimal power transfer occurs within a narrow-band.

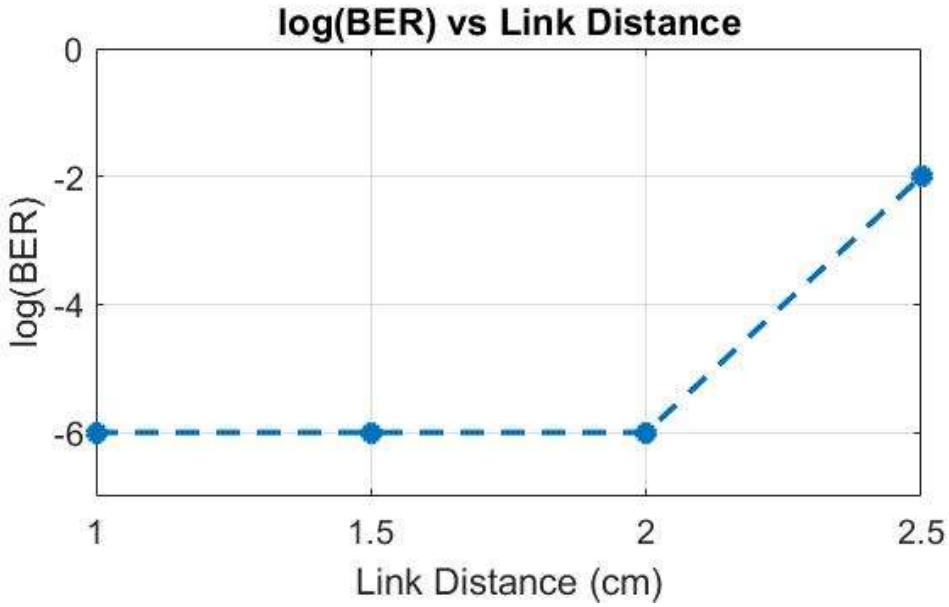

Figure 4-9: BER vs. Link Distance

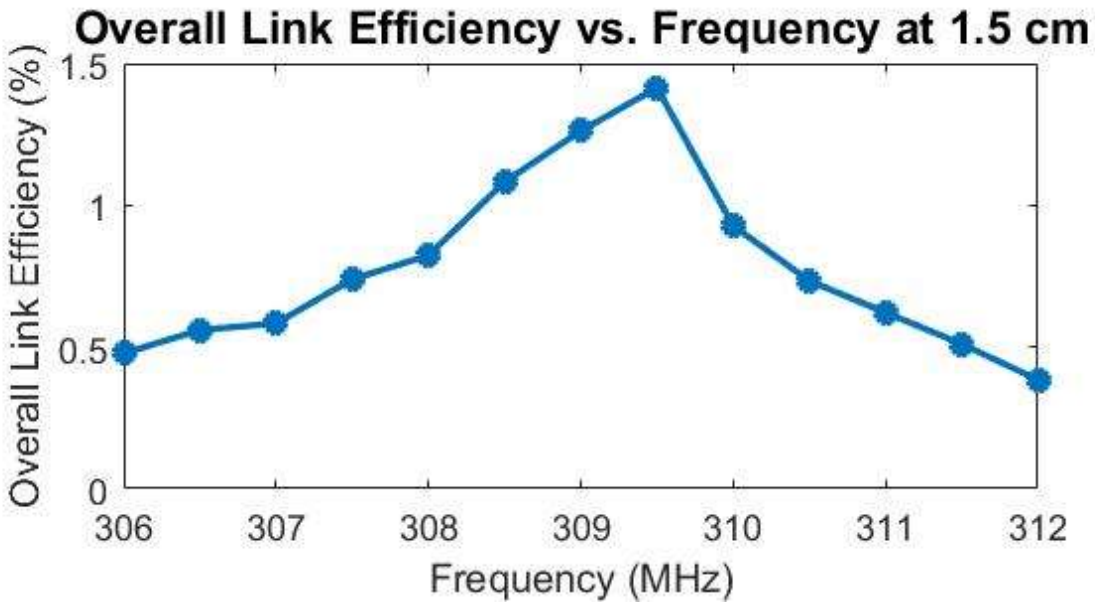

Figure 4-10: Overall Link Efficiency vs. Frequency at 1.5 cm Link Distance

4.6 In-Vitro Experiment

4.6.1 Channel Setup

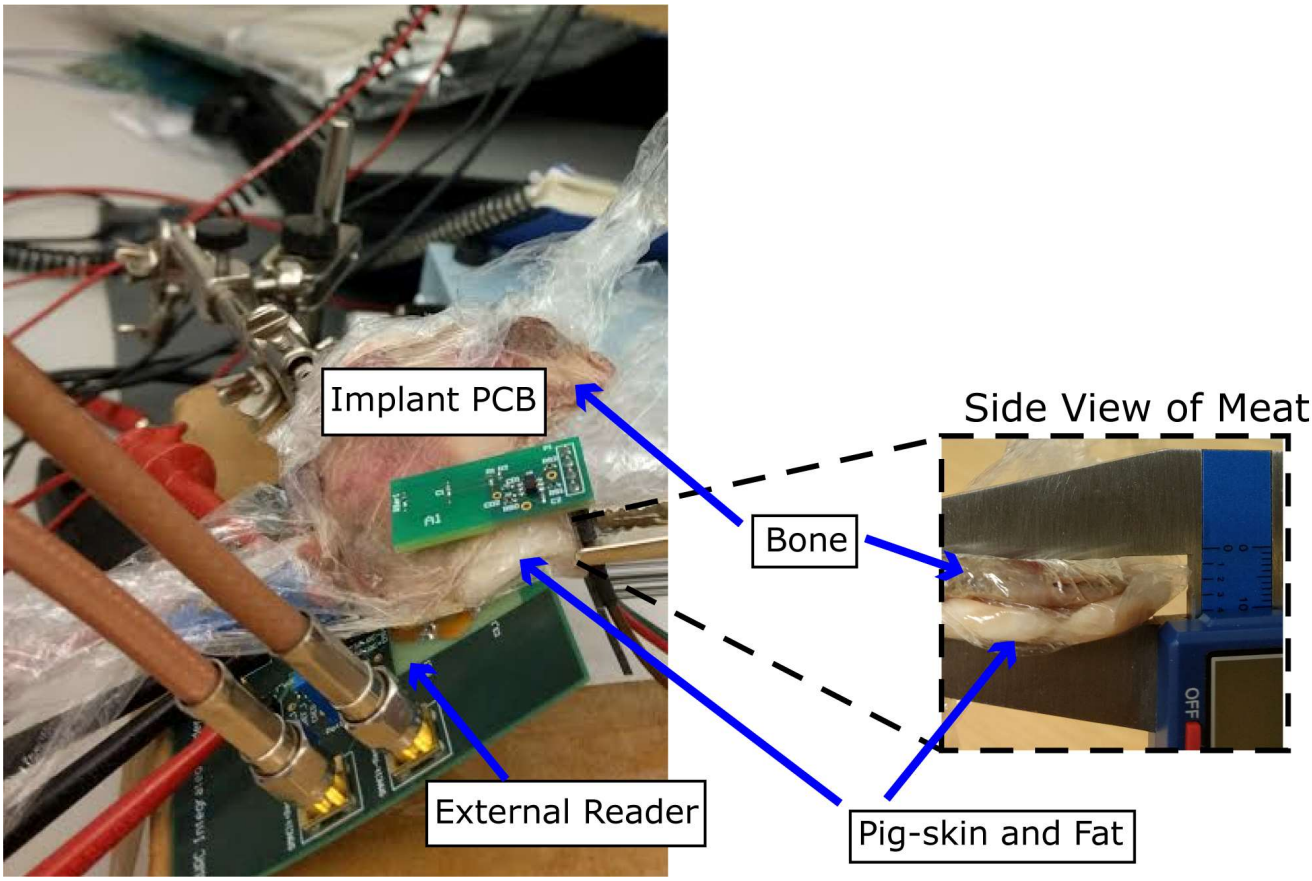

Figure 4-11: Measurement Setup with Reader Communicating with Implant through Proxy for Human Skull

The RFID reader is designed to communicate through an adult human skull. Because of the difficulty in procuring a human skull, a channel meant to have similar loss characteristics to a human skull was constructed out of various meats from the grocery store. To create a medium similar to the skin and fat of a human scalp, we used the skin from a slab of pork belly with the fat layer significantly trimmed down. The flat part of the bone from a t-bone steak was used as a stand-in for the relatively flat geometry of the cranium bone from a human. The two pieces of meat were stacked on top of each other to create the channel shown in Fig. 4-11. The reader antenna was placed on the skin side of the channel, and the implant antenna was placed on the bone side of the channel.

4.6.2 Measurement Results in Tissue

TABLE 4-2: System Performance in Tissue

System Parameter	This Work
External Antenna	1.5 cm
Internal Antenna	6.5 mm
Communication	Transcranial 1 cm
Carrier Frequency	309 MHz
Data Encoding Scheme	Miller
Bit Error Rate	<1E-6
Transmit Power	35 mW
Received Power	790 uW
Overall Link	2.3 %

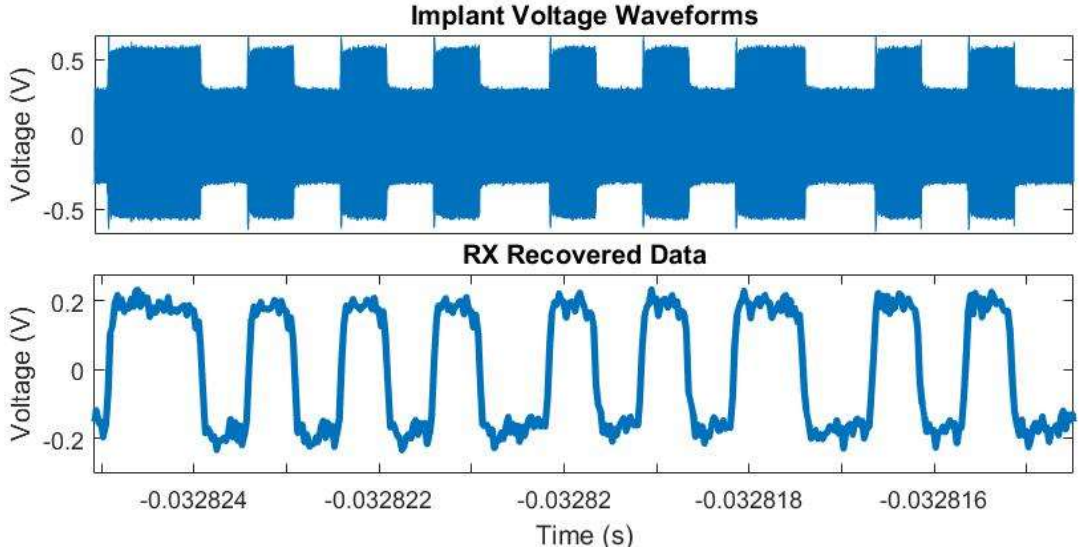

Figure 4-12: Implant and RX Waveforms

Using the measurement setup above, power delivery and data telemetry were tested. Table 4-2 summarizes the overall results of the testing in tissue. The design is able to deliver a maximum of 790 uW to the implant at a TX power consumption of 35 mW, for an overall link efficiency of 2.3%. The receiver's data rate with miller modulation is 2 Mbps at a BER of less than 1e-6 with this configuration. Fig. 4-12 shows the backscatter waveforms from the implant and the recovered data from the reader's TX.

4.7 Comparison and Discussion

TABLE 4-3: Comparison with Prior Art

	2008 [MAND]	2012 [RUSH]	2015 [KIA]	**This Work**
Powering Carrier (MHz)	25	5	13.56	**309**
Data Carrier (MHz)	25	46	50	**309**
Data Rate (Mb/s)	2.8	3	13	**2**
TX Coil Diameter (cm)	3.5	3	3.2	**1.6**
Implant Coil Diameter (mm)	35	10	10	**6.5**
Blocker Rejection Method	Envelope Detection	Different Data/Power Frequency	Different Data/Power Frequency	**Ammeter-Based**
Separate Power and Data coils?	No	Yes	Yes	**No**
BER	1E-06	2E-04	4.3E-07	**<1E-06**
TX Efficiency	N/A	N/A	61.8%	**54%**
Link Efficiency	N/A	N/A	19.3%	**3.3%**

Table 4-3 summarizes the performance of the novel RFID reader compared to state-of-the-art transcranial links. The measured results for these for links with a 1 cm distance away in air. Compared to other work this reader uses a much higher frequency for power and data communications. This higher frequency allows both the TX coil and the implant coil to be much smaller. Specifically, because its diameter is half of previous work, the TX coil consumes 25% the area than other systems. The implant coil diameter is also far smaller. In addition, the ammeter based architecture allows the external reader to be highly integrated for an even more compact form factor while still enabling a sensitive receiver with low BER.

In this transcranial link, the power and data links operate on the same carrier frequency of 309 MHz, which prevents the need for separate coils for data and powering. Also, implant design is simplified because no frequency generation circuitry is needed to generate separate carriers. Compared to other RFID readers, this work uses no external components to isolate TX from RX.

In systems where the implant would require extra power such as BMI systems using neural stimulation with high currents, the other readers could have a role. This system was designed to power and interrogate a uECoG implant meant for chronic neural recording. As stated in Chapter 1, many neurological diseases such as seizures, Alzheimer's, and Parkinson's can be better treated by physicians if long-term ECoG data is available. Having a lightweight, easy to wear reader allows patients to wear these interrogators

This architecture can be applied over a wide range of frequencies for near-field power/data links in a wide variety of applications. As shown in Chapter 3, the performance of the transceiver improves as the strength of coupling between reader and implant increases and as efficiency of the switching PA increases. Improvements in either area would further push the performance limits of the system, allowing for efficient power delivery to many types of implants using wireless communications in the human body.

Chapter 5:

Conclusions and Future Work

5.1 Contributions

This work describes the design of an efficient and compact RFID Reader architecture for near-field powering and communications with mm-sized neural implants. The primary contributions of this work are

- The design of a novel blocker rejection method for RFID Readers that uses the non-linearity of a Class E/Fodd Power Amplifier to demodulate the received backscatter and reject the self-jammer without bulky external components.
- Design methodology for a fully-integrated 300 MHz Class E/Fodd PA
- The exploration of efficient power delivery to segmented loop antennas.
- Prototype of a compact, isolator-less RFID reader that can power and communicate with uECoG Neural Implants.

This design, in combination with the wireless uECoG presented in [MUL2], could be part of a wearable system used for safe and robust chronic neural recordings in a clinical setting.

5.2 Improvement and Design Perspective

When designing any integrated circuit for a wired or wireless transceiver, optimization is important to ensure performance, energy efficiency, and functionality are all maximized. These optimizations have to be performed given certain practical constraints given the requirements and application of the system being built.

In this specific case, the goal was to build a compact RFID Reader meant to deliver power through the skull to a neural implant, while receiving backscattered neural data from that same implant. To ensure a lightweight factor that is wearable on a person's head, a transceiver architecture that didn't require bulky external components to isolate the self-jammer from the received backscatter was required. In addition, making the transceiver more efficient was essential to reducing the weight of a battery that would power the reader.

The ammeter-based Class E/Fodd architecture proved to be an effective solution to both these problems. Significant effort was spent making the IC as small as possible, while limiting the amount of external passive components to push the form factor to its very limit. An arbitrary

constraint based on previous RF transceiver chips taped out in BWRC of using less than 1.5 x 1.5 mm die area was placed on the chip.

The problem is that the Q of integrated inductors in the 65 nm CMOS technology is low at frequencies around 300 MHz unless the inductors approach dimensions of over 1 x 1 mm. Shown in chapter 3, the efficiency of the class E/Fodd PA is heavily dependent on the loss factor of its passives. In addition, the received backscatter signal also improves with the Q of the inductors used. This suggests that using a chip area of 2 x 2 mm or using external SMT inductors would have resulted in greater reader performance in both power delivery and sensitivity.

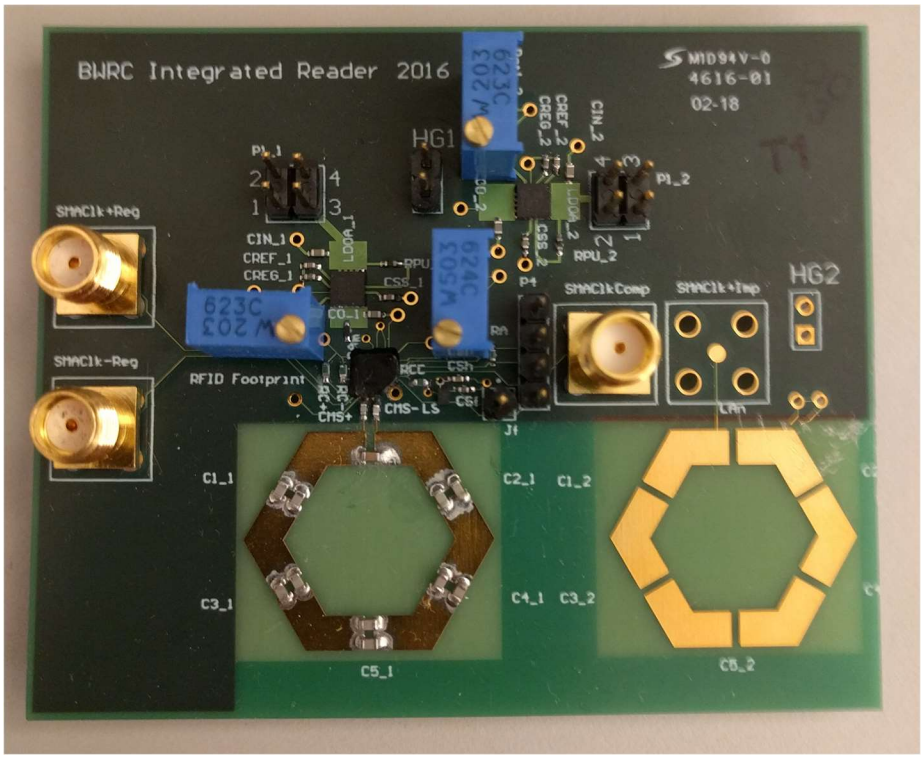

Figure 5-1: Prototype board for integrated reader. Increasing die area of IC would not have contributed much to radio size.

Shown in Fig. 5-1, the antenna diameter of the external radio was already 1.6 cm. An IC, that was double the size would still consume only 2% of the area of the antenna, yet the efficiency could have been much higher. Because the market for brain machine interfaces would be relatively small compared to high volume consumer electronics, cost would be limited to mask cost and engineering effort instead of die size, so the insistence of keeping the chip to below 1.5 x 1.2 mm was not necessarily the best choice for the problem at hand.

5.3 Future Work

On its own, an RFID reader like the one presented in this thesis would be effective for specialized clinical treatments such as seizure localization using ECoG arrays or for control of more rudimentary prosthetics limbs with fewer degrees of freedom than a fully-functional human arm and hand.

However, a single trans-cranial RFID radio, no matter how efficient and sensitive cannot single-handedly meet all the requirements of a Brain Machine system with all the functionality required for precise neural prosthetic control or for mapping the entire brain for neuroscience purposes. Available power to the implant scales inversely with frequency, yet data rates for neural signals required for precise motor control of prosthetic arm are estimated to be about on the order of 100's of Mb/s per second. Separate radios should be used for power and data communications for such future systems. In addition, milliwatts of power would be required for clinical deep brain stimulation. An RFID reader like this could be used to deliver power to an implanted neural recording and stimulation system, while receiving lower data rate diagnostic data that would ensure system robustness and help calibrate each implant at system start-up. Lower frequencies could be used to safely deliver a higher amount of power through the skull to a centralized super capacitor that can be used to power all these implants.

References

[AFL] Aflalo et al., “Decoding motor imagery from the posterior parietal cortex of a tetraplegic human,” Science, vol. 348, no. 6237, pp. 906–910, 2015.

[AJI] Ajiboye et al. Restoration of reaching and grasping movements through brain-controlled muscle stimulation in a person with tetraplegia: a proof-of-concept demonstration, The Lancet. 2017 Mar 28.

[AND] C. Andrews and A. C. Molnar, "A Passive Mixer-First Receiver With Digitally Controlled and Widely Tunable RF Interface," in IEEE Journal of Solid-State Circuits, vol. 45, no. 12, pp. 2696-2708, Dec. 2010.

[BJO] T. Björninen, R. Muller, P. Ledochowitsch, L. Sydänheimo, L. Ukkonen and J. Rabaey, "Antenna design for wireless electrocorticography," Proceedings of the 2012 IEEE International Symposium on Antennas and Propagation, Chicago, IL, 2012, pp. 1-2.

[BOA] A. Boaventura, J. Santos, A. Oliveira and N. B. Carvalho, "Perfect Isolation: Dealing with Self-Jamming in Passive RFID Systems," in IEEE Microwave Magazine, vol. 17, no. 11, pp. 20-39, Nov. 2016.

[BRAN] D. M. Brandman, S. S. Cash and L. R. Hochberg, "Review: Human Intracortical Recording and Neural Decoding for Brain–Computer Interfaces," in IEEE Transactions on Neural Systems and Rehabilitation Engineering, vol. 25, no. 10, pp. 1687-1696, Oct. 2017.

[CAL] L. Calderin, S. Ramakrishnan, A. Puglielli, E. Alon, B. Nikolić and A. M. Niknejad, "Analysis and Design of Integrated Active Cancellation Transceiver for Frequency Division Duplex Systems," in IEEE Journal of Solid-State Circuits, vol. 52, no. 8, pp. 2038-2054, Aug. 2017.

[CHEN1] Y. Chen (2013) “Reflective Impulse Radios: Principles and Design,” Ph.D. Dissertation, University of California, Berkeley

[CHEN2] J. Chen (2014) “Advanced Architectures for Efficient mm-Wave CMOS Wireless Transmitters,” Ph.D. Dissertation, University of California, Berkeley

[CHIU] S. Chiu et al., "A 900 MHz UHF RFID Reader Transceiver IC," in IEEE Journal of Solid-State Circuits, vol. 42, no. 12, pp. 2822-2833, Dec. 2007.

[COL] J. L. Collinger et al., “High-performance neuroprosthetic control by an individual with tetraplegia,” Lancet, vol. 381, no. 9866, pp. 557–564, Feb. 2013.

[ENG] D.J. Englot, D. Ouyang, P.A. Garcia, N.M. Barbaro, E.F. Chang. “Epilepsy Surgery Trends in the United States, 1990-2008.” Neurology, vol 78, iss. 16, pp. 1200-1206, Apr. 2012.

[FIN] K. Finkenzeller, RFID Handbook: Fundamentals and Applications in Contactless Smart Cards, Radio Frequency Identification and Near-Field Communication, 3rd Edition, Wiley, 2013. Print

[GOOD] F. Goodarzy, E. Skafidas and S. Gambini, "Feasibility of Energy-Autonomous Wireless microsensors for Biomedical Applications: Powering and Communication," in IEEE Reviews in Biomedical Engineering, vol. 8, no. , pp. 17-29, 2015.

[HAR] Reid R. Harrison, "Designing Efficient Inductive Power Links for Implantable Devices," 2007 IEEE International Symposium on Circuits and Systems, pp. 2080–2083, IEEE, May 2007.

[HEC] Heck et. al, Two-year seizure reduction in adults with medically intractable partial onset epilepsy treated with responsive neurostimulation: Final results of the RNS System Pivotal trial. Epilepsia, 2014

[HOC] L. R. Hochberg et al., "Reach and grasp by people with tetraplegia using a neurally controlled robotic arm", Nature, vol. 485, no. 7398, pp. 372-375, May 2012.

[JOH] M. D. Johnson *et al*., "Neuromodulation for Brain Disorders: Challenges and Opportunities," in *IEEE Transactions on Biomedical Engineering*, vol. 60, no. 3, pp. 610-624, March 2013.

[KEE] S. Kee (2002) "The class E/F family of harmonic-tuned switching power amplifiers," Ph.D. Dissertation, California Institute of Technology.

[KIA] M. Kiani and M. Ghovanloo, "A 13.56-Mbps Pulse Delay Modulation Based Transceiver for Simultaneous Near-Field Data and Power Transmission," in IEEE Transactions on Biomedical Circuits and Systems, vol. 9, no. 1, pp. 1-11, Feb. 2015.

[KIM] E. H. Kim, K. Lee and J. Ko, "An isolator-less CMOS RF front-end for UHF mobile RFID reader," 2011 IEEE International Solid-State Circuits Conference, San Francisco, CA, 2011, pp. 456-458.

[KLU] E. A. M. Klumperink, H. J. Westerveld and B. Nauta, "N-path filters and mixer-first receivers: A review," 2017 IEEE Custom Integrated Circuits Conference (CICC), Austin, TX, 2017, pp. 1-8.

[KUO] N. C. Kuo, B. Zhao and A. M. Niknejad, "Novel Inductive Wireless Power Transfer Uplink Utilizing Rectifier Third-Order Nonlinearity," in IEEE Transactions on Microwave Theory and Techniques, vol. PP, no. 99, pp. 1-13.

[LEE] H. M. Lee, M. Kiani and M. Ghovanloo, "Advanced wireless power and data transmission techniques for implantable medical devices," 2015 IEEE Custom Integrated Circuits Conference (CICC), San Jose, CA, 2015, pp. 1-8

[MAND] S. Mandal and R. Sarpeshkar, "Power-Efficient Impedance-Modulation Wireless Data Links for Biomedical Implants," in IEEE Transactions on Biomedical Circuits and Systems, vol. 2, no. 4, pp. 301-315, Dec. 2008.

[MARK1] M. Mark et al., "A 1mm3 2Mbps 330fJ/b transponder for implanted neural sensors," 2011 Symposium on VLSI Circuits - Digest of Technical Papers, Honolulu, HI, 2011, pp. 168-169.

[MARK2] M. Mark (2011) Powering mm-Size Wireless Implants for Brain-Machine Interfaces, Ph.D. Dissertation, University of California, Berkeley

[MARK3] M. Mark, T. Björninen, L. Ukkonen, L. Sydänheimo and J. M. Rabaey, "SAR reduction and link optimization for mm-size remotely powered wireless implants using segmented loop antennas," 2011 IEEE Topical Conference on Biomedical Wireless Technologies, Networks, and Sensing Systems, Phoenix, AZ, 2011, pp. 7-10.

[MAY] E. M. Maynard, C. T. Nordhausen, and R. A. Normann, “The utah intracortical electrode array: A recording structure for potential brain-computer interfaces,” Electroencephalogr. Clin. Neurophysiol., vol. 102, no. 3, pp. 228–239, Mar. 1997.

[MUL1] R. Muller (2013)” Low Power, Scalable Platforms for Implantable Neural Recording,” Ph.D. Dissertation, University of California, Berkeley

[MUL2] R. Muller et al., "A Minimally Invasive 64-Channel Wireless µECoG Implant," in IEEE Journal of Solid-State Circuits, vol. 50, no. 1, pp. 344-359, Jan. 2015.

[NAT] National Spinal Cord Injury Statistical Center, “The 2012 annual statistical report for the spinal cord injury model systems,” Nscisc, p. 21, Oct. 2016.

[NGY] Ha H. Nguyen, Ed Shwedyk, “A First Course in Digital Communications,” Cambridge University Press, 2009. 249-251. Print.

[NIC1] MAL Nicolelis, Principles of neural ensemble physiology underlying the operation of brain–machine interfaces, Nature Reviews Neuroscience 10, 530–540 (2009)

[NIC2] Miguel A L Nicolelis, Dragan Dimitrov, Jose M Carmena, Roy Crist, Gary Lehew, Jerald D Kralik, and Steven P Wise, “Chronic, multisite, multielectrode recordings in macaque monkeys.” Proceedings of the National Academy of Sciences of the United States of America, vol. 100, no. 19 pp. 11041–6, Sep 2003.

[ORF] S. J. Orfanidis. (2013). Electromagnetic Waves and Antennas [Online]. Available: http://eceweb1.rutgers.edu/~orfanidi/ewa/

[PAN] Pandarinath C, Nuyujukian P, Blabe CH, Sorice BL, Saab J, Willett FR, Hochberg LR, Shenoy KV, Henderson JM. High performance communication by people with paralysis using an intracortical brain-computer interface.

[RUSH] A. D. Rush and P. R. Troyk, "A Power and Data Link for a Wireless-Implanted Neural Recording System," in IEEE Transactions on Biomedical Engineering, vol. 59, no. 11, pp. 3255-3262, Nov. 2012.

[SEO] Seo, Dongjin et al. Neuron , Wireless Recording in the Peripheral Nervous System with Ultrasonic Neural Dust, Volume 91 , Issue 3 , 529 - 539

[ZIE] Ziegler-Graham K, MacKenzie EJ, Ephraim PL, Travison TG, Brookmeyer R. Estimating the Prevalence of Limb Loss in the United States: 2005 to 2050. Archives of Physical Medicine and Rehabilitation2008;89(3):422-9.